Phase transitions in advanced relaxor-ferroelectric materials with a perovskite-type structure

Dissertation

Zur Erlangung des Doktorgrades der Naturwissenschaften
im Department Geowissenschaften der Universität Hamburg

vorgelegt von

Bernd Jens Maier

aus Böblingen

Hamburg

2010

Als Dissertation angenommen vom Department Geowissenschaften der Universität Hamburg

auf Grund der Gutachten von Prof. Dr. Ulrich Bismayer
Prof. Dr. Boriana Mihaylova (Jun.-Prof.)

Hamburg, den 16. März 2010

Prof. Dr. Oßenbrügge
Dekan
Department Geowissenschaften

Contents

Abstract

Perovskite-type compounds of the general formula ABO_3 play a key role in modern materials science. In particular, relaxor ferroelectrics are of great technological importance due to their outstanding dielectric, optoelectric, and electromechanical properties related to the complex nanoscale structure of these materials, i.e. polar nanoregions (PNR) dispersed in a paraelectric matrix. Relaxor behaviour is most commonly found in lead-based compounds with partial or complete chemical B-site disorder. Although relaxors have been extensively studied over the last decades, the relationship between chemistry, polar nanostructure, local and macroscopic properties is still not clarified and requires further structural analysis.

In order to elucidate the impact of A-site doping on the structure of relaxors, a comparative X-ray/neutron diffraction study on selected A-site doped model relaxor systems $PbSc_{0.5}Ta_{0.5}O_3$ (PST) and $PbSc_{0.5}Nb_{0.5}O_3$ (PSN) was performed for the first time in this thesis. In particular, the effect of disturbed orientational order of lone-pair electrons (LPE) associated with A-site doping is analysed in regard to local elastic and local electric fields.

The detailed analysis of temperature-induced structural phase transformations highlights the importance of an undisturbed LPE system for the formation of ferroelectric long-range order (LRO). Substitution of Bi^{3+} for Pb^{2+} enhances the fraction of ferroelectrically ordered domains in PSN due to its affinity to form LPE, regardless of the additional local electric fields resulting from the aliovalent doping. In contrast, the isovalent substitution of the larger Ba^{2+}, without LPE, for Pb^{2+} disturbs the LPE system of Pb^{2+}. At the same time local elastic fields are introduced which lead to suppression of the ferroelectric LRO.

Pressure as a thermodynamical variable is a much stronger driving force as compared to temperature. Therefore, complementary high-pressure structural analysis on the same model compounds can reveal better structural peculiarities of perovskite-type relaxors. In the limited number of published high-pressure studies rearrangement and/or suppression of PNR was suggested, without however to specify the structure of the high-pressure phase in detail. This comparative study of the pure and doped PST and PSN reveals a pressure-induced structural phase transition involving elastic softening of both phases in all the samples. For the first time the high-pressure structural state of lead-based

perovskite-type relaxor ferroelectrics was revealed to consist of anti-phase tilts of BO_6 octahedra that continuously evolve with increasing pressure. Local elastic fields due to isovalent doping free of lone-pair electrons hamper the development of structural distortions associated with the high-pressure phase whereas orientational order of lone-pair electrons even enhances the distortions and lowers the critical pressure. Hence, the effect of A-dopants on the pressure-driven phase transition displays their impact on the temperature-induced structural transformations.

Lists

List of Figures

List of Tables

List of Abbreviations

ADP atomic displacement parameters

BM-EoS Birch-Murnaghan Equation of State

DAC diamond anvil cell

EoS Equation of State

EPMA electron probe microanalysis

FWHM full width at half maximum

HRTEM high-resolution transmission electron microscopy

LRO long-range order

LPE lone-pair electrons

PMN $PbMg_{1/3}Nb_{2/3}O_3$

PMT $PbMg_{1/3}Ta_{2/3}O_3$

PNR polar nanoregions

PSN $PbSc_{0.5}Nb_{0.5}O_3$

PSN-Ba $Pb_{0.93}Ba_{0.07}Sc_{0.5}Nb_{0.5}O_3$

PSN-Bi $Pb_{0.98}Bi_{0.02}Sc_{0.51}Nb_{0.49}O_3$

PSN-La $Pb_{0.77}La_{0.23}Sc_{0.62}Nb_{0.38}O_3$

PST $PbSc_{0.5}Ta_{0.5}O_3$

PST-Ba $Pb_{0.78}Ba_{0.22}Sc_{0.5}Ta_{0.5}O_3$

PZN $PbZn_{1/3}Nb_{2/3}O_3$

SAED selected area electron diffraction

$T_\mathbf{C}$ Curie temperature

$T_\mathbf{d}$ Burns temperature

TEM	transmission electron microscopy
T_{f}	freezing temperature
T_{m}	temperature of the dielectric permittivity maximum
TOF	time-of-flight
XRD	X-ray diffraction

1 Introduction

Relaxor ferroelectrics (Cross, 1987) are of great technological importance (Bhalla et al., 2000; Gruverman and Kholkin, 2006) as they exhibit outstanding dielectric, electroelastic, and electrooptic properties related to their complex nanoscale structure (Bokov and Ye, 2006; Hirota et al., 2006). Relaxors are used in capacitors, actuators, and transducers (Uchino, 2000), for example in medical ultrasonic devices (e.g. Hosono and Yamashita, 2006; Zhou, 2008). Their most interesting and promising application is however in non-volatile random-access memory (NVRAM) devices. Currently, the market is dominated by semiconductor memories, i.e. dynamic random-access memory (DRAM) and static random-access memory (SRAM) devices. They are fast but volatile, i.e. the stored information is lost with power failure. Current non-volatile memories include complementary metal oxide semiconductors (CMOS) with battery backup and electrically erasable read-only memory (EEPROM) devices, which are very expensive.

Ferroelectric random-access memory (FRAM) based on relaxor-ferroelectric thin films is one concept of realising a NVRAM which has the advantage of a low writing current as opposed to magnetic and phase-change RAMs. *Toshiba* announced a prototype of a new FRAM (Fig. 1.1) at the International Solid-State Circuits Conference 2009, which realises 128 MB storage and r/w speeds of 1.6 GB/s. This breaks Toshiba's own record of 32 MB storage and 200 MB/s data transfer rate, and pushes FRAM devices closer to the storage memory regime.

However, FRAMs suffer from fatique and aging effects, i.e. the reduction of polarisation with write cycles and the ability to keep the polarisation and thus the information over a long period of time. Current FRAMs are made of lead zircon titanate (PZT), strontium bismuth tantalate (SBT), and bismuth titanate (Scott, 2007). They can withstand 10^{12} cycles but a fatigue resistance of 10^{15} cycles is required if the FRAMs are to replace semiconductor memories completely. In order to overcome this limitation, better compounds or mixtures must be used in future devices which requires a better understanding of the relaxor behaviour.

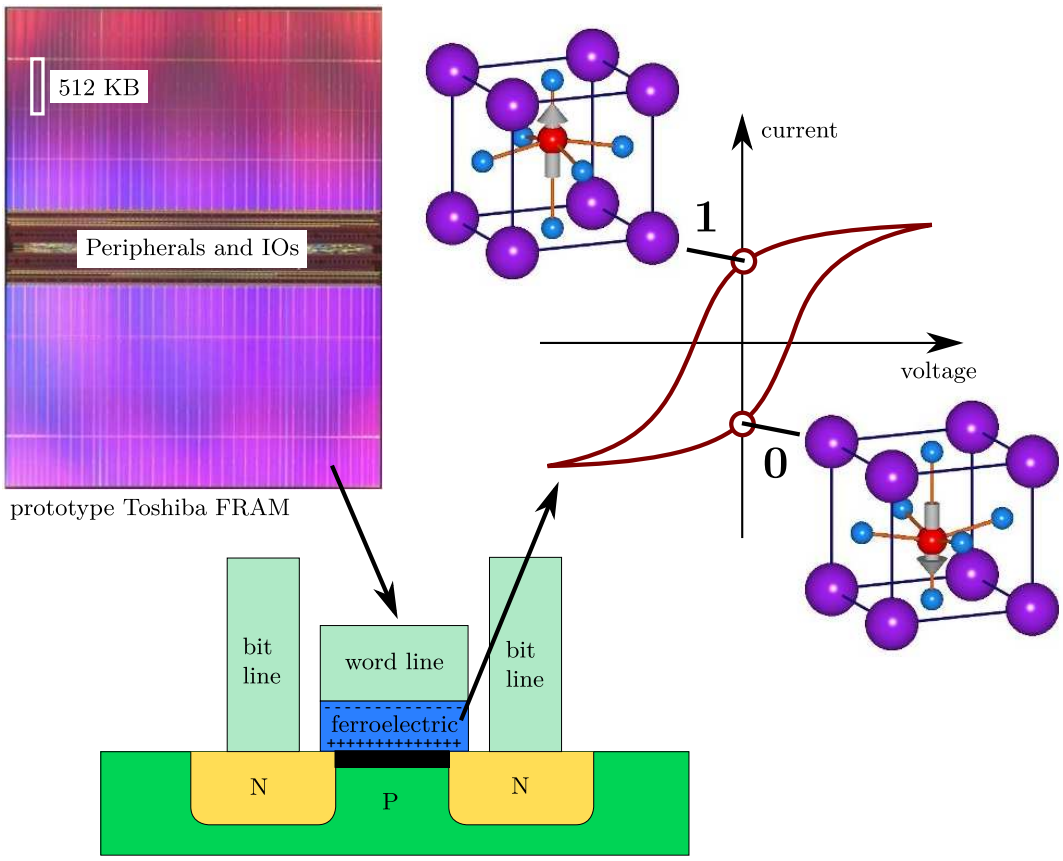

Figure 1.1: Ferroelectric random-access memory.

Hence, it is vital to understand the atomic mechanisms of relaxor ferroelectrics. This work aims to provide an experimental step towards tuning relaxor behaviour via doping selected model compounds.

1.1 The perovskite-type structure

The perovskite-type structure shows high variation in symmetry and plays an important role in material science (Bhalla et al., 2000). Although it has been named after the orthorhombic mineral perovskite with the formula $CaTiO_3$, the ideal perovskite structure is cubic with the general formula $A^{2+}B^{4+}X_3^{2-}$, where in most cases O^{2-} occupies the anion site (Fig. 1.2). However, there are also non-oxide perovskite-type materials, e.g. the fluoride perovskites, having F^- on the anion site such as $NaMgF_3$ where Na^+ and Mg^{2+} ensure the charge balance of the system. This example highlights the advantage of the perovskite-type structure: it allows for a vast variety of compositions, including the

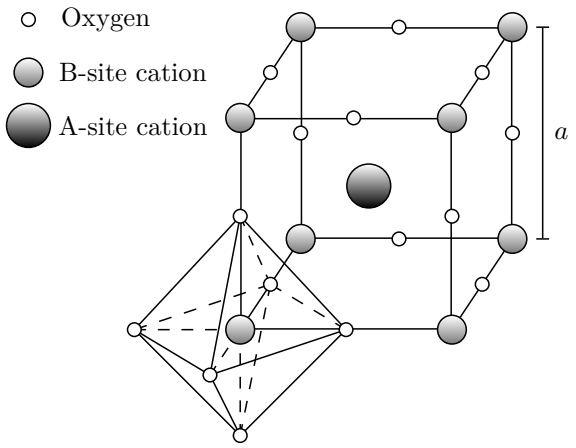

Figure 1.2: Schematic view of the cubic prototype perovskite-type structure with the formula $A^{2+}B^{4+}O_3^{2-}$. The space group is $Pm\bar{3}m$ with $a_p \sim 4$ Å, however, in the case of a mixed B-cation site with cation ordering, a doubling of the unit cell occurs and the space group becomes $Fm\bar{3}m$.

possibility for mixed-cation sites, leading to many outstanding physical properties such as giant magnetoresistance, ferroelectricity (see Sec. 1.2), and superconductivity (Bhalla et al., 2000).

An important measure of the deviation from the ideal cubic perovskite-type structure caused by the size of the compositional ions with the radii R_A for the A-site cations, R_B for the B-site cations, and R_X for the anions, is the *tolerance factor* introduced by Goldschmidt (1927):

$$t = \frac{R_A + R_X}{\sqrt{2}(R_B + R_X)} \tag{1.1}$$

It reflects a structural distortion (unit-cell distortion, tilting of octahedra, ...), which in turn affects physical properties such as the transition temperature or dielectric permittivity.

In the ideal case ($t = 1$), the size of A-site and B-site cations perfectly match the interstitial voids formed by the corresponding X-anion cages. If $t < 1$, the B-site cations are too large for their cage, thus governing the unit-cell parameter, while the A-site cations are left with too much room for vibration. For $t > 1$, the opposite is the case.

Figure 1.2 shows a schematic view of the perovskite-type oxide structure. Compounds with mixed-cation sites are *complex* perovskite-type oxides. Depending on the mixed-cation site, there are *A-site* complex perovskites with $(A'A'')BO_3$, *B-site* complex perovskites with $A(B'B'')O_3$, and the mixed case with $(A'A'')(B'B'')O_3$. Advanced ferroelectrics (see Sec. 1.3) usually have Na^+, K^+, Pb^{2+}, Ba^{2+}, La^{3+}, Bi^{3+}, ..., on the A-site and Mg^{2+}, Zn^{2+}, Sc^{3+}, Fe^{3+}, Ti^{4+}, Ta^{5+}, Nb^{5+}, ..., on the B-site.

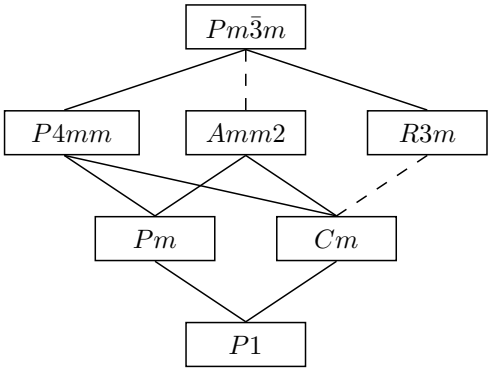

Figure 1.3: Group-subgroup relationship for perovskites with B-site cation displacements without octahedral tilts after Howard and Stokes (2005). Solid and dashed lines indicate continuous (second-order) and discontinuous (first-order) phase transition, respectively, in terms of Landau theory (see Tolédano and Dmitriev, 1996).

The prototype structure[1] of perovskite-type ferroelectrics is cubic with space group $Pm\bar{3}m$ and unit-cell parameter $a_p \sim 4$ Å. In the case of a B-site complex perovskite, B-site cation ordering can occur with an alternating 1:1, 1:2, or 1:3 sequence of B′ and B″ (111) layers along the cubic ⟨111⟩ direction, having an ordering vector of $1/2[111]^\star$, $1/3[111]^\star$, and $1/4[111]^\star$, respectively (Davies et al., 2008). B-site 1:1 order (e.g. in Pb_2ScTaO_6) doubles the unit cell, thus forming a face-centred cubic structure with space group $Fm\bar{3}m$ and unit cell $2a_p \times 2a_p \times 2a_p$ (Howard et al., 2003). For B-site 1:2 order, e.g. in $Ba_3ZnTa_2O_9$ (Jacobson et al., 1976), the cubic space group becomes $P\bar{3}m1$ with unit-cell parameters of $\sqrt{2}a_p \times \sqrt{2}a_p \times \sqrt{3}a_p$ (Howard and Stokes, 2004). In the case of B-site 1:3 order, e.g. in $Sr_4LiNb_3O_{12}$ (Hikichi et al., 1982), the structure adopts a monoclinic cell with $\sqrt{6}a_p \times \sqrt{2}a_p \times 2\sqrt{2}a_p$ and $\beta \sim 125°$ (Davies et al., 2008). However, 1:3 order in a cubic perovskite, e.g. $Ba_4Li^+Sb_3^{5+}O_{12}$ (Jacobson et al., 1974), the unit cell is doubled with space group $Im\bar{3}m$ (Howard and Stokes, 2005). Unlike the ⟨111⟩-ordered schemes given above, this structure is not layered, but contains a three-dimensional distribution of B′ and B″ cations.

Depending on the composition, temperature, and pressure, the prototype cubic unit cell can be distorted as a result of cation shifts, octahedral tilting, octahedral distortion, or a combination of them, lowering the symmetry to a subgroup. Figure 1.3 shows the group-subgroup relationship for untilted perovskite-type structures with displaced B-site cations (Howard and Stokes, 2005) which is the cause for ferroelectricity in perovskites (see Sec. 1.2).

Tilting of octahedra in perovskites can occur along one or more axis. Glazer (1972) introduced a classification of the possible tilt systems in perovskites. The magnitude of tilts about the cubic crystallographic directions [100], [010], and [001] are denoted by a, b, and c,

[1] The prototype structure refers to the paraelectric structure of ferroelectrics. Its space group is a supergroup of the one exhibited by the ferroelectric phase

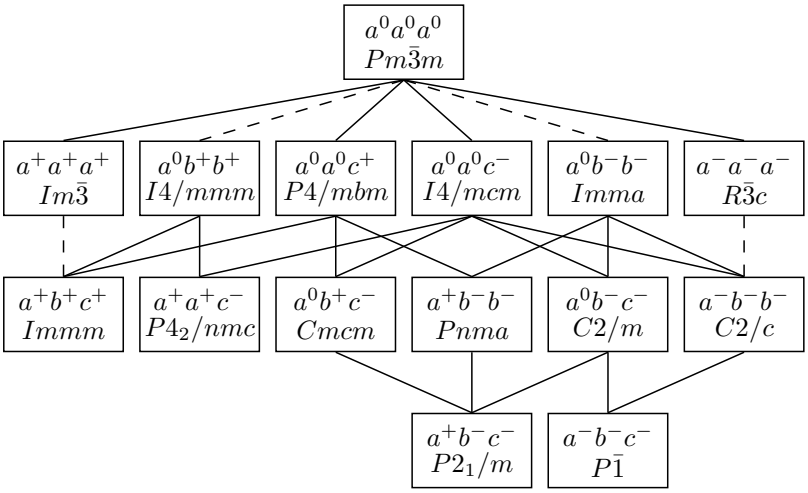

(a) B-site disordered systems.

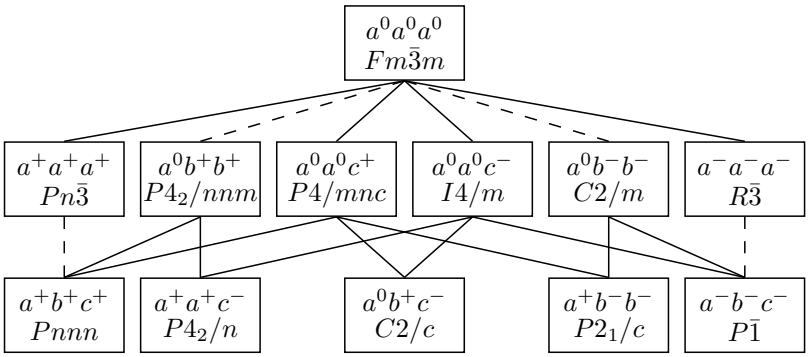

(b) B-site 1:1 ordered systems.

Figure 1.4: Group-subgroup relationship for perovskites with octahedral tilts (Howard et al., 2003; Howard and Stokes, 2005). Solid and dashed lines indicate continuous (second-order) and discontinuous (first-order) phase transition, respectively, in terms of Landau theory (see Tolédano and Dmitriev, 1996).

respectively. Tilts of equal magnitude are denoted by repeating the appropriate letter, e.g. *abb* means equal tilts about [010] and [001] with a different tilt about [100]. A superscript to the letter indicates the tilting of adjacent octahedra along the corresponding axis: no tilt (0), same tilts (+), or opposite tilts (−). Thus, the tilt system $a^0b^-b^-$ indicates a tetragonal system, having no tilts along the cubic [100] direction and opposite tilts of adjacent octahedra along the cubic [010] and [001] directions, both with the same tilt magnitude about the corresponding axis. Figures 1.4a and 1.4b show the group-subgroup relationship for tilted B-site disordered perovskites ($Pm\bar{3}m$) after Howard and Stokes (2005) and B-site 1:1 ordered perovskites ($Fm\bar{3}m$) after Howard et al. (2003).

Stokes et al. (2002) modified the Glazer notation with a subscript + or −, denoting ferroelectric B-site cation displacements along the given axis, and listed a table of $Pm\bar{3}m$ subgroups having tilts and displaced B-site cations.

1.2 Ferroelectricity in perovskite-type materials

Ferroics are a generic class of materials exhibiting a spontaneous phase transition at T_C upon cooling, at which a non-ferroic *prototype* structure becomes ferroic by lowering the point symmetry. Depending on the physical properties, i.e. the thermodynamic variable involved, there are three primary classes of ferroics: ferroelectrics, ferromagnetics, and ferroelastics (Cross, 1990), in which spontaneous polarisation $\boldsymbol{P}_\mathrm{S}$, spontaneous magnetisation $\boldsymbol{M}_\mathrm{S}$, and spontaneous strain $\boldsymbol{S}_\mathrm{S}$, occurs on cooling at T_C, respectively. The spontaneous polarisation, magnetisation, and strain exhibit a temperature-dependent hysteresis loop under the corresponding external field, $\boldsymbol{P}(\boldsymbol{E})$, $\boldsymbol{M}(\boldsymbol{H})$, and $\boldsymbol{S}(\boldsymbol{T})$, respectively.

In the case of ferroelectrics, the polarisation $\boldsymbol{P}$ is related to the electric field $\boldsymbol{E}$ via the second-rank tensor of the *dielectric susceptibility* χ_{ij}:

$$P_i = \varepsilon_0 \chi_{ij} E_j \tag{1.2}$$

where $\varepsilon_0 = 8.8542$ pF/m is the vacuum permittivity ($\varepsilon_0 \mu_0 = 1/c_0^2$, where μ_0 is the vacuum permeability and c_0 is the vacuum light speed). More common is the *dielectric permittivity* $\varepsilon = \varepsilon_0(1 + \chi)$, which relates the electric displacement $\boldsymbol{D}$ with the applied electric field $\boldsymbol{E}$:

$$D_i = \varepsilon_{ij} E_j = \varepsilon_0 E_i + P_i \tag{1.3}$$

The dielectric permittivity as a function of temperature, $\varepsilon(T)$ exhibits a sharp peak near T_C (Fig. 1.5a) with T_m close to T_C. In the paraelectric state above T_C, $\varepsilon(T)$ follows the Curie-Weiss law:

$$\varepsilon - 1 = \chi = \frac{C}{T - T_0} \tag{1.4}$$

where C is the material-specific Curie constant. The phase transition from the paraelectric to the ferroelectric state is usually first-order. However, if T_C coincides with T_0 at which $1/\varepsilon$ approaches zero, a second-order phase transition occurs when T reaches T_C from above. The polarisation, $\boldsymbol{P}$, is switchable under an external electric field, following a hysteresis loop schematically shown in Fig. 1.5b.

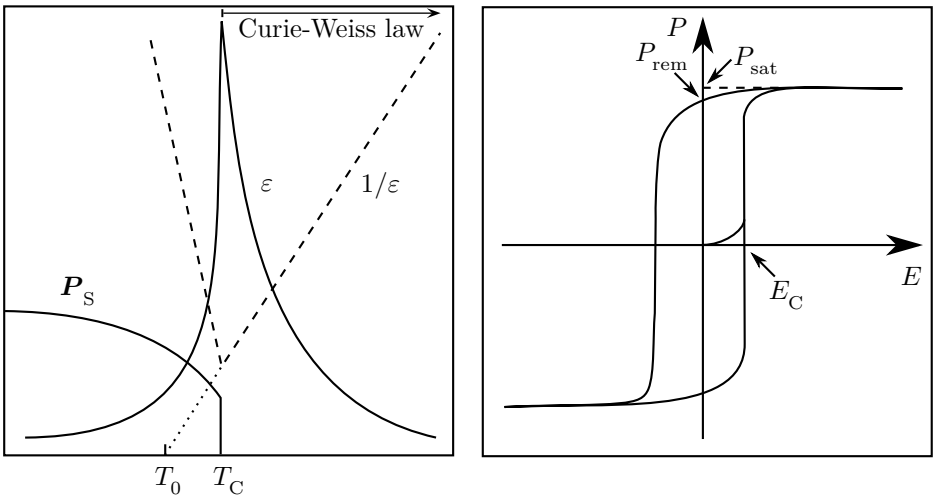

(a) Schematic temperature dependence of the dielectric permittivity ε and spontaneous polarisation $\boldsymbol{P}_\mathrm{S}$ of normal ferroelectrics after Hirota et al. (2006). At T_C a first-order phase transition from the paraelectric to the ferroelectric state, in which spontaneous polarisation $\boldsymbol{P}_\mathrm{S}$ occurs, takes place. If $T_\mathrm{C} = T_0$, at which $1/\varepsilon$ approaches zero when T reaches T_C from above, the phase transition is second-order.

(b) Schematic polarisation hysteresis loop of normal ferroelectrics under an external field at $T < T_\mathrm{C}$ after Samara et al. (2006). After the polarisation has reached its saturation P_sat, a remanent polarisation P_rem remains when the field is switched off and a coercive field in opposite direction E_C is required to nullify P_rem.

Figure 1.5: Electric properties of classical ferroelectrics.

Ferroelectricity is limited to the ten polar crystal classes (1, 2, m, mm2, 3, 3m, 4, 4mm, 6, and 6mm) which possess a polar axis, i.e. no mirror plane exists perpendicular to the axis. Thus, the existence of a dipole moment is symmetrically allowed. The phase transition from the prototype paraelectric structure to the polar ferroelectric structure is of displacive nature (Lines and Glass, 1977), where cations are off-centre shifted, thus creating a dipole moment.

Cohen (1992) first revealed the origin of ferroelectricity in a simple perovskite-type structure by electronic structure calculations on the well-known ferroelectrics barium titanate ($BaTiO_3$) and lead titanate ($PbTiO_3$). Both compounds have a $Pm\bar{3}m$ prototype structure in the paraelectric phase at high temperatures with similar volumes. However, they show different ferroelectric behaviour, i.e. $BaTiO_3$ undergoes a cubic→tetragonal→orthorhombic→rhombohedral phase transition sequence upon cooling, whereas $PbTiO_3$ exhibits only a cubic→tetragonal transition. Cohen (1992) found that a *d*-hybridisation between the B-cation and O is essential to overcome the short-range ionic core repulsion which stabilises the cubic phase although long-range Coulomb energy

favours a ferroelectric distortion. In the case of $PbTiO_3$, the Pb 6s and the O 2p states are also strongly hybridised. This yields a stereochemically active lone pair which leads to a large c/a strain which is further enhanced by the smaller ionic radius of Pb^{2+} as compared to Ba^{2+}. The strain stabilises the ferroelectric distortion and leads to a tetragonal ground state. In contrast, Ba^{2+} is fully ionic and is therefore not polarising with the ferroelectric distortion, thus, the strain is small and the ferroelectric structure has a rhombohedral ground state. As temperature increases, the atoms average over the [111] distortions, leading to the sequence of phase transitions stated above. Based on first-principles calculations, Miyazawa et al. (2003) claimed that the large ferroelectric distortion in $PbTiO_3$ is due to a hybridisation between Pb 6p and O 2p states, whereas the Pb 6s states behave like shallow core levels.

1.3 Advanced ferroelectrics: relaxors

Most relaxor ferroelectrics are lead-based B-site complex perovskite-type materials with a partial or complete chemical disorder on the B-site (Bokov and Ye, 2006), e.g. $PbSc_{0.5}Ta_{0.5}O_3$ (PST), $PbSc_{0.5}Nb_{0.5}O_3$ (PSN), $PbMg_{1/3}Ta_{2/3}O_3$ (PMT), and $PbMg_{1/3}Nb_{2/3}O_3$ (PMN). Recently, relaxor properties were also found in lead-free ternary systems such as $(1-x-y)BaTiO_3$–$xBaZrO_3$–$yBaLiF_3$ (Kerfah et al., 2000) and $(1–x–y)BaTiO_3$–$xCaTiO_3$–$ySrTiO_3$ (Zhang et al., 2008) in a specific compositional range of x and y. Other structure types can also exhibit relaxor properties, e.g. , the pyrochlore-type structure $Cd_2Nb_2O_7$ (Samara and Venturini, 2006) and $Sr_{1-x}Ba_xNb_2O_6$ of tungsten-bronze type (Neurgaonkar et al., 1988; Fan et al., 1998).

1.3.1 Dielectric properties of relaxors

In contrast to normal ferroelectrics, relaxors show a strong frequency dependence of the dielectric permittivity as a function of temperature. The temperature of the dielectric permittivity maximum T_m is near but above T_C and also depends on the probe frequency f. Instead of a sharp phase transition at T_C, a diffuse phase transition over a temperature range takes place below $T_m(f)$, from the *ergodic*[2] state to either a ferroelectric LRO state (Fig. 1.6a) at T_C or to a *non-ergodic* state (Fig. 1.6b) at the freezing temperature T_f. For relaxors the Curie-Weiss law is valid only at very high temperatures, i.e. above a characteristic temperature called the Burns temperature T_d (see below). Between T_d and

[2] ergodic state of a system: no preferred direction after averaging over time or ensemble

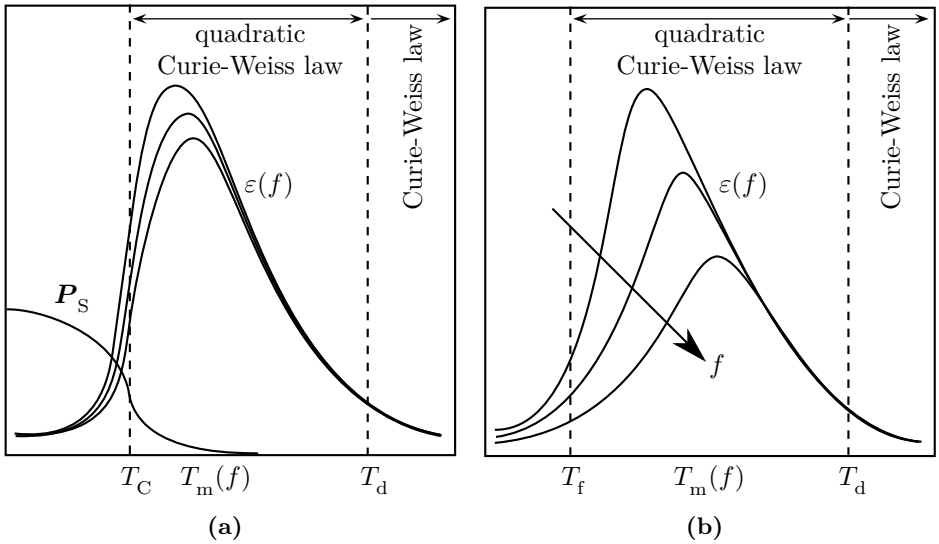

Figure 1.6: Schematic temperature dependence of the dielectric permittivity ε and spontaneous polarisation $\boldsymbol{P}_\mathrm{S}$ after Hirota et al. (2006): (a) relaxors with a diffuse relaxor-to-ferroelectric phase transition. T_C is below $T_\mathrm{m}(f)$ and spontaneous polarisation $\boldsymbol{P}_\mathrm{S}$ occurs already above T_C. (b) canonical relaxors. At the Burns temperature T_d PNR nucleate and after growing with decreasing temperature, they freeze to a non-ergodic state at T_f. $\boldsymbol{P}_\mathrm{S}$ appears only under an external electric field.

T_m, the dielectric permittivity can be better approximised by a quadratic relation (Uchino, 2000):

$$\varepsilon - 1 = \chi = \frac{C'}{(T - T_0')^2} \tag{1.5}$$

The relation between temperature and the frequency of the dielectric permittivity peak is described by the Vogel-Fulcher law:

$$f = \frac{1}{2\pi\tau_0} \exp\left(-\frac{E_a}{T_\mathrm{m} - T_\mathrm{VF}}\right) \tag{1.6}$$

where τ_0, E_a, and T_VF are fitting parameters (Bokov and Ye, 2006). The Vogel-Fulcher law is also typical for dipole glasses.

1.3.2 Temperature evolution of the relaxor structure

Relaxor ferroelectrics owe their outstanding properties to their complex local structure. At temperatures well above T_C, clusters of dynamic PNR are dispersed in the paraelectric structure. Figure 1.7a shows schematically the temperature evolution of the PNR. A structural transformation from the paraelectric state to the ergodic relaxor state occurs

with the nucleation of PNR at T_d at which the refractive index deviates from a linear behaviour with temperature (Burns and Dacol, 1983) as shown in Fig. 1.7b. The nucleation and growth of PNR was also revealed by neutron pair distribution function analysis (Jeong et al., 2005). In addition, other methods prove the existence of PNR, such as X-ray and neutron diffuse scattering analysis (see Sec. 1.3.4), Raman scattering (Svitelskiy et al., 2003; Toulouse et al., 2005; Mihailova et al., 2007a), and NMR (Blinc et al., 2000, 2001; Laguta et al., 2004; Zhou et al., 2004; Vijayakumar et al., 2007). T_d also marks the temperature at which the dielectric permittivity deviates from a linear (Eq. 1.4) to a quadratic (Eq. 1.5) Curie-Weiss law as shown in Fig. 1.7c after Samara (2003). The nucleation process gives rise to an acoustic emission peak shown in Fig. 1.7e after Dul'kin et al. (2006) and leads to a change in the slope of the linear temperature dependence of the pseudo-cubic lattice parameter, a (Fig. 1.7d after Dkhil et al. (2009)).

Upon cooling the PNR grow (Jeong et al., 2005) and couple at $T^\star$ (La-Orauttapong et al., 2001; Svitelskiy et al., 2003; Toulouse et al., 2005; Mihailova et al., 2008b; Dkhil et al., 2009). This results in a spontaneous strain which gives rise to a deviation from a linear temperature dependence of the unit-cell parameter a (Fig. 1.7d) and a strong acoustic emission (Fig. 1.7e) near $T^\star$. The PNR grow on further cooling and are abundant near T_m at which they have an average lifetime of 10^{-4}–10^{-5} s (Blinc et al., 2001).

Below T_m, the PNR either freeze to a non-ergodic (glassy-like) state at T_f for canonical relaxors or a diffuse "relaxor-to-ferroelectric" phase transition takes place at T_C. Canonical relaxors in the non-ergodic state can be irreversibly transformed to a normal ferroelectric state by an external electric field (Bokov and Ye, 2006), which distinguishes them from dipole glasses. Upon heating, the field-induced normal ferroelectric state transforms to an ergodic state at T_C, which is very close to T_f.

1.3.3 Theoretical approaches to relaxor behaviour

Although the existence of PNR is experimentally proved (Bokov and Ye, 2006, and references therein), the mechanism of their formation is still a matter of debate. It is widely believed that the PNR are related to quenched compositional disorder, since most relaxors, after becoming compositionally ordered by temperature annealing, show an abrupt phase transition to a normal ferroelectric or antiferroelectric state (Bokov and Ye, 2006). The first approach to explain relaxor behaviour was proposed by Isupov and Smolenskii (Isupov, 2003, and references therein). T_C depends on the chemical composition and impurity concentration. The compositional disorder leads to quenched spatial fluctuations

of concentrations of different ions sharing the same site, which results in local fluctuations of T_C. Thus, PNR can be seen as regions with elevated T_C, which transform first to

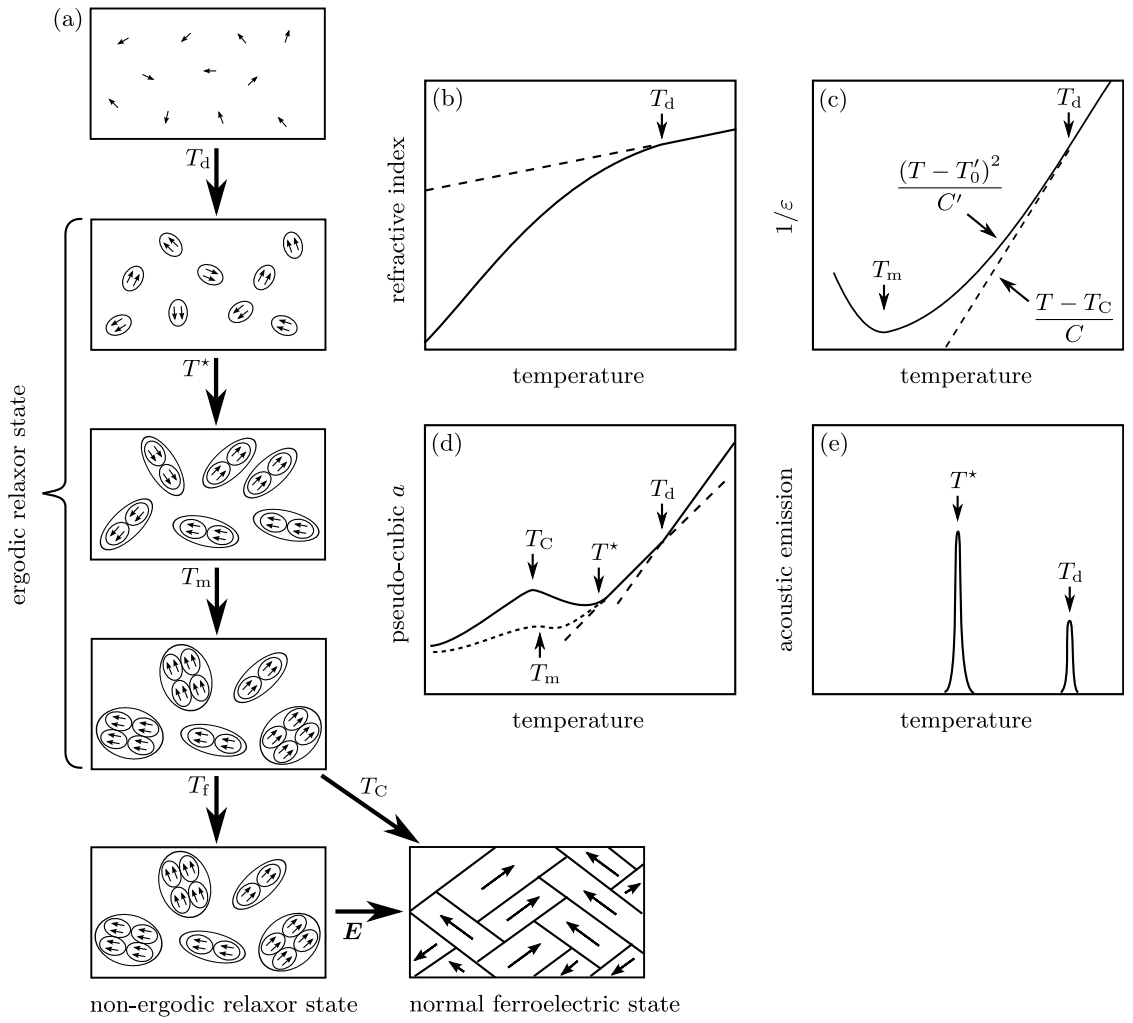

Figure 1.7: Schematic temperature evolution of the local structure of relaxor ferroelectrics (a). At T_d, polar nanoregions (PNR) nucleate by coupling of randomly off-centred cation shifts, resulting in a deviation from the linear temperature dependence of the refractive index (b, after Burns and Dacol (1983)). At the same temperature the dielectric permittivity deviates from a Curie-Weiss law (c, after Samara (2003)) and the linear temperature dependence of the pseudo-cubic lattice parameter, a, shows a change in slope (d, after Dkhil et al. (2009)). Upon further cooling, PNR couple at $T^\star$, leading to a deviation from a linear temperature dependence of the unit-cell parameter a (d, after Dkhil et al. (2009)) resulting from accumulated spontaneous strain which also gives rise to an acoustic emission peak (e, after Dul'kin et al. (2006)). The PNR grow on further cooling until T_m, after which they either freeze to a non-ergodic state at T_f for canonical relaxors of a diffuse phase transition at T_C to a normal ferroelectric state takes place. The non-ergodic relaxor state can be irreversibly transformed into a normal ferroelectric state by an external electric field.

the ferroelectric state upon cooling, giving rise to a smeared transition. However, the cation concentration alone cannot explain the frequency dispersion of $\varepsilon(T)$. Cross (1987) proposed a superparaelectric model which consists of flipping polar regions with a relaxation time similar to superparamagnetic nanoparticles of $\tau = \tau_0 \exp(E_b/k_B T)$ where E_b can be considered as an energy barrier between spin orientation states. The model assumes that these dynamical PNR, flipping between different orientation states, give rise to the frequency dependency of $\varepsilon(T)$. Both models do not consider interactions between the polar nanoregions. Nowadays, there exist a variety of models which describe the formation of PNR with two basic underlying concepts.

The first concept considers the PNR as local phase fluctuations, thus the crystal consists of nanosized polar regions with lower symmetry embedded into a matrix of unchanged (cubic) symmetry. This is the basis of the dipole-glass models which elaborate the models developed by Isupov and Cross. These models have the disadvantage that they cannot explain the crossover from relaxor to ferroelectric state under an external electric field.

The second concept considers the whole crystal consisting of low-symmetry nanodomains separated by domain walls having a thickness comparable to the size of nanodomains. This concept is represented by the random-field model (Westphal et al., 1992; Kleemann, 1993). The model is based on the theoretical work of Imry and Ma (1975) who showed that in a system having an order parameter of continuous orientational symmetry, a second-order phase transition is hindered by quenched random local fields. Although the order parameter in perovskite-type relaxors can be aligned along a finite number of definite crystallographic directions, its symmetry can be regarded as quasi-continuous if the number of directions is large as in the case of cubic-to-rhombohedral phase transitions: $\boldsymbol{P}_\mathrm{S}$ can be aligned along $\{111\}$, i.e. eight directions. Thus, due to the quenched random electric fields arising from the compositional disorder, the system breaks into small nanodomains analog to PNR below T_C instead of developing ferroelectric LRO. Within the framework of this concept the frequency dispersion of $\varepsilon(T)$ is explained via a complex domain-wall motion.

As mentioned in Sec. 1.2, ferroelectricity in an ordered perovskite-type structure depends on the electrostatic interactions, the short-range repulsions, and the covalent bonding. Considering electrostatic interactions, Glinchuk and Farhi (1996) developed the random-field theory for relaxors, in which orientable dipoles created by shifts of ferroelectrically active cations are embedded in a highly polarisable host matrix. The dipole-dipole interactions are random and indirect via the host matrix, leading to ferroelectric order at low temperatures. Thus, additional static/dynamic local electric fields are introduced,

originating from compositional disorder, impurities, vacancies, shifts of non-ferroactive cations, etc. Hence, this model can be considered as a hybrid model between the two concepts mentioned above. The model predicts that depending on the strength of local elastic fields a dipolar glassy state or a ferroelectrically ordered state is developed at low temperatures. Bokov (1997) developed a similar model and included short-range repulsions between the ions. A model based on random covalent bonding was introduced by Egami (2002).

1.3.4 Diffuse X-ray and neutron scattering analysis of perovskite-type relaxors

The described theoretical approaches can hardly be distinguished experimentally, because they all assume a coexistence of spatial nanoregions with and without net polarisation. However, since relaxor properties are governed by the structure and abundance of PNR, the application of methods probing the atomic structure is vital for better understanding the origin of relaxor behaviour. The most prominent experimental evidence of PNR is the related X-ray or neutron diffuse scattering. It exhibits a very specific shape for all lead-based perovskite-type relaxors: a "butterfly" shape for $h00$ reflections and an ellipsoid shape for $hh0$ peaks (see the $\bar{2}00$ and $\bar{2}20$ in Fig. 1.8b, respectively). The diffuse scattering is related to atomic correlations in the real space. Xu et al. (2004) performed a three-dimensional mapping of the diffuse X-ray scattering (Fig. 1.8c) of a $PbZn_{1/3}Nb_{2/3}O_3$ (PZN) crystal doped with 8% $PbTiO_3$ (PZN-8PT). They found the diffuse scattering to consist of $\langle 110 \rangle$-type intensity rods with distributions different for each type of reflection. Thus, they concluded that PNR must be composed of atomic shifts correlating in 110 cubic planes. Thus PNR have a disc-like shape with local polarisations along $\langle 110 \rangle$ cubic directions, i.e. different from the direction of macroscopic polarisation which is along the cubic $\langle 111 \rangle$ directions. Xu et al. (2006b,a) have shown with neutron and X-ray diffuse scattering measurements on PZN-8PT and PZN, respectively, that the PNR even persist in the ferroelectric phase. An applied external electric field along the [111] direction, enlarging the volume fraction of ferroelectric domains aligned along the field direction, revealed a redistribution of the diffuse scattering. This implies that the atomic periodicity in PNR couple to that of the surrounding lattice and the $\langle 110 \rangle$ polarisations of PNR are preferentially aligned perpendicular to the polarisation of the surrounding ferroelectric matrix.

The model of PNR proposed by Xu et al. (2004) is also supported by Welberry et al. (2005); Welberry and Goossens (2006) who stated, based on neutron diffraction studies on PZN

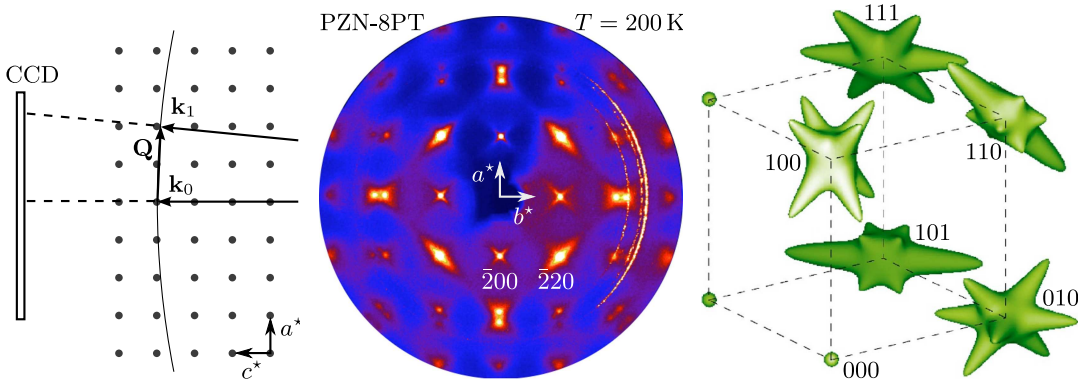

(a) Scattering geometry. **(b)** Diffraction pattern close to $(hk0)$. **(c)** Three-dimensional model of the diffuse scattering

Figure 1.8: Three-dimensional mapping of diffuse X-ray scattering originating from PNR in a PZN-8PT crystal at $T = 200$ K (below $T_C \sim 450$ K) after Xu et al. (2004). A well oriented sample was measured with monochromatic high-energy X-rays, schematically shown in (a). Thus, the diffraction image on the CCD detector shown in (b) is close to the $(hk0)$-layer, deviating further from $l = 0$ with larger values of $\boldsymbol{Q}$. By slightly tilting and rotating the crystal, the diffuse scattering is mapped three-dimensionally which is shown in (c).

and subsequent Monte-Carlo simulation, that Pb shifts along the ⟨110⟩ directions towards one of the neighbouring oxygen ions are correlated to form planar PNR perpendicular to each of the 12 ⟨110⟩ directions. However, as a response to the publication of Pasciak et al. (2007), Welberry and Goossens (2008) found that Pb shifts along the ⟨100⟩ and ⟨111⟩ directions can also give rise to the observed diffuse scattering features. Pasciak et al. (2007) proposed a different model of PNR, describing them as three-dimensional polar domains with walls parallel to 110 planes. Relative atomic shifts of neighbouring domains must be parallel to the ⟨110⟩ directions in order to satisfy the special extinction conditions for the diffuse rods. These relative shifts can be achieved by a combination of atomic shifts in all three symmetrically nonequivalent cubic directions ⟨100⟩, ⟨110⟩, and ⟨111⟩.

1.3.5 High-pressure studies

To study relaxor ferroelectrics under high pressures is of particular interest as the mechanical load can slow down the dynamic structural fluctuations. Thus, high-pressure studies can help to resolve the structural complexity in relaxors, i.e. revealing energetically preferred non-cubic atomic clustering. However, only a limited number of high-pressure experiments have been reported in literature so far. Samara et al. (2006) revealed a ferroelectric-to-relaxor crossover for various lead-based compounds by dielectric permittivity measurements at moderate pressures up to 2 GPa and concluded that pressure favours the relaxor

structural state. However, other studies reported a pressure-induced suppression of the diffuse scattering arising from PNR (Chaabane et al., 2003; Kreisel et al., 2003; Ahart et al., 2005; Janolin et al., 2006; Mihailova et al., 2008a), which indicates that the high-pressure phase of lead-based perovskite-type relaxors is not in a relaxor state. In addition, high-pressure Raman scattering is inconsistent with the cubic symmetry of the paraelectric phase and differs from Raman scattering observed at low temperatures in the ferroelectric state (Chaabane et al., 2004; Ahart et al., 2005; Janolin et al., 2006; Mihailova et al., 2008a; Welsch et al., 2009b). Thus, pressure induces ferroic structural species which do not develop upon cooling. However, no explicit structure has been reported for the high-pressure phase so far.

Synchrotron single-crystal XRD experiments on PMN revealed that the broad super-structure reflections arising from chemical B-site ordered domains are superimposed with an additional sharp but weak Bragg reflections above 4 GPa Chaabane et al. (2003). In combination with their unpublished high-pressure neutron diffraction patterns, which showed the same feature in a similar weak manner, Chaabane et al. (2003) concluded that this pressure-induced reflection contribution is associated with antiparallel cation shifts rather than BO_6 octahedral tilting. Janolin et al. (2006) observed similar superlattice reflections increasing with pressure in PZN. However, in conjunction with high-pressure Raman scattering data, Janolin et al. (2006) interpreted these reflections as a result of a pressure-induced development anti-phase BO_6 octahedral tilting, suggesting $R\bar{3}c$ as the most likely space group candidate. This would be consistent with the general principle that "2:4" perovskites with an average cation charge of 4+ on the octahedral sites undergo tilt transitions to lower-symmetry structures with greater tilts on increasing pressure (Angel et al., 2005).

In contradiction to the results above, high-pressure neutron powder diffraction data on PMT (Gvasaliya et al., 2006) and PMN (Rotaru et al., 2008) revealed no pressure-induced super-lattice reflections. However, their structure refinements in $Pm\bar{3}m$ revealed that the magnitudes of the Pb displacements decrease with pressure, while the anisotropy of the oxygen displacements within a cubic average structure increases in a way consistent with the development of octahedral tilting.

1.4 Aims of the study

The existence of PNR is the reason for the special physical properties of relaxor ferroelectrics. The theoretical approaches to explain the formation and temperature evolution of the PNR

are still a matter of debate. They are commonly based on random electric fields associated with the local charge imbalance due to the chemically disordered, heterovalently occupied B sites. However, recent publications have reported relaxor properties in compounds with no chemical B-site disorder. Torres-Pardo et al. (2009) revealed induced relaxor behaviour by cationic vacancies in $Na_{1-x}Sr_{x/2}\square_{x/2}NbO_3$ with $x = 0.4$. Samara and Venturini (2006) revealed relaxor properties in $Cd_2Nb_2O_7$, a pyrochlore-type structure with chemically homogeneous cation sites. Lente et al. (2006) have shown that the relaxor state can be induced in normal ferroelectrics via isovalent cation substitution. By varying the barium content with $x = 0$–0.4 in $Pb_{1-x}Ba_xZr^{4+}_{0.65}Ti^{4+}_{0.35}O_3$, relaxational properties were induced at a Ba content of $0.3 \leq x \leq 0.4$. In addition, doping with Ba enhances the relaxational properties of $PbSc_{0.5}Ta_{0.5}O_3$ (Marinova et al., 2006) and PSN $Pb_{0.94}Ba_{0.06}Sc_{0.5}Nb_{0.5}O_3$. These examples clearly show that other factors can govern the relaxor state than chemical B-site disorder in a perovskite-type structure.

Thus, the objective of the presented study was to elucidate the impact of A-site doping on the structure of the model relaxor compounds PST and PSN with different elements. Both pure compounds develop ferroelectric LRO with a diffuse phase transition near T_C. Pb^{2+} cations on the 12-fold coordinated A site of a perovskite-type structure have an ionic radius of $r_i = 1.49$ Å (Shannon, 1976) and show affinity to form LPE. Thus, A-site doping with Ba^{2+} ($r_i = 1.61$ Å, no LPE), Bi^{3+} ($r_i = 1.45$ Å, LPE)[3], and La^{3+} ($r_i = 1.36$ Å, no LPE) allows to study the effect of local elastic strain and local electric fields in conjunction with the influence of the (violated) LPE system. For this purpose, temperature- and pressure-dependent structural phase transitions were studied in these compounds using X-ray and neutron diffraction combined with complementary results of Raman spectroscopic measurements. In addition, the high-pressure structural state of lead-based relaxor ferroelectrics is elucidated.

[3]The ionic radius for 12-fold coordinated Bi^{3+} was linearly extrapolated from the values for 5-, 6-, and 8-fold coordinated Bi^{3+} (Shannon, 1976)

2 Experimental Methods

2.1 Theoretical aspects

2.1.1 X-ray diffraction

Crystalline materials have their atoms periodically arranged in a lattice with unit-cell parameters typically in the order of 0.2 to tenths of nanometers. This allows for matter-penetrating electro-magnetic radiation with a wavelength of $\lambda \sim$ Å (X-rays) to be diffracted and, subsequently, to determine the atomic structure from the resultant diffraction pattern. According to quantum mechanics beams of neutrons and electrons can be considered as propagating waves, having the so-called *de Brouglie* wavelength:

$$\lambda = \frac{2\pi\hbar}{\sqrt{2m_0 E_{\text{kin}}}} \tag{2.1}$$

where m_0 is the rest mass and E_{kin} is the kinetic energy of the particle. Thus, neutrons or electrons with an appropriate velocity also give rise to a diffraction pattern when passing through a periodic atomic system and, hence, can also be used to resolve the crystal structure.

Each atom in the lattice elastically scatters the incident wave, resulting in an interference of all scattered waves. The Laue Equation (Eq. 2.2) gives the condition for maximum constructive interference in any direction,

$$a(\cos\alpha_1 - \cos\alpha_2) = n\lambda \tag{2.2}$$

where a is the spacing of a given lattice direction, α_1 and α_2 are the respective angles of the incident beam and propagated wave relative to the lattice direction, n is the order of scattering, and λ is the wavelength of the incident radiation. Diffraction occurs in three dimensions when all the three Laue Equations are satisfied for each direction in space. These conditions are combined in the Bragg Equation (Eq. 2.3), in which the scattering vector $\boldsymbol{h} = \boldsymbol{k_1} - \boldsymbol{k_0}$ (vector difference between the wave propagation vectors $\boldsymbol{k_0}$ and $\boldsymbol{k_1}$ of

the incident and the diffracted beam, respectively) is connected to the diffraction angle θ at a given radiation wavelength λ.

$$\frac{2\sin\theta}{|\boldsymbol{h}|} = \lambda \tag{2.3}$$

Each diffraction peak (reflection) is therefore given as a vector $\boldsymbol{h}$, defined in a reciprocal-space lattice of inverse length and perpendicular directions to the real-space lattice. Thus, each reflection is characterised by its position, given by the integer components hkl (*Miller indices*) of $\boldsymbol{h}$, and its intensity I. As $\boldsymbol{h}$ is perpendicular to a reciprocal lattice plane, which is defined in the real space by its inverse intersections with the lattice parameters ($\boldsymbol{a}/h$, $\boldsymbol{b}/k$, and $\boldsymbol{c}/l$), the magnitude of $\boldsymbol{h}$ with the lowest hkl defines the spacing between two adjacent lattice planes, $d_{hkl} = 1/|\boldsymbol{h}|$.

While the position of the reflections give the reciprocal-space lattice, from which the metric of the real-space lattice can be determined, the intensity of each reflection is proportional to the squared structure factor: $I(\boldsymbol{h}) \sim |F(\boldsymbol{h})|^2$. The structure factor is defined as the Fourier transform of the electron density in the unit cell:

$$F(\boldsymbol{h}) = \sum_{\nu=0}^{n} f_\nu(\boldsymbol{h}) e^{2\pi i \boldsymbol{h}\cdot\boldsymbol{x_\nu}} \tag{2.4}$$

It is therefore a sum over the scattering amplitudes of all atoms at the position $\boldsymbol{x_\nu}$ in the unit cell multiplied with their atomic form factors $f_\nu(\boldsymbol{h})$, which give a measure for the scattering power of a specific element. The atomic form factor is the Fourier transform of the electron density $\rho(\boldsymbol{x})$ of the electron cloud associated with a single atom:

$$f(\boldsymbol{h}) = \iiint_V \rho(\boldsymbol{x}) e^{2\pi i \boldsymbol{h}\cdot\boldsymbol{x}} d\boldsymbol{x} \tag{2.5}$$

As $f(\boldsymbol{h})$ is a function of $\boldsymbol{h}$ it is dependent upon the scattering angle, i.e. $f(\boldsymbol{h})$ is damped with larger scattering angles. For X-rays the scattering power scales with the number of electrons surrounding the atom, thus light elements like oxygen have a very small scattering power and do not contribute much to the structure factor.

The $I(\boldsymbol{h}) \sim |F(\boldsymbol{h})|^2$ relationship leads to a general issue of diffraction, the phase problem. The phase information needed to obtain the atomic positions via an inverse Fourier transform of the structure factor is lost in the measured intensities due to the squared relationship. Thus, a direct estimate of atomic positions from the measured reflections is not possible. However, if a structure model is known, it can be refined to the data by least-squares algorithms Giacovazzo et al. (1992).

2.1.2 Neutron diffraction

Neutrons are scattered at the nucleus rather than the electron cloud. The measured intensity is proportional to the differential scattering cross section: $I(\boldsymbol{h}) \sim d\sigma/d\Omega(\boldsymbol{h})$, where $d\sigma$ is the scattered flux into the solid angle $d\Omega$ over the incident flux. The scattering cross section equals the squared scattering amplitude $|A(\boldsymbol{h})|^2$ which is defined similarly to the structure factor for X-rays as

$$A(\boldsymbol{h}) = \sum_{\nu=0}^{n} b_\nu e^{2\pi i \boldsymbol{h}\cdot\boldsymbol{x_\nu}} \tag{2.6}$$

where b_ν is the neutron scattering length, depending on the isotope and on the relative nuclear spin orientations. Because the different isotopes of a given element are randomly distributed over all sites and the nuclear spin orientation is also random, an average distribution of the scattering length substitutes for b_ν in Eq. 2.6, leading to a squared amplitude of

$$|A(\boldsymbol{h})|^2 = \sum_{\nu=0}^{n}\sum_{\mu=0}^{n} \left\langle b_\nu b_\mu^* \right\rangle e^{2\pi i \boldsymbol{h}\cdot(\boldsymbol{x_\nu}-\boldsymbol{x_\mu})} \tag{2.7}$$

The distribution of the scattering length on the different sites is completely uncorrelated, thus, only for $\nu = \mu$ there is a correlation leading to an additional term describing the mean quadratic deviation from the average:

$$\langle b_\nu b_\mu \rangle = \begin{cases} \langle b\rangle\langle b\rangle = \langle b\rangle^2 & \nu \neq \mu \\ \langle b^2\rangle = \langle b\rangle^2 + \langle (b-\langle b\rangle)^2\rangle & \nu = \mu \end{cases} \tag{2.8}$$

Therefore, the differential neutron cross section becomes a sum of two terms:

$$\frac{d\sigma}{d\Omega}(\boldsymbol{h}) = \langle b\rangle^2 \left| \sum_{\nu=0}^{n} e^{2\pi i \boldsymbol{h}\cdot\boldsymbol{x_\nu}} \right|^2 + N\left\langle (b-\langle b\rangle)^2 \right\rangle \tag{2.9}$$

The first term contains the phase factors resulting from coherent interference of pairs of scatterers, thus it is named *coherent scattering* and is analog to the structure factor for X-rays. The second term corresponds to scattering from single atoms which superimpose incoherently, thus it is named *incoherent scattering* and is proportional to the number of atoms N. Because incoherent scattering contributes to the background, samples containing hydrogen are usually deuterated in order to solve their structure as hydrogen scatters mainly incoherently.

In contrast to the atomic form factor for X-rays, the coherent scattering lengths do not depend on the scattering angle and their values vary non-systematically with atomic weight. This has the advantage that light isotopes, for example ^{16}O, have stronger scattering power for neutrons as compared to X-rays, thus oxygen atoms can be detected more easily among heavy metal isotopes.

Neutrons are real particles having a rest mass m_n and a momentum $\boldsymbol{p}_n = m_n \boldsymbol{v}_n$. According to wave-particle duality, a beam of neutrons with a velocity $\boldsymbol{v}_n$ can be considered as waves with a *de Brouglie* wavelength $\lambda_n = \hbar/(v_n m_n)$ and a wavevector $\boldsymbol{k}_n = \boldsymbol{v}_n m_n/\hbar$. For a diffraction process, Bragg's law (see Eq. 2.3) determines the relationship between λ_n, θ, and $\boldsymbol{h} = \boldsymbol{k}_{n,\mathrm{out}} - \boldsymbol{k}_{n,\mathrm{in}}$. Given the above equations for λ_n and $\boldsymbol{k}_n$, the Bragg's law can be rewritten to relate the neutron time-of-flight t with the lattice spacing d_{hkl}:

$$t\ (\mathrm{ms}) = 505.56 \cdot L\ (\mathrm{m}) \cdot d_{hkl}\ (\text{Å}) \cdot \sin\theta \tag{2.10}$$

where L denotes the total flight path of the neutrons.

It should be mentioned that neutrons also interact with magnetic moments allowing for the diffraction on and determination of magnetic lattices. As this is not relevant for the present study, it is not discussed here.

2.1.3 The Rietveld method

The Rietveld method allows to determine the crystal structure from powder diffraction data via a refinement of an initial structure model to the diffraction pattern using the least-squares algorithm (Rietveld, 1969). A powder diffraction pattern consists of three arrays $\{T_i, y_i, \sigma_i\}_{i=1,\ldots,n}$, where T_i is the diffraction variable (diffraction angle, neutron TOF, or energy), y_i is the profile intensity at T_i, and σ_i is with the standard deviation of y_i. The pattern can be calculated with the intensity y_i^c at each T_i according to

$$y_i^c = \sum_{p=1}^{N_p} S_p \sum_{\boldsymbol{h}} I_{p,\boldsymbol{h}} \Omega(T_i - T_{p,\boldsymbol{h}}) + b_i \tag{2.11}$$

where p denotes the phase varying from 1 to the number of phases N_p, S_p is the phase scale factor, $I_{p,\boldsymbol{h}}$ denotes the intensity of a given reflection of phase p, $\Omega(T_i - T_{p,\boldsymbol{h}})$ is the profile function of the given reflection that models instrumental and sample effects, and b_i is the added background function. Several factors determine the calculated reflection intensity, i.e. $I_{p,\boldsymbol{h}} = \{LAPCF^2\}_{p,\boldsymbol{h}}$, where $L_{p,\boldsymbol{h}}$ contains the Lorentz-polarisation correction as well as

the multiplicity factors, $A_{p,\boldsymbol{h}}$ is the absorption correction, $P_{p,\boldsymbol{h}}$ is the preferred orientation correction, $C_{p,\boldsymbol{h}}$ includes other corrections like extinction, and $F_{p,\boldsymbol{h}}$ denotes the structure factor.

For neutron time-of-flight data, a special zero-shift correction has to be applied (Larson and Von Dreele, 2004):

$$t = \mathrm{DIFC} \cdot d_{hkl} + \mathrm{DIFA} \cdot d_{hkl}^2 + \mathrm{ZERO} \tag{2.12}$$

where $\mathrm{DIFC} = 505.56 L \sin\theta$ after Eq. 2.10, DIFA and ZERO are the d_{hkl}-dependent and independent zero-shift corrections.

A structure model can be refined to the powder diffraction data by minimising the χ^2 sum

$$\chi^2 = \sum_{i=1}^{n} \frac{1}{\sigma_i^2} \left[y_i - y_i^c(\boldsymbol{\alpha}) \right]^2 \tag{2.13}$$

for the parameter vector $\boldsymbol{\alpha}$ containing the structural parameters as well as the profile and correction parameters. In order to determine the quality of the refinement, a weighted profile factor R_{wp} (Eq. 2.14) is commonly used.

$$R_{wp} = 100 \left[\frac{\sum_{i=1}^{n} \frac{1}{\sigma_i^2} |y_i - y_i^c|^2}{\sum_{i=1}^{n} \frac{1}{\sigma_i^2} y_i^2} \right]^{\frac{1}{2}} \tag{2.14}$$

In order to compare the quality of refinements of different models to the same experimental data, the reduced $\chi_\nu^2 = \chi^2/(n-p)$ is used, where n is the number of data points and p is the number of parameters used in the refinement. Thus, χ_ν^2 is normalised to the degree of freedom $(n-p)$ and is therefore comparable between models having an unequal number of parameters.

2.1.4 Equation of State

An EoS describes the relation between a matter property such as volume (V) and a physical condition such as temperature (T) and pressure (P). Since an EoS is not based on definitive thermodynamic principles, there are many empirically formulated EoS describing a specific relationship in a limited range of the physical condition involved. There is no single EoS, which can predict the behaviour of all matter properties under all physical conditions.

There are four types of EoS describing the relation between volume and pressure (Angel et al., 2000): the Murnaghan, Natural Strain, Birch-Murnaghan, and Vinet EoS. In most

cases, the P-V relation is expressed in terms of the isothermal bulk modulus K and its pressure derivatives K' and K'', defined as

$$K = -V\left(\frac{\partial P}{\partial V}\right)_T, \quad K' = \left(\frac{\partial K}{\partial P}\right)_T, \quad K'' = \left(\frac{\partial^2 K}{\partial P^2}\right)_T \tag{2.15}$$

The BM-EoS (Birch, 1947) is well established for fitting P-V data obtained by high-pressure diffraction and is accurate up to 10 % compression. It expresses the compressional strain energy as a Taylor series expansion of the finite Eulerian strain f_E defined as:

$$f_E = \frac{\left[\left(\frac{V_0}{V}\right)^{\frac{2}{3}} - 1\right]}{2} \tag{2.16}$$

where V_0 is the volume at ambient pressure. Expansion of the free Gibbs energy in terms of f_E truncated at the fourth-order term yields the following BM-EoS, i.e. P as a function of f_E:

$$P = 3K_0 f_E\,(1+2f_E)^{\frac{5}{2}}\left[1+\frac{3}{2}(K_0'-4)f_E+\frac{3}{2}\left(K_0K_0''+(K_0'-4)(K_0'-3)+\frac{35}{9}\right)f_E^2\right] \tag{2.17}$$

where the fitting parameters V_0, K_0, K_0', and K_0'' are the isothermal ambient-pressure values for the unit-cell volume as well as the bulk modulus and its pressure derivatives, respectively.

However, not all materials require a full fourth-order equation in order to fit their P-V dependence properly. In such cases a truncated form of the equation can be used. The third-order truncation fixes $f_E^2 = 0$, thus only V_0, K_0, and K_0' remain as fit parameters, whereas the value of K_0'' is determined by the other parameters (Anderson, 1995):

$$K_0'' = -\frac{1}{K_0}\left((3-K_0')(4-K_0')+\frac{35}{9}\right) \tag{2.18}$$

The second-order truncation fixes also $f_E = 0$, therefore only V_0 and K_0 remain as refinable parameters, whereas K_0' is fixed to 4 and K_0'' is ignored.

The actual fitting of the BM-EoS to the P-V data is accomplished using the program *EoSFit* (Angel, 2000). It uses a least squares algorithm, minimising the weighted χ^2 sum for m parameters and n data points:

$$\chi_w^2 = \frac{1}{n-m}\sum_{i=1}^{n} w_i\left(P_i^{\mathrm{obs}} - \mathrm{EoS}(V_i^{\mathrm{obs}})\right)^2 \tag{2.19}$$

Each data point has a weight defined by the effective variance method:

$$w_i = \frac{1}{\sigma^2} = \frac{1}{\sigma_P^2 + \sigma_V^2 \left(\frac{K}{V}\right)^2} \tag{2.20}$$

In order to graphically evaluate the BM-EoS, the normalised pressure F (Eq. 2.21) is plotted against the finite Eulerian strain f_E, leading to the f-F plot.

$$F = \frac{P}{[3f_E(1+2f_E)]^{\frac{5}{2}}} \tag{2.21}$$

The order of the BM-EoS can easily be seen in the f-F plot. A second-order BM-EoS plots as a horizontal straight line, a third-order BM-EoS plots as an inclined straight line, and a fourth-order BM-EoS plots as a polynomial curve. In addition, small changes in the volume compressibility, which usually indicate a phase transition, are easily seen in the f-F plot as change in slope, whereas they might be hardly deduced from the P-V dependence. It should be noted that the uncertainties of f_E are usually so small that they can be ignored, whereas those of F are large at low pressures and decrease with increasing pressure.

2.2 Temperature-dependent diffraction experiments

2.2.1 High-resolution powder X-ray diffraction

Low-temperature powder XRD experiments were conducted between 20 and 300 K by using a house-developed (Ihringer, 1982) high-resolution powder diffractometer (Fig. 2.1a), operating in Guinier geometry (Fig. 2.1b) and with Cu-$K_{\alpha 1}$ radiation of wavelength $\lambda = 1.54059$ Å. The diffractometer is equipped with a Huber 670G image plate covering a 2θ-range of 4–100° with a resolution of 0.005° and a closed-cycle helium cryostat. The mean exposure time is 15 minutes with a read-out time less than 1 minute. The standard deviations of the measured intensities (Eq. 2.22) were empirically determined using a statistical distribution of intensities obtained from a LaB_6 standard.

$$\sigma = \sqrt{k(I-b) + \sigma_{2\theta}^2 \left(\frac{dI}{d2\theta}\right)^2} \tag{2.22}$$

where k is a diffractometer-specific parameter, b is a constant subtracted background, and $\sigma_{2\theta}$ the uncertainty in 2θ. The sample powder is fixed between two Kapton foils pressed into a sample holder which is rotated during the exposure time in order to improve the

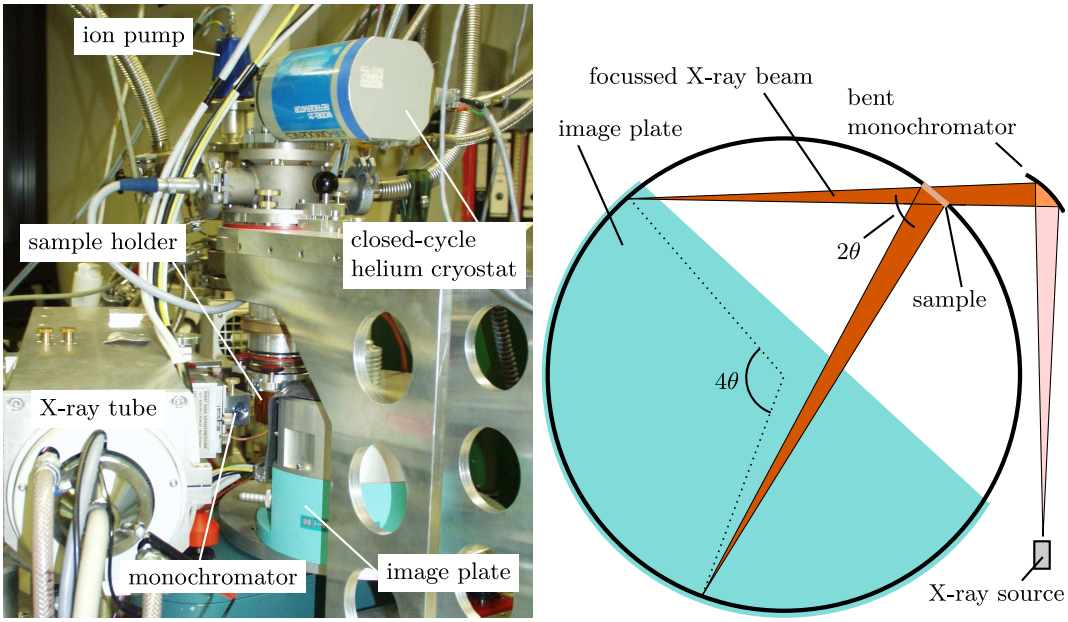

(a) Low-temperature Guinier camera.

(b) Beam path of transmission Guinier geometry.

Figure 2.1: Low-temperature Guinier camera of the Institut für Angewandte Physik, Universität Tübingen (a). The beam path of the Guinier geometry is illustrated in (b).

statistical distribution of the powder particles. As the sample chamber is put under ultra-high vacuum using an ion pump, the sample rotation is achieved via a magnetic-coupled motor. Note, that the sample chamber is flooded with helium in order to improve the cooling efficiency.

The samples were cooled down with a cooling rate of 1 K/min and a holding time of 15 minutes in order to settle temperature oscillations. The acquisition time was 30 minutes and patterns were collected in steps of 5–10 K.

High-temperature powder XRD measurements in the range of 300–1000 K were performed with a Philips X'Pert PW3020 diffractometer (Fig. 2.2a) operating in θ–2θ Bragg-Brentano geometry illustrated in Fig. 2.2b. The diffractometer was equipped with an Anton Paar high-temperature cell with a steel or platinum sample band. The temperature scale was calibrated ex-situ with a thermocouple. Powder patterns were collected upon cooling in a 2θ range of 15–84° with a step size of 0.02°. The accumulation time varied between 4 and 10 s/step with 2:1 Cu-$K_{\alpha 1}$–Cu-$K_{\alpha 2}$ radiation of wavelengths $\lambda_1 = 1.54059$ Å and $\lambda_2 = 1.54443$ Å, respectively.

The low- and high-temperature data were subsequently fitted by Rietveld refinement carried out by using the program SIMREF (Maichle et al., 1988) and the graphical

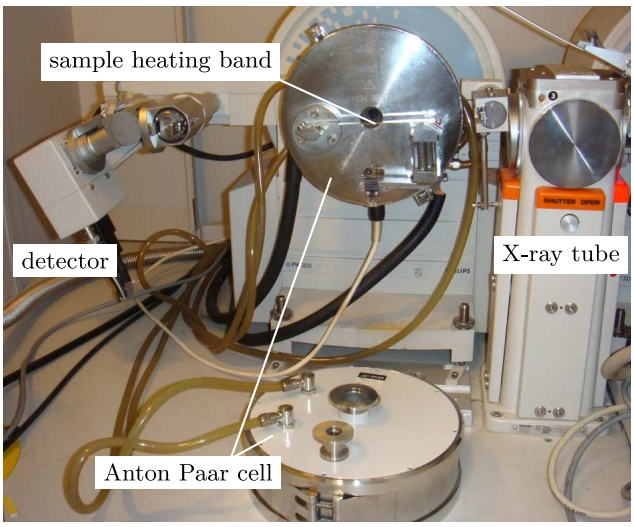

(a) Philips X'pert PW3020 powder diffractometer.

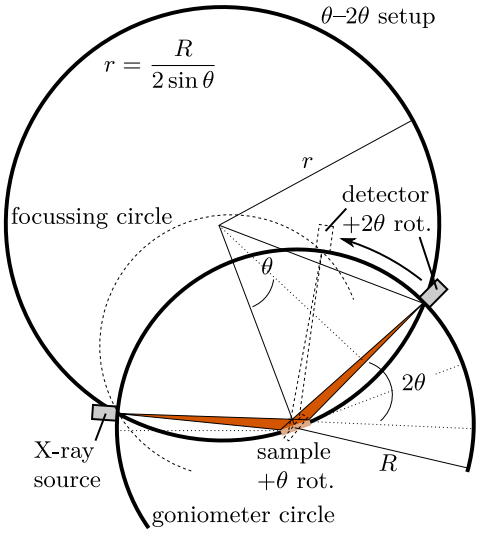

(b) Beam path of the θ–2θ Bragg-Brentano geometry.

Figure 2.2: The Philips X'Pert PW3020 Bragg-Brentano powder diffractometer (a) with a θ–2θ setup, equipped with an Anton-Paar high-temperature cell. The beam path of the θ–2θ Bragg-Brentano geometry is illustrated in (b).

user interface QSIMREF developed by the author (Maier, 2007). Built-in temperature-dependent calibration of the 2θ scale on an internal silicon standard was applied for a precise determination of unit-cell parameters:

$$2\theta_i^{\text{corr}} = 2\theta_i + \sum_{n=0}^{2} t_n (2\theta_i)^n \tag{2.23}$$

where t_0, t_1, and t_2 are refinable parameters.

For refinements to the data collected with the Huber image plate in Guinier geometry, a pseudo-Voigt function was used for the peak shape:

$$P(x_{i,k}) = \eta L(x_{i,k}) + (1 - \eta) G(x_{i,k}) \tag{2.24}$$

where $x_{i,k} = 2\theta_i - 2\theta_k$ of the ith data point and kth Bragg reflection, $L(x_{i,k})$ is a Lorentzian function, and $G(x_{i,k})$ is a Gaussian function. The weight-coefficient parameter η is considered as a Taylor expansion to the second order of 2θ:

$$\eta(2\theta) = \eta_0 + \eta_1(2\theta) + \eta_2(2\theta)^2 \tag{2.25}$$

where η_0, η_1, and η_2 are refinable parameters. Both peak shape functions have the same FWHM after Caglioti et al. (1958):

$$H_{hkl}(\theta_{hkl}) = \sqrt{U \tan^2 \theta_{hkl} + V \tan \theta_{hkl} + W} \tag{2.26}$$

where U, V, and W are refinable parameters. A correction factor for the asymmetric peak shape was used after Bérar and Baldinozzi (1993):

$$A(x_{i,k}) = 1 + \left(\frac{A_0}{\tan\theta} + \frac{A_1}{\tan 2\theta}\right) 2x_{i,k} e^{-x_{i,k}^2} + \left(\frac{B_0}{\tan\theta} + \frac{B_1}{\tan 2\theta}\right) (8x_{i,k}^3 - 12x_{i,k}) e^{-x_{i,k}^2} \tag{2.27}$$

where A_0, A_1, B_0, and B_1 are refinable parameters. Further details can be found in the Ritter et al. (2003).

For refinements to the data collected in Bragg-Brentano geometry, a pseudo-Voigt function corrected to peak asymmetry due to axial divergence after Finger et al. (1994) was used. The asymmetric peak shape is modelled with two parameters, S/L and H/L, where $2S$ is the finite sample size, $2H$ the detector size, and L the sample-to-detector distance.

2.2.2 Synchrotron single-crystal X-ray diffraction

In order to measure the weak diffuse scattering arising from PNR (see Sec. 1.3.4) at different temperatures, as well as the weak reflections arising from chemical B-site ordered domains, synchrotron single-crystal XRD experiments were conducted at the beamline F1 at HASYLAB/DESY. The beamline is equipped with a Huber 4-circle diffractometer with κ-geometry (see Figs. 2.3a and 2.7), providing a photon flux of 10^{11} mm^{-2}s^{-1} on the sample. Low-temperature measurements were conducted using an Oxford Cryosystems Cryostream 600 device (Fig. 2.3a), having a temperature range of 90–370 K with a temperature stability of $\pm$0.1 K. High-temperature data collections were performed using an in-house developed N_2 gas-stream heating device (Fig. 2.3b), having a temperature range 300–1200 K with a stability of $\pm$4 K.

Single-crystal XRD experiments were conducted at different temperatures with a Mar-CCD 165 detector, using high-energy radiation with a wavelength of $\lambda = 0.4000$ Å. In order to determine the unit-cell parameters and the UB matrix with the program XDS (Kabsch, 1988, 1993), ϕ-rotation diffraction data were collected with a sample-to-detector distance of 60 mm, a ϕ-step width of 1° per frame, and an exposure time of 15 s. The data of subsequent long-exposure collections (exposure times of 150–220 s, detector distance of 100 mm, and a ϕ-step width of 0.5° per frame) were unwarped to reciprocal space layers

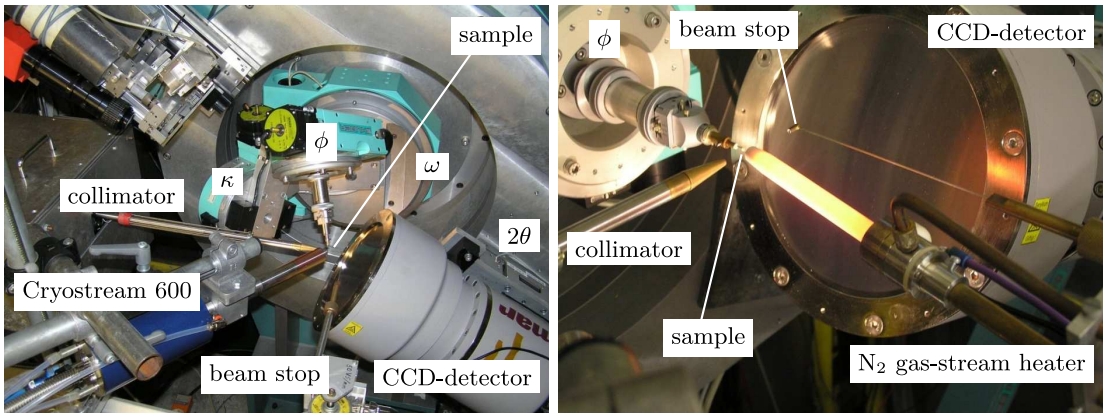

(a) Oxford Cryosystems Cryostream 600.

(b) In-house developed N_2 gas-stream heating device.

Figure 2.3: Four-circle Kappa-diffractometer of F1 beamline at HASYLAB/DESY operating at low (a) and high (b) temperatures. Pictures were taken from the HASYLAB website (2009) and modified by the author.

using the program RASTM (Paulmann and Malcherek, 2006) by utilising the previously determined UB matrix of the short-exposure data. Prior to the data processing, the raw data frames were scaled to the synchrotron decay of the primary beam intensity by using the program SCLMAR, part of the MarToolsCP-package (Paulmann and Malcherek, 2006). The unwarped data were visualised with KUPLOT which is part of the DISCUS program package (Proffen and Neder, 1997).

2.3 High-pressure diffraction experiments

2.3.1 The diamond-anvil-cell technique

The DAC was developed as a simple tool to study materials under high pressures up to 100 GPa (Basset, 2009). As pressure is defined as force over area ($P = F/A$), it is necessary to keep A small in order to reach high pressures with reasonable forces. Fig. 2.4 shows a schematic view of the working principle of a DAC device. The diamond anvils are pressed by mechanical force against a preindented metal gasket, containing the sample in a drilled hole within the indented area. Thus, the sample chamber is put under uniaxial stress which is transformed to hydrostatic pressure within the chamber volume by the pressure-transmitting medium, which can be a solid, a liquid, or a gas. A common liquid medium is a 4:1 methanol–ethanol mixture ensuring hydrostatic conditions up to 9.8 GPa (Angel et al., 2007). However, the pressure medium has to be inert regarding the sample,

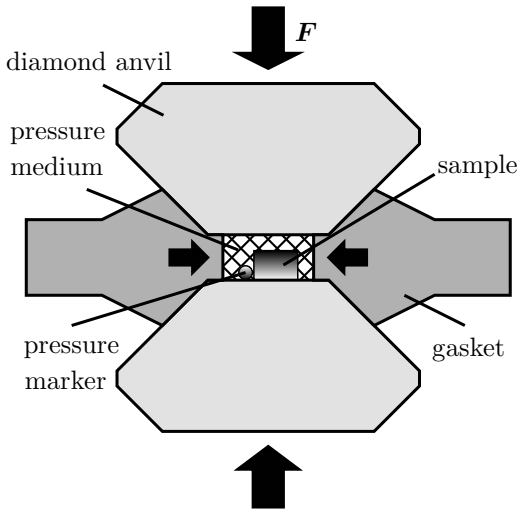

Figure 2.4: Schematic view of the diamond anvil cell. The diamond anvils apply uniaxial pressure on the gasket. The pressure medium ensures hydrostatic pressure conditions inside the sample volume.

limiting the choices of pressure media in some experiments. Table 2.1 gives an overview of common pressure media with their effective hydrostatic limits.

The role of the gasket is two-fold: to ensure a chamber for the sample and the pressure medium and to support the diamond anvils in order to reduce stress at the edges of the culets (Eremets, 1996). Thus, it is usually made of a hard metal which is typically stainless steel. In order to reduce the level of background scattering in a XRD experiment, X-ray absorbing metals like tungsten or rhenium can be used (Angel, 2000). In addition, special gaskets were developed, e.g. a X-ray transparent composite gasket based on Kapton, amorphous boron, and epoxy (Merkel and Yagi, 2005).

Table 2.1: Pressure-transmitting media with their effective hydrostatic limits after Miletich et al. (2000); Angel et al. (2007).

pressure-transmitting medium	hydrostatic limit (GPa)
silicone oil	0.9
glycerol	1.4
argon	1.9
nitrogen	3.0
4:1 methanol–ethanol	9.8
16:3:1 methanol–ethanol–water	10.5
helium	70
hydrogen	177

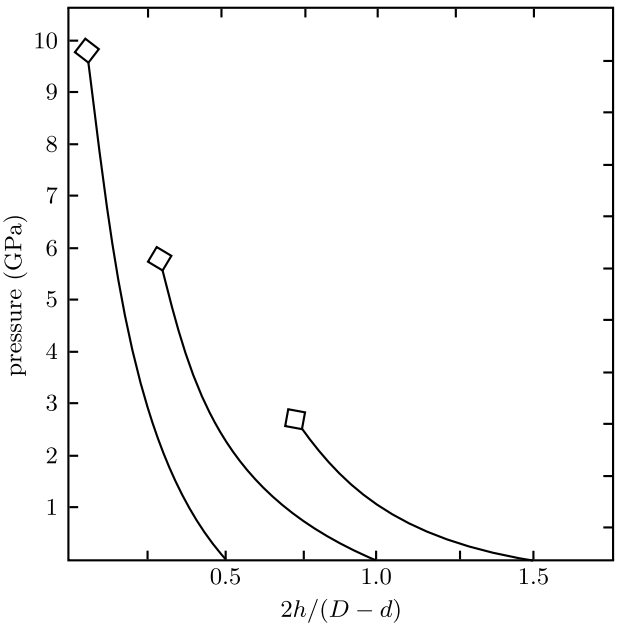

Figure 2.5: Simplified diagram of the relationship between sample chamber dimensions and attainable pressure after (Katrusiak, 2008), where h is the height and d the diameter of the sample chamber, and D is the diameter of the culets. The maximum attainable pressure is marked with an open diamond.

The standard procedure for preparing gaskets for the experiment is to use a thicker metal foil than needed and to preindent it to the desired thickness. The preindentation has several advantages: the gasket material is work-hardened during the indentation process, it allows controlling the gasket height, and it improves the sample chamber sealing during initial pressure generation (Katrusiak, 2008). Once the gasket is indented to the desired thickness, the sample chamber has to be drilled as a small hole in the centre of the preindented area (see Appx. A.4). The preindented gasket has to be removed from the cell for the drilling process, thus all DACs used in this work (see Appxs. A.1, A.2, and A.3) ensure a unique gasket position, which also allows for measuring the gasket thickness during the indentation process. The highest pressure that can be achieved during the experiment is inversely proportional to the ratio $r = 2h/(D - d)$, where h and d are height and diameter of the sample chamber, respectively, whereas D is the diameter of the culets (Katrusiak, 2008). Figure 2.5 shows a simplified diagram of that relationship after Katrusiak (2008). In order to reach for example 10 GPa, r should be 0.5 or less. Therefore, for a culet diameter of 600 μm and a hole diameter of 270 μm, the gasket has to be preindented to a thickness of 82.5 μm in order to achieve 10 GPa. Certainly, this relation puts restrictions on the sample size, as the thickness of the chamber at 10 GPa is reduced to approximately 20–25 μm.

Pressure in the cell is usually determined with an internal pressure standard. The most common method for pressure calibration is the use of the ruby fluorescence (Forman et al., 1972). The $R_{1,2}$-doublet (at 694.2 nm and 692.7 nm for ambient conditions, respectively) shifts with a linear pressure dependence under hydrostatic conditions up to 20 GPa according to $\Delta P = 0.2740(16)\Delta\lambda$ GPa, where the line shift $\Delta\lambda$ is given in Å (Piermarini et al., 1975). Mao et al. (1986) improved the calibration curve proposing the relation:

$$\Delta p = 1904 \left[\left(\frac{\lambda}{\lambda_0} \right)^B - 1 \right] \frac{1}{B} \tag{2.28}$$

where λ_0 is the position of the R_1 line measured at ambient conditions, $B = 7.655$ for quasi-hydrostatic conditions and $B = 5$ for non-hydrostatic conditions, extending the ruby fluorescence scale up to 80 GPa.

Pressure determination with the ruby fluorescence is a quick and simple procedure, however, the precision of the method is of the order of ±0.03 GPa (Angel et al., 1992). For diffraction experiments which measure the volume with a precision of 1 part in 10000 (see Sec. 2.3.2), an internal diffraction standard with a well-known equation of state such as CaF_2 (Hazen and Finger, 1981; Angel, 1993) or SiO_2 (Angel et al., 1997) can be used to precisely determine pressure. The use of quartz in such diffraction experiments allows for pressure determination with a precision of ±0.004 GPa at 1 GPa, ±0.006 GPa at 5 GPa, and ±0.009 GPa at 9 GPa (Angel et al., 1997).

There are many designs of DACs (Eremets, 1996), each suited best for specific measurements. The high-pressure studies in this work were performed with DACs of *ETH* design (Miletich et al., 2000) for in-house *P-V* measurements and of *Boehler-Almax* (Boehler, 2006) and *Ahsbahs* design (Ahsbahs, 2004) for synchrotron experiments. See Appx. A for a detailed description of the DACs used and the sample loading procedure.

2.3.2 High-pressure single-crystal X-ray diffraction

Precise measurements of the volume compressibility were conducted at the *Crystallography Laboratory, Virginia Tech, USA* by high-pressure single-crystal XRD on a Huber 4-circle diffractometer (Fig. 2.6), equipped with a Eulerian cradle and a point detector. Sample crystals with an approximate size of 80×80×30 μm were loaded next to a quartz crystal used as a pressure calibrant into an ETH-DAC with a culet diameter of 600 μm. Gaskets made of a 250 μm thick T301 steel foil were preindented to a thickness of 90–100 μm. A hole of 300 μm in diameter was drilled into the centre of the indented area. A mixture

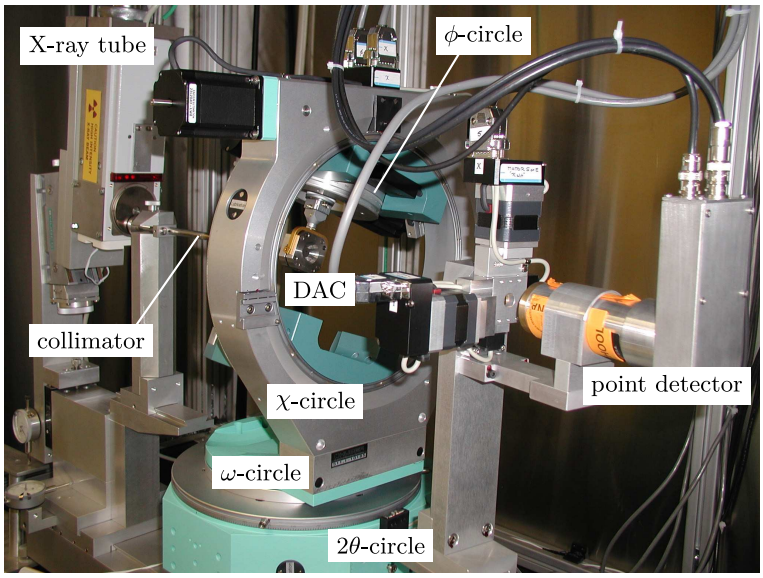

Figure 2.6: Huber 4-circle diffractometer at *Crystallography Laboratory, Virginia Tech, USA*, equipped with an Eulerian cradle (Angel, 2008).

of 4:1 methanol–ethanol was used as a pressure-transmitting medium in order to ensure hydrostatic conditions up to 9.8 GPa. The unit-cell volume was measured for a minimum of 12 pressure points up to 10 GPa and an BM-EoS of third-order was subsequently used to fit the P-V data with the program EOSFIT (Angel et al., 2000)

The diffractometer is driven by the SINGLE software (Angel, 2000), a setup allowing for the determination of the unit-cell volume with a precision of 1 part in 10000. As the sample is measured in a DAC, an optical alignment of the crystal in beam direction is only possible via the focus of the alignment telescope, as the DAC laterally restricts visual access to the sample. Thus, the high accuracy in crystal alignment needed for measuring the unit-cell volume with the precision given above is not possible with optical methods. Therefore, a set of reflections is measured with the eight-position diffracted beam centring method (King and Finger, 1979). The latter eliminates experimental aberrations such as the offset of the crystal from the centre of the goniometer, incorrect zero positions of the 2θ, ω, and χ circles, and more (Angel, 2000). The same procedure is applied to the standard quartz crystal placed next to the sample. Due to the precision of the unit-cell volume, pressure can be determined from the known EoS of quartz with an error of $\pm$0.004–0.009 GPa.

The exact procedure is as follows. The crystal in the DAC has to be centred optically along the x and z direction (coordinate system after Busing and Levy (1967)). The y

Table 2.2: Reflection positions for the eight-position diffracted beam centring used in the centring routing of the SINGLE software.

position	diffractometer angles			
1	2θ	ω	χ	ϕ
2	-2θ	ω	χ	ϕ
3	-2θ	$-\omega$	$\pi+\chi$	ϕ
4	2θ	$-\omega$	$\pi+\chi$	ϕ
5	2θ	$-\omega$	$\pi-\chi$	$\pi+\phi$
6	-2θ	$-\omega$	$\pi-\chi$	$\pi+\phi$
7	-2θ	ω	$-\chi$	$\pi+\phi$
8	2θ	ω	$-\chi$	$\pi+\phi$

direction can be roughly centred by the focus of the camera. Subsequently, an initial UB matrix is calculated from known unit-cell parameters (previously measured in air or extrapolated from different pressures) and the precise position of two reflections determined by a two-position centring procedure at $+2\theta$ and -2θ.

Once the UB matrix is determined, a set of reflections is centred using the eight-position beam diffracting centring routine. Each reflection is measured at the eight positions given in Tab. 2.2. For this purpose, iterative step scans are carried out in order to maximise the reflection intensity in the detector. The scan sequence is ω, ω–2θ, ω, χ, and ω again, where each scan consists of nine steps and the scan width in ω is narrowed each step. Subsequently, a fine χ scan with $\sim$30 steps is performed and the position of the peak maximum, A_i, $i = 1, \ldots, 8$ (see Eq. 2.29), is determined using a Gaussian peak fit. Finally, a fine ω scan with typically 51 steps with $\chi = A_i$ is conducted and the peak position, intensity, and FWHM are determined by a subsequent least-squares fit to a pair of pseudo-Voigt functions, describing the α_1 and α_2 contributions, respectively. This procedure is repeated for each of the eight equivalent reflection positions. The correct diffraction angles for the eight-position centred reflection are then given as

$$\begin{aligned} 2\theta_{\mathrm{ref}} &= (D_1 - D_2 - D_3 + D_4 + D_5 - D_6 - D_7 + D_8)/4 \\ \omega_{\mathrm{ref}} &= (D_1 + D_2 - D_3 - D_4 - D_5 - D_6 + D_7 + D_8)/8 \\ \chi_{\mathrm{ref}} &= (A_1 + A_2 + A_3 + A_4 - A_5 - A_6 - A_7 - A_8)/8 \end{aligned} \tag{2.29}$$

where $D_i = \omega + \theta$ is the observed absolute ω value and A_i is the observed χ value of the ith centring position.

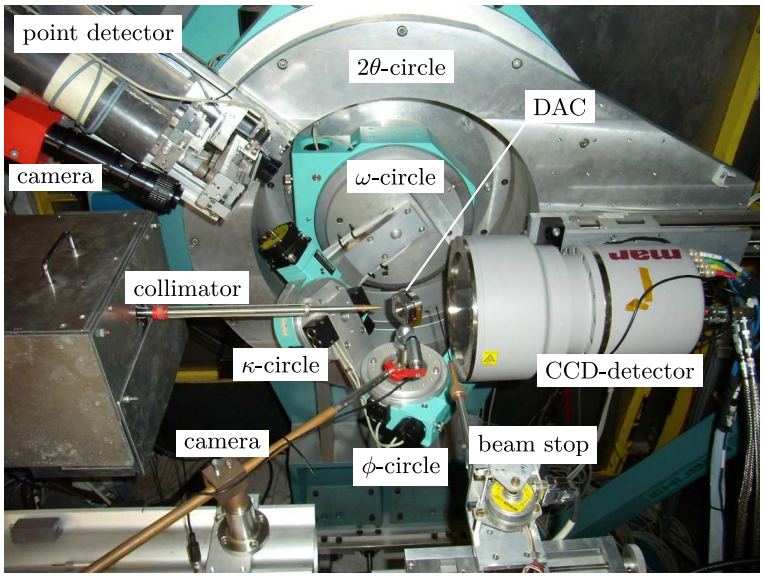

Figure 2.7: 4-circle Kappa-diffractometer of the F1 beamline at HASYLAB/DESY.

The unit-cell parameters are subsequently determined by a symmetry-constrained vector-least-squares fit after Ralph and Finger (1982) which is implemented in the SINGLE software using the determined reflection angles given by Eq. 2.29.

2.3.3 Synchrotron high-pressure single-crystal X-ray diffraction

In order to measure pressure-dependence of the weak diffuse scattering arising from PNR (see Sec. 1.3.4), synchrotron high-pressure single-crystal XRD experiments were conducted at the F1 beamline at HASYLAB/DESY (see also 2.2.2), using DACs of Boehler-Almax, Ahsbahs, and ETH type. Stainless steel gaskets were preindented to a thickness of 90–100 μm and a hole of 270 μm was drilled into the centre of the indented area. Crystals with a mean size of 100×100×40 μm cut from polished $\langle 100 \rangle$ plates were oriented on the culet in such a way that one of the cubic axis is parallel to the rotation axis, allowing best access to the (hk0) reciprocal space layer. In addition, crystals cut from polished $\langle 110 \rangle$ plates were oriented with the in-plane cubic axis parallel to the rotation axis in order to gain best access to (hhh), $h = n$, reflections. A 4:1 methanol–ethanol mixture was used as pressure-transmitting medium and the ruby fluorescence method to determine pressure (see Sec. 2.3.1).

The measurements were conducted using a high-energy radiation of wavelength $\lambda =$ 0.4500 Å for PST-Ba and $\lambda = 0.5000$ Å for all the other compounds. The DAC was mounted upright on the goniometer head with its face perpendicular to the beam direction

circle	κ-angles ($\alpha = 60°$)	Eulerian angles	κ-angles ($\alpha = 50°$)
2θ	0.000°	0.000°	0.000°
ω	35.264°	0.000°	57.045°
κ	-109.471°	–	-134.756°
χ	–	-90.000°	–
ϕ	125.264°	90.000°	57.045°

Table 2.3: Conversion of diffractometer angles in κ-geometry between α-angle settings ($\alpha = 60°$ at F1 and $\alpha = 50°$ as standard setting used in the CrysAlis software). Note that a ϕ-offset of +90° was applied to the ϕ-circle at F1 in order to compensate for different axis definitions.

(see Fig. 2.7). The data frames were collected with a ϕ-step width of 0.5° and subsequently scaled to the synchrotron decay of the primary beam intensity using the program SCLMAR (Paulmann and Malcherek, 2006). The scaled frames were converted to a readable format for CrysAlis (Oxford Diffraction, 2009) using the program M2OXL (Paulmann and Malcherek, 2006). As the F1 diffractometer has a kappa arm angle of $\alpha = 60°$, the corresponding diffractometer angles were then converted to the standard setting of $\alpha = 50°$ (see Tab. 2.3).

The data were indexed according to space group $Fm\bar{3}m$ and subsequently integrated and unwarped to reciprocal space layers. The integrated intensities were corrected for diamond and gasket absorption using Absorb6.0 (Angel et al., 2004). Structure models were refined to the corrected integrated intensities of PST using SHELX (Sheldrick, 2008).

2.3.4 High-pressure neutron powder diffraction

High-pressure TOF neutron powder diffraction experiments were conducted at the high-pressure powder beamline PEARL (ISIS Annual Report, 1996, 1997) of the ISIS Pulsed Neutron and Muon Source facility (ISIS/RAL website, 2009), located at the *Rutherford Appleton Laboratory*. Figure 2.8a schematically shows the working principle of the pulsed spallation source. A linear particle accelerator feeds a synchrotron ring with bunches of protons produced by an ion source. Subsequently, they are accelerated close to light speed and, when reached sufficient energy, ejected from the ring and shot on a tungsten target. Thus, due to the spallation process in the target, an extremely intense neutron pulse is emitted, which is directed to the experiments after slowing down the neutrons to desired energies.

Due to the pulsed nature of the neutron radiation at ISIS, the flight path of each neutron pulse is known, allowing for a TOF diffraction. Figure 2.8b shows a schematic drawing of

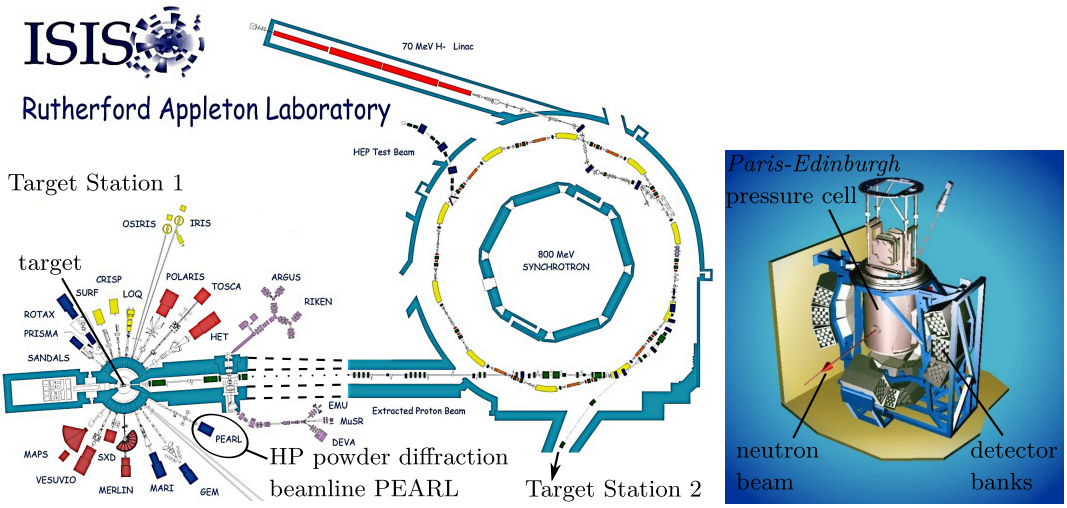

(a) The ISIS/RAL facility.

(b) The instrument PEARL.

Figure 2.8: Schematic view of the ISIS/RAL neutron facility. The pictures were taken from ISIS/RAL website (2009) and modified by the author.

the instrument PEARL. The sample is pressurised using a Paris-Edinburgh pressure cell (Besson et al., 1992; Nelmes et al., 1994) with a modified gasket configuration (Marshall and Francis, 2002). The detector banks consist of ^{7}Li-doped ZnS scintillator modules, which cover a 2θ-range of $83° < 2\theta < 97°$, giving access to d-spacing range of $\sim 0.5 - 4.1$ Å.

The experiments were performed using a perdeuterated 4:1 methanol–ethanol mixture as pressure medium to ensure hydrostatic conditions. Pressure was determined using the EoS (see Sec. 2.1.4) of the samples previously determined by in-house single-crystal XRD measurements (see Sec. 2.3.2).

Structure refinements to the obtained powder patterns were carried out using the Rietveld software package EXPGUI/GSAS (Toby, 2001; Larson and Von Dreele, 2004). The peak shape was refined with the GSAS time-of-flight profile #3 consisting of a convolution of two back-to-back exponentials and a pseudo-Voigt function. The background was fitted using a 12-term cosine Fourier series.

2.4 Complementary methods

2.4.1 Electron probe microanalysis

EPMA was used to determine the chemical composition and homogeneity of the samples characterised in this work. In the EPMA method, a beam of accelerated electrons is focused on the sample surface using electromagnetic lenses with a typical spot size in the order of 1–10 μm. The energy of the electrons must be higher than the element specific excitation energy of the sample, which then emit characteristic X-ray radiation due to inner-electron energy transitions. The electrons are slowed down by the impact on the sample surface, thus the characteristic penetration depth is also in the order of 1–10 μm. The slow-down process gives rise to Bremsstrahlung which contributes to the background intensity.

The concentration of a specific element e in the sample C^e_{sample} can be determined by comparing the measured X-ray emission intensity from the sample I^e_{sample} with the intensity of a standard material I^e_{standard}, having a known concentration C^e_{standard} of the element e:

$$C^e_{\text{sample}} = ZAF \frac{C^e_{\text{standard}}}{I^e_{\text{standard}}} I^e_{\text{sample}} \tag{2.30}$$

where ZAF is a coefficient including corrections for the atomic number dependence of the incident electron penetration, the absorption of X-rays in the sample, and the contribution of fluorescence from other elements.

The detection limit for a specific element is given as the concentration measured at three times the standard deviation of the background intensity from the sample.

$$3ZAF \frac{1}{I^e_{\text{standard}}} \sqrt{\frac{I_b}{t_b}} \text{ (wt. \%)} \tag{2.31}$$

where I_b/t_b is background intensity in cts/s and thus $\sqrt{I_b/t_b} = \sigma_b$ is the standard deviation of the background intensity.

The samples were analysed using a CAMECA SX100 electron microprobe (Fig. 2.9), using an acceleration voltage of 20 kV and a beam current of 20 nA. The beam was focussed to a diameter on the sample surface of $\sim$1 μm and chemical composition was averaged over 50–100 spatial points. The polished sample surface was coated with a thin carbon layer prior to the measurements in order to dissipate electrical surface charging of the sample.

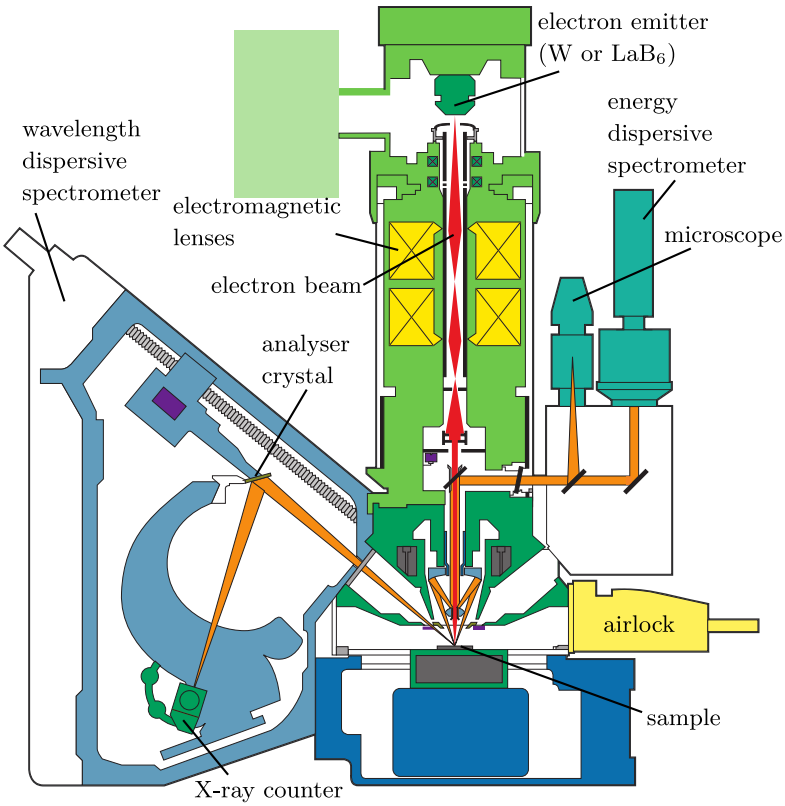

Figure 2.9: Schematic view of the CAMECA SX100 electron microprobe, taken from the CAMECA website (2009) and modified by the author.

2.4.2 Raman spectroscopy

Raman spectroscopy is based on the Raman effect (Raman and Krishnan, 1928) which is essentially inelastic scattering of light by optical vibrational modes (in crystals: optical phonons). An incident laser beam oscillates the electron cloud with the frequency of its electric field, thus an induced dipole moment is created which itself emits radiation with a frequency corresponding to its oscillation frequency. The time-dependent induced dipole moment is given by

$$P = \alpha E_0 \cos(\omega_0 t) \tag{2.32}$$

where α is the polarisability and ω_0 the frequency of the incident light. The polarisability depends on the vibrational energy and thus on the frequency of the vibrational mode which

are related after $E_{\mathrm{vib}} = (j + 1/2)\hbar\omega_{\mathrm{vib}}$, where $\hbar$ is reduced Planck constant and j is the integer vibrational quantum number. Thus, the polarisability equals

$$\alpha = \alpha_0 + \frac{\partial\alpha}{\partial Q} Q_0 \cos(\omega_{\mathrm{vib}} t) \tag{2.33}$$

where Q is the classical atomic displacement amplitude of the given vibrational mode with frequency ω_{vib}. The Substitution of Eq. 2.33 into Eq. 2.32 and the application of the trigonometric sum rule yields

$$P = \underbrace{\alpha_0 E_0 \cos(2\pi\omega_0 t)}_{\mathrm{I}} + \underbrace{\left(\frac{\partial\alpha}{\partial Q}\frac{Q_0 E_0}{2}\right)\left[\cos\left(2\pi\overbrace{(\omega_0 - \omega_{\mathrm{vib}})}^{\text{Stokes}}\, t\right) + \cos\left(2\pi\overbrace{(\omega_0 + \omega_{\mathrm{vib}})}^{\text{anti-Stokes}}\, t\right)\right]}_{\mathrm{II}} \tag{2.34}$$

Thus, induced dipole moments are created at three distinct frequencies ω_0, $\omega_0 - \omega_{\mathrm{vib}}$, and $\omega_0 + \omega_{\mathrm{vib}}$, and hence the incident light is scattered with these frequencies. The first term in Eq. 2.34 describes the so-called Rayleigh scattering, i.e. elastically scattered light. The second term describes the inelastic light scattering from optical phonon modes, namely Raman scattering, consisting of two compounds: the Stokes scattering corresponds to a phonon energy transition from the ground state to an excited virtual state, and vice-verca for anti-Stokes scattering. Usually the Stokes Raman spectra are measured since their intensity is stronger than that of anti-Stokes Raman spectra due to the higher probability of the scattering event. A given vibrational state is Raman active if the value of $\partial\alpha/\partial Q$ is non-zero, i.e. the polarisability must change with vibrational states which are restricted by the symmetry of the molecule or crystal lattice. Thus, the Raman selection rules can be derived from the character table of the given point group, according to group-theory analysis of crystal normal phonon modes.

In a molecule, the number of degrees of vibrational freedom leads to $3N - 6$ ($3N - 5$ for a linear molecule) vibration modes, where N is the number of atoms in the molecule. In the case of a crystal, the atomic vibrations can be considered as normal (standing) elastic waves, with atomic displacements parallel (longitudinal mode) or perpendicular (transverse mode) to the wave vector. There are $3N$ vibrational modes, also referred to as phonons, of which three are acoustic and $3N - 3$ are optic which may be Raman active. Due to the substantial difference between the wavelength of the excitation light ($\sim 10^3 - 10^4$ Å) and the unit-cell parameter ($\sim 1 - 10$ Å) only phonons with wavevector $k \approx 0$, i.e. close to the centre of the *Brillouin zone*[1] can be involved in Raman scattering. Since the process

[1] Brillouin zone: the Wigner-Seitz primitive cell of the reciprocal lattice

of photon-phonon inelastic scattering takes place in a spatial volume of a few angstroms, Raman spectroscopy is ideally for probing the local structure of a crystal.

Depending on the crystal symmetry and experimental geometry, phonon modes give rise to different intensities in the so-called parallel- and cross-polarised Raman spectra, where the polarisation of the scattered light is parallel or perpendicular to the polarisation of the incident light, respectively. The different intensities measured in parallel- and cross-polarised spectra is informative of the phonon mode symmetry. Thus, deviations from the predictions of group theory in the experimental polarised spectra give a deeper insight into the local structural distortion. The experimental scattering geometry is commonly given in the so-called Porto notation $a(bc)d$, where a and d denote the direction of propagation ($\boldsymbol{k}$) of the incident and scattered light, respectively, while b and c denote the direction of polarisation ($\boldsymbol{E}$) of incident and scattered light.

The Raman spectra presented in this work were measured with the triple monochromator system Jobin-Yvon T64000 equipped with an Olympus BH2 microscope. The data were collected in backscattering geometry by using the 514.5 nm line of an Ar^+ laser and a beam power density on the sample surface of 2 kW/mm^2. The Raman scattering was recorded at different temperatures and pressures with a spectral resolution of 2 cm^{-1}. The low- and high-temperature data were collected by using a Cryovac cryogenic system and a LINKAM heating/cooling stage, respectively. In the temperature range of 100–290 K, spectroscopic measurements were performed with both devices to verify the reproducibility of the data. Polarised spectra in Z(XX)$\overline{\text{Z}}$ and Z(XY)$\overline{\text{Z}}$ scattering geometries were collected at each temperature, where X, Y, and Z are parallel to the cubic $\langle 100 \rangle$ crystallographic directions. The as-measured Raman spectra were subsequently reduced by the Bose-Einstein phonon occupation factor in order to eliminate the temperature dependence of the peak intensities:

$$I_{\text{red}} \propto \frac{I(\omega)}{n(\omega)+1}, \quad n(\omega) = \frac{1}{e^{\hbar\omega/kT}-1} \tag{2.35}$$

where $I(\omega)$ is the measured Stokes scattering intensity at temperature T in kelvin and k is the Boltzmann constant. The peak positions, widths, and intensities were determined by fitting the temperature-reduced spectra with Lorentzian functions.

2.4.3 Transmission electron microscopy

TEM was used as a method to probe the size and abundance of chemically 1:1 B-site ordered nanodomains. Similarly to the EPMA method (see Sec. 2.4.1), electrons are

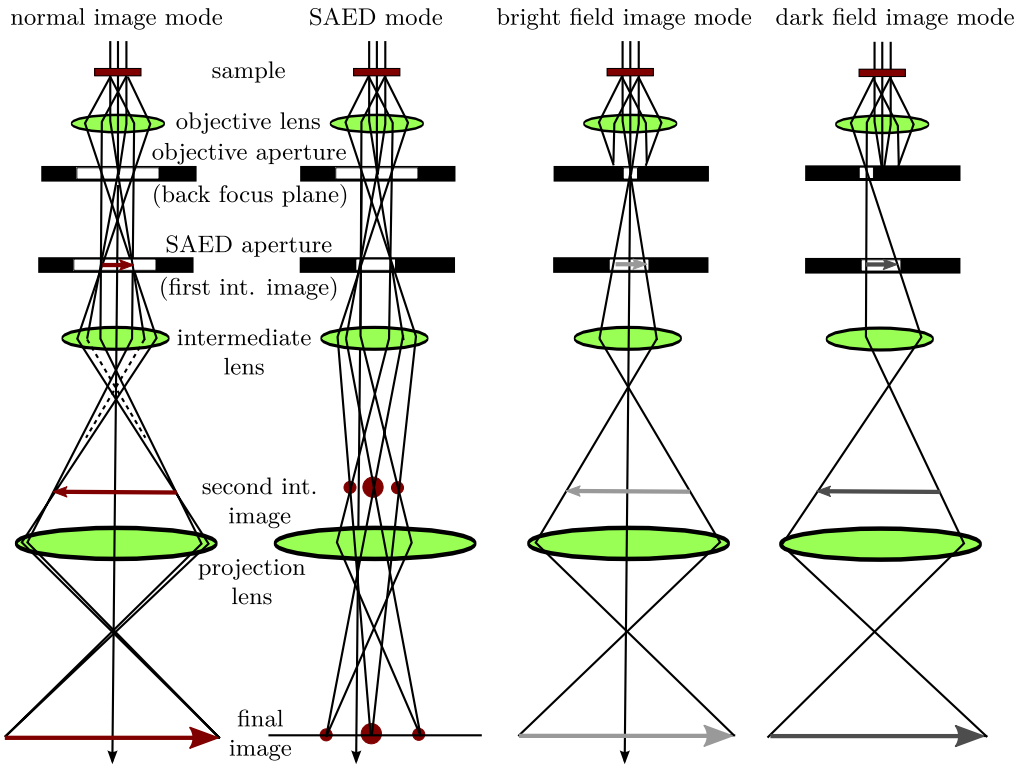

Figure 2.10: Schematic view of the beam path for TEM in different operation modes.

accelerated onto the sample, however, the electron energies are much higher, and hence the *de Brouglie* wavelength of the electron beam fulfils the requirements for diffraction from the periodic atomic array. Nevertheless, the sample has to be very thin in order to prevent absorption of the beam. A set of electromagnetic lenses and apertures schematically shown in Fig. 2.10 are placed below the sample in order to produce images or diffraction patterns. Beams with small diffraction angles are focussed in the back focal plane of the objective lens, creating an intermediate diffraction pattern. The diffracted beams are then recombined to form a first intermediate image in the image plane of the objective lens.

There are two basic operation modes in TEM. In the imaging mode, the intermediate lens is adjusted in such a manner that its object plane coincides with the image plane of the objective lens, projecting a second intermediate image which is then projected as the final image on the screen using the projector lens. In the diffraction pattern mode, the object plane of the intermediate lens coincides with the back focal plane of the objective lens, thus creating a second intermediate diffraction pattern which is then projected on the screen by the projector lens. In order to reduce intensity, the second aperture is closed, creating a virtual aperture on the sample, i.e. selecting an area of diffraction on the sample.

Once a SAED pattern is established, a diffraction spot can be chosen with the objective aperture, and switch back to imaging mode. This allows for taking bright field or dark field images, depending if the primary beam is in the aperture or only a diffraction spot (see Fig. 2.10).

In the phase-contrast imaging mode, which is more commonly named HRTEM, the objective aperture is completely opened or even removed in dedicated instruments in order to get contribution from as many as possible diffracted beams. The contrast in the image arises from the different phases of the diffracted beams, allowing for a spatial resolution of less than 1 Å. This can be achieved by defocusing the beam path in order to enhance the phase shift between diffracted beams.

The measurements in this work were carried out on a Philips CM20 super twin microscope operating at an acceleration voltage of 200 kV. The samples were {110}-oriented plates with a thickness of 10 μm, glued on a molybdenum grid and subsequently Ar^+ ion milled. Prior to the measurements, the sample plates were coated with a thin layer of carbon in order to prevent surface charging. SAED patterns were taken as well as HRTEM images.

3 Results

3.1 Chemical analysis

All compounds studied in this work were grown by the high-temperature solution growth method, resulting in optically homogeneous cubic-shaped single crystals with a mean edge length of 2–3 mm. In order to analyse the chemical composition and to verify the chemical homogeneity, EPMA has been applied, averaging over 50–100 spatial points. Subsequently, the degree of chemical B-site ordering S was determined by powder XRD at ambient conditions. S is given as the intensity ratio of the 111 and 200 reflection indexed according to space group $Fm\bar{3}m$ divided by the same ratio calculated for a perfectly B-site ordered structure:

$$S = \frac{[I(111)/I(200)_{\mathrm{meas}}]}{[I(111)/I(200)_{\mathrm{calc}}]} \tag{3.1}$$

The domain size of the ordered regions was determined from the width of the 111 peak after the Scherrer equation:

$$\tau = \frac{k\lambda}{\beta \cos\theta} \tag{3.2}$$

where τ is the mean size of the coherently diffracting domains, λ is the wavelength, β is the FWHM in radians, θ is the Bragg angle of the according reflection, and k is the shape

Table 3.1: Chemical composition obtained by EPMA and the degree of B-site ordering S as well as the B-site ordered domain size τ estimated from powder XRD data.

compound	chemical formula	S	τ (nm)
PST	$PbSc_{0.5}Ta_{0.5}O_3$	0.13	6.4
PST-Ba	$Pb_{0.78}Ba_{0.22}Sc_{0.5}Ta_{0.5}O_3$	0.11	32.8
PSN	$PbSc_{0.5}Nb_{0.5}O_3$	n.d.*	n.d.
PSN-Ba	$Pb_{0.93}Ba_{0.07}Sc_{0.5}Nb_{0.5}O_3$	n.d.	n.d.
PSN-Bi	$Pb_{0.98}Bi_{0.02}Sc_{0.51}Nb_{0.49}O_3$	n.d.	n.d.
PSN-La	$Pb_{0.77}La_{0.23}Sc_{0.62}Nb_{0.38}O_3$	n.d.	n.d.

*n.d., not detected

factor (see Langford and Wilson, 1978), which was set to 0.9 as an approximation for an unknown shape.

The chemical formulas for each compound are listed in Tab. 3.1.

3.2 Measurements as a function of temperature

3.2.1 Lead scandium tantalate, pure and Ba-doped

The relaxor ferroelectric PST is well-known compound, undergoing a phase transition from a relaxor to a normal ferroelectric state. The Curie temperature T_C varies in the range 250–300 K, depending on the degree of chemical 1:1 B-site ordering (Stenger and Burggraaf, 1980). The ferroelectric phase is rhombohedral, exhibiting the space group symmetry $R3$ (Woodward and Baba-Kishi, 2002). The recently synthesised PST-Ba shows a broad, frequency-dependent maximum of the dielectric permittivity near 200 K (Marinova et al., 2006), indicating a suppression of the low-temperature ferroelectric LRO.

Figure 3.1 shows representative (hkl) reciprocal-space layers determined from single-crystal synchrotron XRD data for PST and PST-Ba. At high temperature, near T_d, both compounds are cubic and can be indexed as $Fm\bar{3}m$. Both A- and B-site cations contribute to hkl diffraction peaks with $h, k, l = 2n$, where n is an integer. The A and B cations contribute additively to the Bragg reflections with $h + k + l = 4n$ and, hence, generate the stronger peaks in the ($hk0$) layer, whereas the two types of cations contribute in antiphase to the Bragg reflections with $h + k + l = 4n + 2$ and, consequently, give rise to the weaker peaks in the ($hk0$) layer. The chemical 1:1 B-site ordered domains (see Tab. 3.1) give rise to reflections of type hkl, all odd, which are visible in the ($hk1$) layer. The temperature evolution of the Bragg reflections and diffuse X-ray scattering reveals the relaxor-to-ferroelectric phase transition occurring upon cooling for PST. Upon cooling to 300 K, PST approaches its T_m at which PNR are abundant (see Sec. 1.3.2). Strong diffuse scattering streaks along $\langle 110 \rangle$ in the ($hk0$) layer develop, which is indicative of the existence of PNR, i.e. intermediate-range structural ordering associated with PNR (see Sec. 1.3.4). The direction of diffuse scattering shows that the atomic ferroic shifts correlate within $\{110\}$ planes of the real space. However, the real-space direction of atomic deviations from the crystallographic positions of the cubic structure cannot unambiguously be determined from the observed diffuse scattering. In particular, the preferred direction of Pb off-centre shifts is rather controversial and all the three pseudo-cubic directions, $\langle 100 \rangle$, $\langle 110 \rangle$, and $\langle 111 \rangle$, have been proposed on the basis of different experimental methods (see

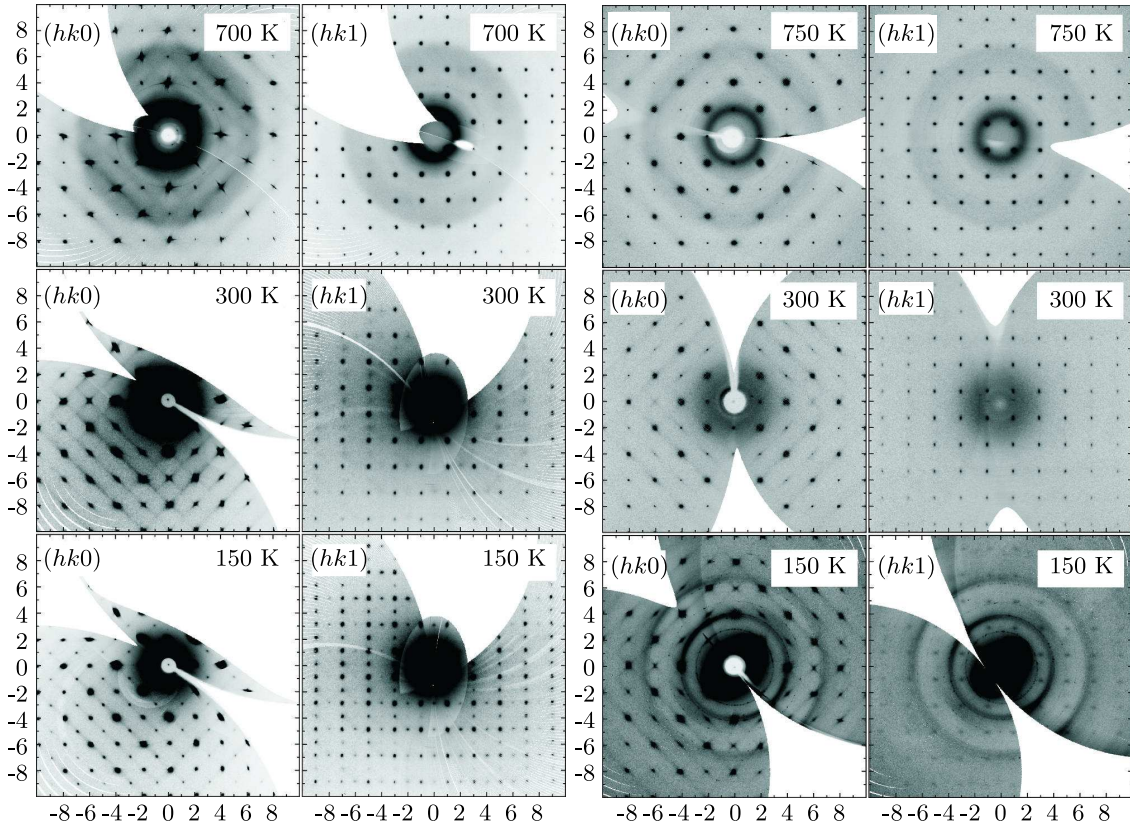

(a) PST. **(b)** PST-Ba.

Figure 3.1: Reciprocal space layers $(hk0)$ and $(hk1)$ at high, room, and low temperature for PST (a) and PST-Ba (b). All indices are given in space group $Fm\bar{3}m$. The round features are background contributions of the quartz capillary holding the sample.

Sec. 1.3.4). At $T = 150$ K, below T_{m}, the diffuse scattering for PST is strongly suppressed and additional Bragg reflections appear in both, $(hk0)$ and $(hk1)$ layers. The additional Bragg reflections seen at 150 K correspond to the crossings of the diffuse scattering streaks observed at 300 K, e.g. $1\bar{5}0$, and reveal the occurrence of ferroelectric LRO due to the enlarged correlation length between polar nanoclusters.

The temperature dependence of the (hkl) layers for PST-Ba is different from that of PST. As can be seen in Fig. 3.1b, upon cooling, the diffuse scattering gradually increases in intensity and it is strongest at low temperatures. As an estimate, the ratio $I_{\mathrm{DS}}/(I_{\mathrm{BR}} + I_{\mathrm{DS}})$ calculated for the $\bar{8}\bar{4}0$ reflection is approximately 0 at 750 K, $0.1{\cdot}10^{-3}$ at 300 K, and $1.5{\cdot}10^{-3}$ at 150 K. I_{BR} is the Bragg intensity determined from a fitted Voigt profile along the $[\bar{1}10]$ streak, while I_{DS} is the diffuse scattering determined as the difference between the average intensity of a parallel but off-peak profile and the baseline of the Bragg peak fitting. The absence of additional Bragg reflections at 150 K and the increase in diffuse-scattering

intensity confirm the suppression of ferroelectric LRO and the enhancement of a nonergodic, relaxor ferroelectric state as deduced from dielectric-permittivity experiments and polarised Raman spectroscopy (Marinova et al., 2006). A strong enhancement of the reflections stemming from (h00) planes, where $h = 6$, is observed upon cooling. At $T = 748$ K, neither the corresponding Bragg signal nor diffuse scattering is observed, at $T = 300$ K, only a weak diffuse scattering along the ⟨110⟩ directions exists, whereas at $T = 150$ K, a Bragg spot with the typical butterfly-shaped diffuse scattering (see Sec. 1.3.4) appears. A similar suppression is observed for signals stemming from (hh2) planes, where $h = 4$ (not shown). A similar tendency was found for other hk0 reflections with $h + k = 4n$, i.e. with nominally additive scattering contributions from both A- and B-site cations. In addition, the Bragg reflections in the (hk1) layer, which are related to chemically B-site ordered regions, become weaker and poorly resolved when the temperature decreases.

Further information on the preferred atomic arrangements can be gained from polarised Raman scattering. Figure 3.2 shows polarised Raman spectra of PST and PST-Ba at temperatures above T_{m}. For both PST and PST-Ba, the Z(XX)$\overline{\mathrm{Z}}$ Raman signals that appear near 53 and 77 cm^{-1} at room temperature are observed also at $T = 850$ K, which is above the typical values of T_{d}. Those signals arise from Pb-localised modes of ferroic species, which stem from the splitting of the Pb-localised F_{2g} mode of the cubic structure (see Appx. B for details), thus their contribution to the Z(XX)$\overline{\mathrm{Z}}$ Raman scattering is forbidden by the cubic symmetry. Therefore, the existence of anomalous Z(XX)$\overline{\mathrm{Z}}$ Raman peaks near 53 and 77 cm^{-1} undoubtedly reveals the presence of Pb off-centre shifts even at $T > T_{\mathrm{d}}$. These observations are in accordance with the results obtained from pair-distribution-function analysis (Egami, 2007). Both peaks near 53 and 77 cm^{-1} soften with the temperature decrease. The softening of both peaks indicates that the corresponding phonon modes are involved in the structural transformations occurring upon cooling. Another similarity between PST and PST-Ba is the suppression of the peak near 240 cm^{-1} at $T = 850$ K and its strong enhancement upon cooling. As explained in Appx. B, this peak arises from the infrared-active F_{1u} mode localised in the B-site cations and is also forbidden by cubic symmetry. Thus, the appearance of the infrared-active F_{1u} B-localised mode in the Raman spectra is indicative for off-centre shifts of B-site cations. Hence, the temperature evolution of Raman scattering at 240 cm^{-1} is related to the nucleation and development of PNR comprising B-cation off-centre shifts.

It has been demonstrated that the temperature dependence of the position, width, and intensity of the lowest-wavenumber unpolarised Raman signal reflects the development

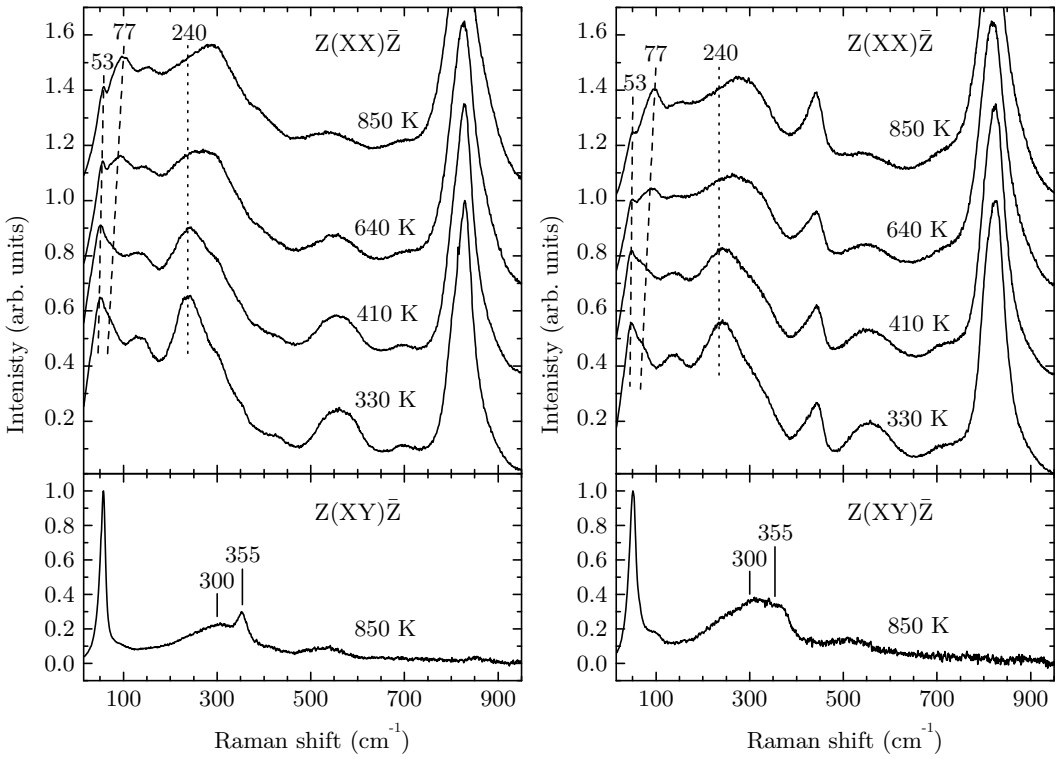

(a) PST. **(b)** PST-Ba.

Figure 3.2: Polarised Raman spectra of PST (a) and PST-Ba (b) collected at different temperatures above T_{m}∼280 K. The dashed lines in the parallel-polarised plots indicate the anomalous Raman scattering near 53 and 77 cm−1, which are related to the Pb-localised vibrations. The dotted lines trace the position of the anomalous Raman scattering near 240 cm−1 which is related to the B-cation-localised mode. The Raman scattering related to the Pb-O stretching mode near 300 and 355 cm−1 is marked in the 850 K cross-polarised spectrum.

of the ferroelectric state in PST (Bismayer et al., 1989). Hence, to gain deeper insights into structural phenomena in relaxors, the trends of the polarised Raman signals for the peak near 53 cm^{-1} are considered. Figures 3.3 shows the temperature dependence for PST and PST-Ba of the square wave number ω^2 of the allowed Z(XY)$\overline{\mathrm{Z}}$ and anomalous Z(XX)$\overline{\mathrm{Z}}$ Raman scattering near 53 cm^{-1}, which is generated from the Pb-localised phonon mode. When the temperature is changed from 850 K to T_{m}, the symmetry-allowed peak, which results from the F_{2g} mode in cubic symmetry, linearly decreases in wave number, while the temperature dependence of the anomalous Raman scattering is more complex. Initially, the anomalous signal follows the trend of the allowed signal, but near 700 K, it deviates from the linear dependence and starts to soften more strongly. The temperature deviation of $\omega^2(T)$ of the Z(XX)$\overline{\mathrm{Z}}$ peak from the $\omega^2(T)$ of the Z(XY)$\overline{\mathrm{Z}}$ peak is similar to the deviation of the temperature dependence of the refractive index from the expected linear

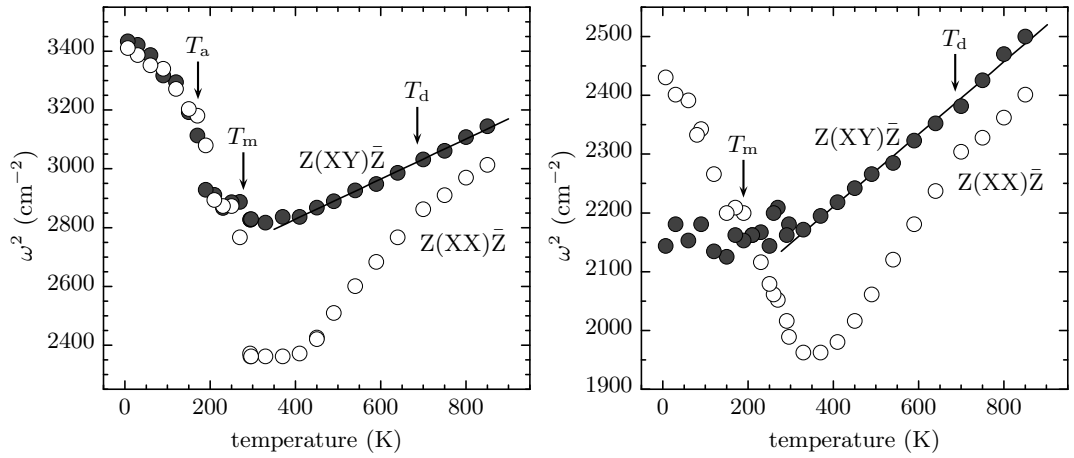

(a) PST. **(b)** PST-Ba.

Figure 3.3: Temperature dependence of the square wave number ω^2 of the allowed Z(XY)$\overline{\text{Z}}$ and anomalous Z(XX)$\overline{\text{Z}}$ Raman scattering near 53 cm^{-1} measured for PST (a) and PST-Ba (a). The lines represent linear fits of $\omega^2(T)$ at $T > 400$ K for the allowed Raman scattering (F_{2g} mode in $Fm\bar{3}m$).

trend typical of paraelectrics (Burns and Dacol, 1983), thus it corresponds to T_d. For PST, near 420 K, the anomalous peak stops softening and between 420 and 290 K, $\omega^2(T)$ has a plateau-like shape, indicating additional structural transformation processes between T_d and T_m. Below T_m, the temperature dependence of the peak positions observed in Z(XX)$\overline{\text{Z}}$ and Z(XY)$\overline{\text{Z}}$ spectra becomes the same, as ferroelectric LRO domains of rhombohedral symmetry are formed. Hence, the peaks originate from rhombohedral phonon modes and can no longer be considered in terms of *anomalous* and *allowed* signals coming from the cubic F_{2g} mode. Another change in the slope in $\omega^2(T)$ is observed near $T_a = 190$ K due to lowering of the rotational local symmetry as revealed by the additional splitting of the Raman peaks (Mihailova et al., 2005). For PST-Ba, the anomalous signal near 53 cm^{-1} exhibits a broad minimum near 350 K instead of a plateau-like $\omega^2(T)$ dependence as in the case of PST, which implies that coupling processes within the system of off-centred Pb atoms are weaker as compared to those in PST. Below T_m, the anomalous and the allowed scattering have different temperature dependencies in contrast to PST, which mirrors the absence of ferroelectric LRO domains. Below 350 K, the allowed Z(XY)$\overline{\text{Z}}$ signal shows no hardening on cooling, which also indicates the absence of transition to normal ferroelectric state. The slight kink in $\omega^2(T)$ of the anomalous Pb-localised signal marks the temperature of the dielectric maximum T_m (see Fig. 3.3b).

As the off-centre shifts of B-site cations play an important role in perovskite-type ferroelectrics (see Sec. 1.2), the behaviour of the anomalous Raman peak at 240 cm^{-1}

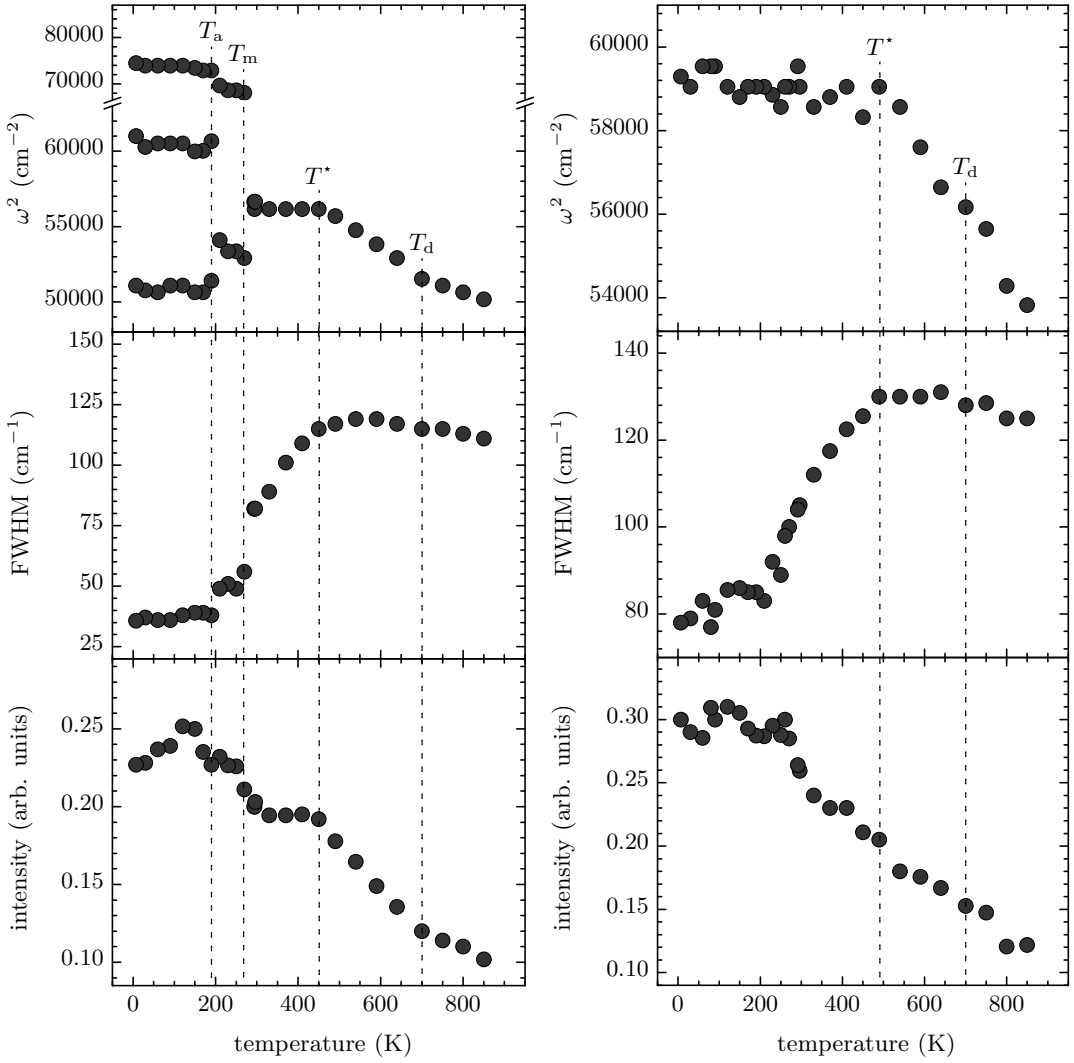

(a) PST. **(b)** PST-Ba.

Figure 3.4: Temperature dependence of the square wave number, FWHM for the most intense component, and total intensity of the Raman scattering near 240 cm^{-1} measured in Z(XX)$\overline{\text{Z}}$ scattering geometry for PST (a) and PST-Ba (a).

(see Fig. 3.4), which arises from off-shifted B-site cations, helps to better understand the formation of PNR in relaxors. Figure 3.4 shows the temperature dependence of ω^2, FWHM, and the total intensity I of the Raman scattering near 240 cm^{-1} for PST and PST-Ba. For PST, near 700 K, an increase in the slope of $\omega^2(T)$ and $I(T)$ is observed, corresponding to T_d similarly to the mode near 53 cm^{-1}. Below 450 K, no further change in wave number and intensity takes place, however, the FWHM decreases strongly between $T^\star = 450$ K and T_m. Below T_m, the peak first splits in two and then, at T_a, in three components,

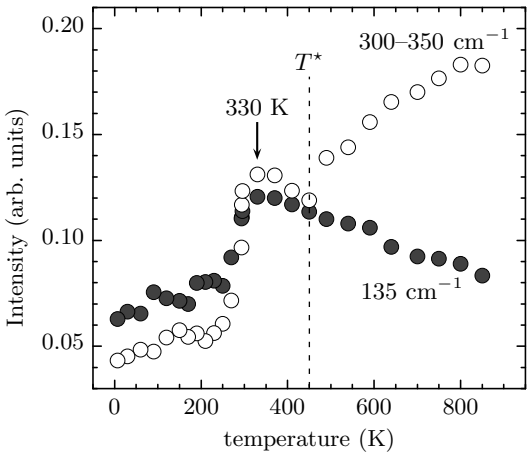

Figure 3.5: Temperature dependence of the intensities of the Raman scattering near 135 cm^{-1} (filled circles) and 300–350 cm^{-1} (open circles), which is related to the Pb-BO_3 translational mode and Pb-O stretching mode, respectively, measured for PST in Z(XX)$\overline{\text{Z}}$ scattering geometry.

clearly due to the formation of the ferroelectric LRO state. The peak width at $T < T_\text{m}$ is plotted for the most intense component in Fig. 3.4a. For PST-Ba, no peak splitting at low temperatures is observed and no change in slope occurs near 700 K. However, below 490 K, a decrease of the FWHM takes place while the wave number remains constant. In contrast to PST, however, the intensity continues to increase.

A challenging problem is to distinguish phonon modes involved in the inter-cluster coupling from the rest of the anomalous phonons. Such modes should substantially comprise vibrations of atoms at the interface between the polar spatial regions and the paraelectric matrix. For relaxors that exhibit ferroelectric LRO, the number of interface atoms should initially increase because of the enlargement of the polar nanoclusters and then it should decrease due to merging of clusters in domains. Hence, the intensity of such modes should have a maximum within the temperature range of inter-cluster coupling. PST undergoes a phase transition to the normal ferroelectric state, which makes this compound a very suitable model system. The analysis of the temperature evolution of Raman scattering for PST reveals that two modes indeed show such a feature (see Fig. 3.5). The integrated intensity of the Raman scattering near 135 cm^{-1} (Pb-BO_3) and 300-355 cm^{-1} (Pb-O) show a peak near 330 K. For the latter phonon mode, PST exhibits a higher intensity ratio ρ (Eq. B.1) (see the bottom plots in Fig. 3.2) than PST-Ba, revealing a larger correlation length of coherent structural distortions in the Pb-O system (see Appx. B for details).

To check whether the structural changes taking place near T* affect the average structure, powder XRD analysis at different temperatures was performed. Figure 3.6 show the temperature evolution of the lattice parameters of PST and PST-Ba, derived from Rietveld refinements to the powder data. The existence of a phase transition in the vicinity of $T^\star$ K

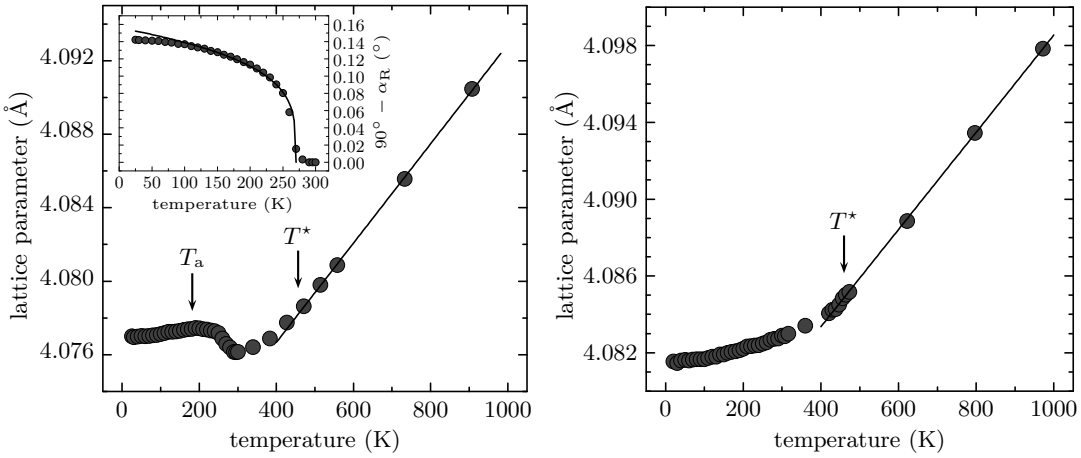

(a) PST. **(b)** PST-Ba.

Figure 3.6: Temperature evolution of the lattice parameters for PST (a) and PST-Ba (b). The inset in (a) show the deviation of the rhombohedral angle α_R from 90°. The line represents a power-function fit with $90 - \alpha_R = 0.0385(270 - T)^{1/4}$.

is revealed. For PST below 450 K and for PST-Ba below 490 K, the pseudo-cubic unit-cell parameter clearly deviates from the linear dependence characteristic of high temperatures, thus revealing the occurrence of structural transformation. For PST, the low-temperature data are in good accordance with the structure refinement based on high-resolution neutron diffraction data (Woodward and Baba-Kishi, 2002). A paraelectric-to-ferroelectric phase transition from the cubic $Fm\bar{3}m$ to the rhombohedral $R3$ structure occurs at 280 K. Since $R3$ is a polar crystal class, the deviation of the unit-cell angle α_R (rhombohedral setting) from 90° is related to spontaneous polarisation and, hence, $90° - \alpha_R$ can be used as an order parameter. It can be seen in the inset of Fig. 3.6a, $90° - \alpha_R$ follows the $A(T_C - T)^{1/4}$ dependence, as found by Woodward and Baba-Kishi (2002), who suggested that this result indicates a weak first-order phase transition approaching a tricritical point. It is worth noting that the rhombohedral unit-cell parameter a has a maximum at $T = 190$ K, which corresponds well to the temperature T_a, determined from the temperature dependence of the Raman spectra. The comparison between the temperature evolution of the unit-cell parameters and Raman scattering reveals that just below T_m, the parameter $90° - \alpha_R$ becomes nonzero, thus indicating the occurrence of cubic-to-rhombohedral transition. Accordingly, below T_m, the Raman peaks originating from cubic F modes split into two components, corresponding to rhombohedral A and E modes. Between T_m and T_a, the unit-cell parameter a increases with the temperature decrease, whereas below T_a, $a(T)$ follows the ordinary trend. At the same time, below T_a, the Raman peaks originating from

the cubic F modes further split to three components which evidences additional lowering of the local symmetry. Indeed, Woodward and Baba-Kishi (2002) refined the average structure of PST at 4.2 K by considering the coexistence of cation-oxygen polyhedra that have C_3 and C_1 symmetries. Therefore, the complementary XRD and Raman data presented here indicate that the development of ferroelectric LRO in PST may be considered as a two-step process: First, rhombohedral distortion of the unit cell just below T_m, and second, atomic rearrangements that lower the local symmetry below T_a. The temperature dependence of the pseudo-cubic unit-cell parameter a of PST-Ba is shown in Fig. 3.6b. The high-resolution powder XRD data again confirm the absence of a ferroelectric phase transition below T_m. As in the case of PST, near $T^\star$, a deviation of $a(T)$ from the linear trend is observed.

3.2.2 Lead scandium niobate, pure, Ba-, Bi-, and La-doped

Disordered PSN is another well-known relaxor compound which undergoes a relaxor-to-ferroelectric phase transition near 378 K from $Pm\bar{3}m$ to $R3m$ (Perrin et al., 2000). At 100 kHz the T_m for PSN-Ba and PSN-Bi is near 270 and 330 K, respectively (Petrova, unpublished).

First, PSN-Ba and PSN-Bi, both with relatively low degree of doping, are compared in order to analyse the role of LPE for the formation of ferroelectric LRO at low temperatures. In order to substantiate that analysis, the XRD results on the heavily doped PSN-La are presented afterwards.

Figure 3.7 shows $hk0$ and $hk1$ reciprocal lattice sections of PSN, PSN-Ba, and PSN-Bi at three different temperatures: well above T_m (T = 700 K), near T_m (T = 300 K), and well below T_m (T = 150 K). The indexation is given in a face-centred cubic $Fm\bar{3}m$ space group symmetry. All the three compounds show no or very weak diffuse scattering at 700 K and develop diffuse scattering along $\langle 110 \rangle$ in the $hk0$ layers at 300 K, which is stronger for the doped compounds. For PSN, well below $\mathrm{T_m}$, additional Bragg reflections appear at the crossings of the diffuse streaks observed near $\mathrm{T_m}$. Such Bragg reflections indicate a lowering of the cubic face-centred symmetry and therefore reveal the development of ferroelectric LRO, i.e. the occurrence of a phase transition to a normal ferroelectric state. The incorporation of Ba^{2+}-cations suppresses this phase transition and enhances the relaxor state, as revealed by the increase in the diffuse scattering intensity at low temperature. The same effect of Ba-doping was observed for PST as a host matrix (see Sec. 3.2.1. However, the substitution of Bi^{3+} for Pb^{2+} leads to a more complex, intermediate structural state.

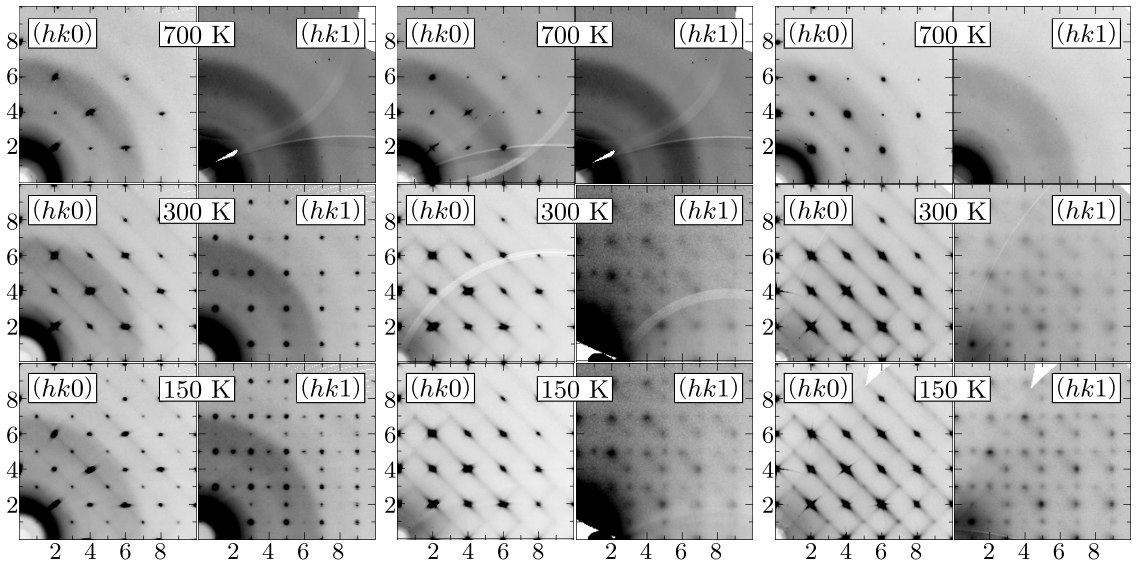

(a) PSN. **(b)** PSN-Ba. **(c)** PSN-Bi.

Figure 3.7: The $(hk0)$ and $(hk1)$ layers of the reciprocal space at high, room, and low temperature, reconstructed from synchrotron data for PSN (a), PSN-Ba (b), and PSN-Bi (c). The Miller indices are given in a cubic double-perovskite $Fm\bar{3}m$ unit cell. The powder rings are artificial contributions from a quartz capillary used for some of the measurements. The ellipses mark examples of diffuse scattering between pairs of adjacent points with the indices $h\,k\,1$ and $h+i\,k+j\,1$ with $h=2n$, $k=n$, and $i=+1$ for h, $i=-1$ for $\bar{h}$, $j=+1$ for $\bar{k}$, and $j=-1$ for k.

The diffuse scattering is still well pronounced but resolved Bragg reflections appear at the crossings of the diffuse scattering streaks (see Fig. 3.7c and 3.8a for an enlarged segment). This indicates coexistence of ferroelectric *normal* domains, large enough to generate Bragg reflections, and ferroelectric nanodomains of a size still below the length-scale sensitivity of XRD. It is worth noting that the development of ferroelectric LRO was not detected by high-resolution powder XRD in both PSN and PSN-Bi, which indicates a subtle rhombohedral distortion of the average structure and/or a tiny portion of FE-LRO domains inside a pseudo-cubic matrix.

At high temperature Bragg reflections arising from chemical B-site ordering with hkl, all odd, are observed for PSN, whereas for PSN-Ba and PSN-Bi they can hardly be resolved from the background. One should underline that the powder XRD patterns of all the three compounds do not show any superlattice reflections related to B-site ordering, which points to a very low degree of B-site ordering in PSN. On cooling no change in the B-site ordering takes place and, therefore, the observed additional features in the $hk1$ layers at low temperature are related to the enhancement of coherent ferroic displacements of atoms from their cubic positions. The additional Bragg reflections detected for PSN at 150 K

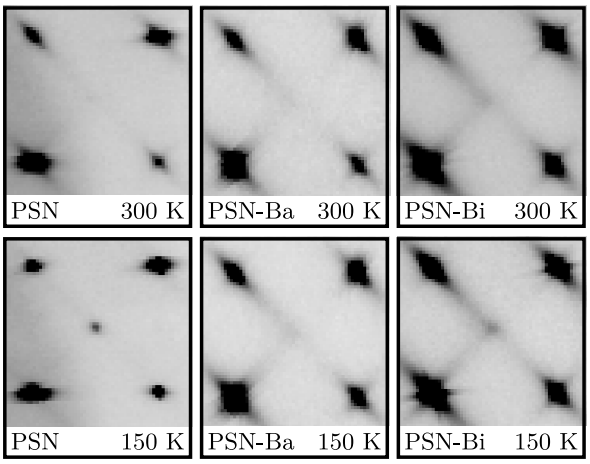

(a) ($hk0$) layer.

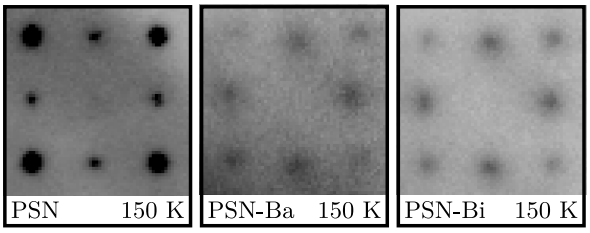

(b) ($hk1$) layer.

Figure 3.8: Enlarged segments of the ($hk0$) and ($hk1$) layers (see Fig. 3.7) at 300 K and 150 K for PSN, PSN-Ba, and PSN-Bi. The indices of the four strong Bragg reflections in (a) are 640, 840, 620, and 820, respectively. The corner peaks in (b) have the indices 531, 551, 331, and 531, respectively.

reveal the occurrence of ferroelectric LRO, while the corresponding diffuse spots observed for the doped samples are intersections of the diffuse scattering observed in the $hk0$ layers Welberry et al. (2005); Welberry and Goossens (2006). The relative intensity between peaks with hkl, all odd, and hkl, two odd, one even, is different for PSN as compared to PSN-Ba and PSN-Bi, due to the presence of detectable B-site ordered regions in the undoped sample. According to Monte Carlo simulations based on correlated atomic shifts within {110} planes of the real space Welberry et al. (2005), the $hk1$ diffuse spots with h and k odd arise from local chemical ordering on the B-site. Those spots are not resolved in the reciprocal ($hk1$) layers of the doped samples measured at 700 K, due to the high background of the sample-containing glass capillary. It is worth mentioning the noticeable diffuse scattering streaks observed in the reciprocal $hk1$ layers of PSN-Ba and PSN-Bi at 300 and 150 K between pairs of adjacent points with the indices $h\,k\,1$ and $h+i\,k+j\,1$ with $h = 2n$, $k = n$, and $i = +1$ for h, $i = -1$ for $\bar{h}$, $j = +1$ for $\bar{k}$, and $j = -1$ for k (see Figs. 3.7b and 3.7c). These additional features may result from diffuse scattering along other reciprocal lattice directions, which in turn would indicate coherence of ferroic atomic shifts within the corresponding crystallographic planes in the real space. To clarify the origin of

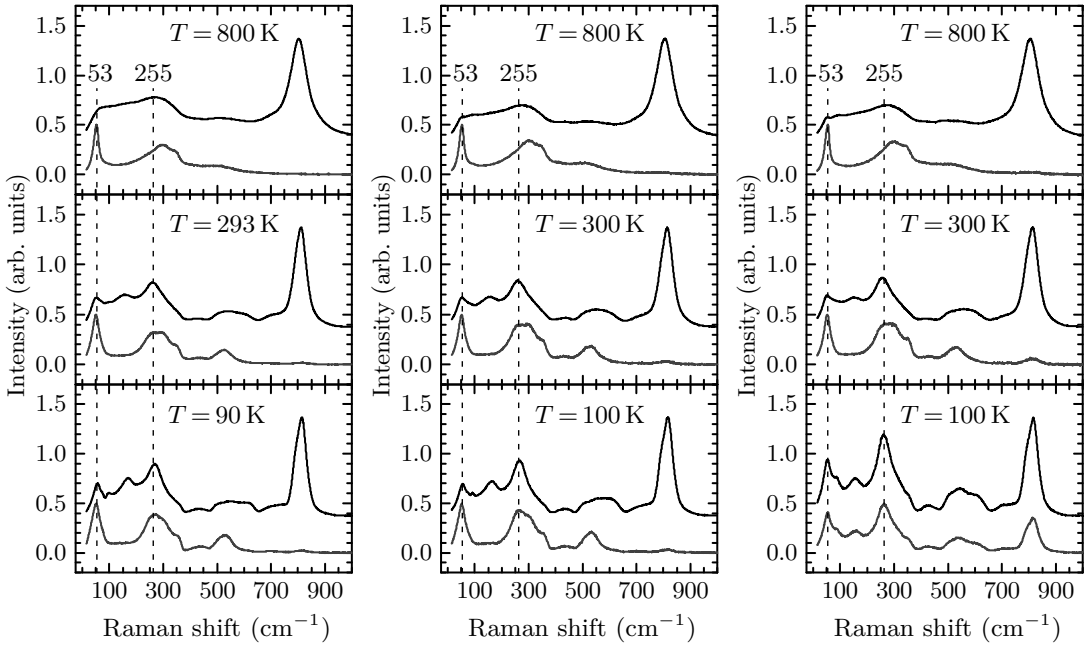

(a) PSN. **(b)** PSN-Ba. **(c)** PSN-Bi.

Figure 3.9: Raman scattering of PSN (a), PSN-Ba (b), and PSN-Bi (c) collected at high, room, and low temperatures. The solid black and gray lines represent Z(XX)$\overline{\text{Z}}$ and Z(XY)$\overline{\text{Z}}$ polarised spectra, respectively. The dashed lines mark the Raman scattering near 53 cm^{-1}, which is related to the Pb-localised vibrations, and near 255 cm^{-1}, which is related to the B-cation-localised mode.

the observed diffuse features model calculations are required, which however is beyond the scope of this work.

In order to gain further insights into the structural changes on a local scale polarised Raman spectroscopy was applied. Figure 3.9 shows Z(XX)$\overline{\text{Z}}$ and Z(XY)$\overline{\text{Z}}$ Raman spectra of PSN, PSN-Ba, and PSN-Bi at representative temperatures well above, near and well below

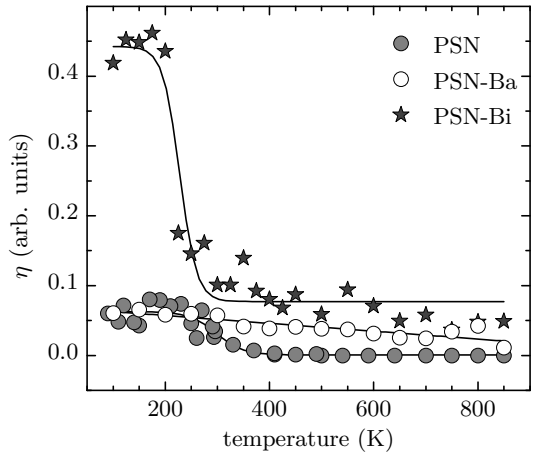

Figure 3.10: Temperature dependence of the depolarisation ratio η (Eq. B.2) for PSN, PSN-Ba, and PSN-Bi. The solid lines are guides for the eye.

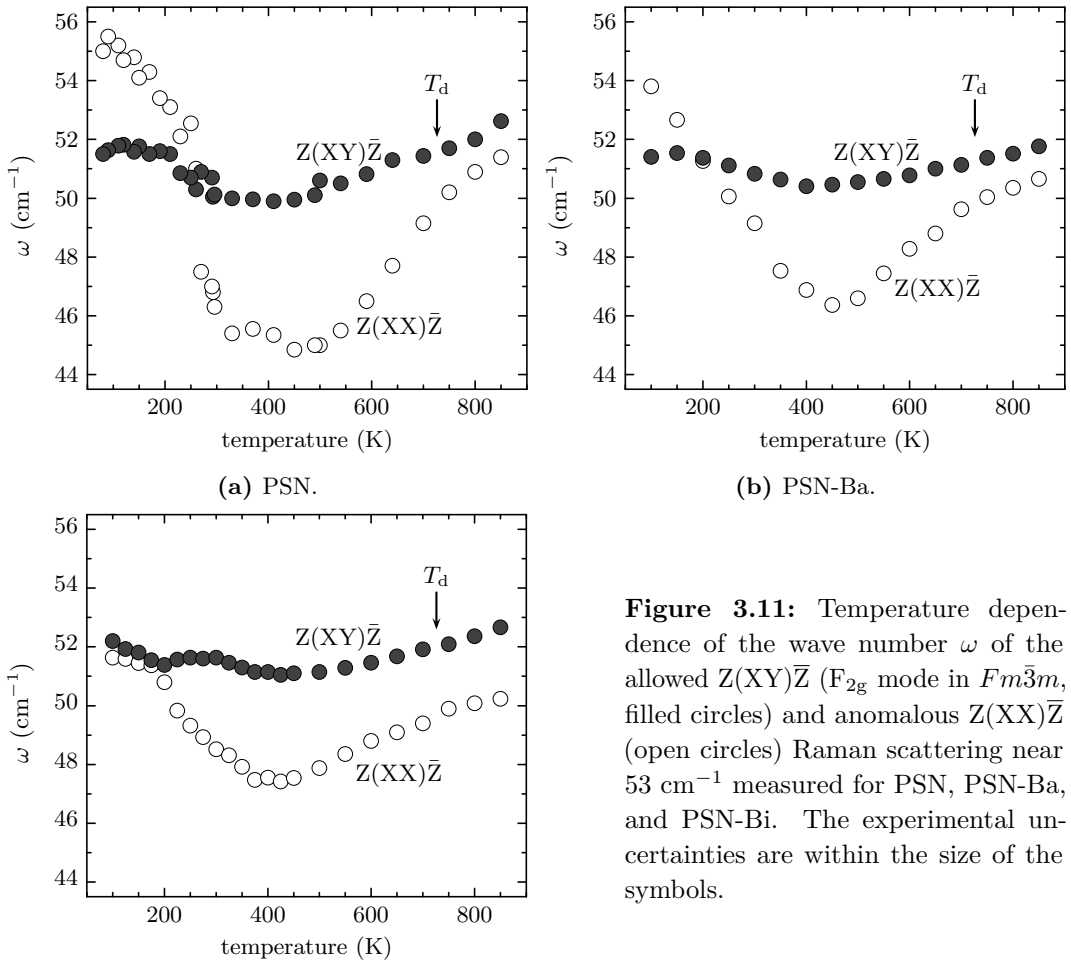

(a) PSN.

(b) PSN-Ba.

(c) PSN-Bi.

Figure 3.11: Temperature dependence of the wave number ω of the allowed Z(XY)$\overline{\text{Z}}$ (F_{2g} mode in $Fm\bar{3}m$, filled circles) and anomalous Z(XX)$\overline{\text{Z}}$ (open circles) Raman scattering near 53 cm^{-1} measured for PSN, PSN-Ba, and PSN-Bi. The experimental uncertainties are within the size of the symbols.

T_{m}. For all three compounds the anomalous Raman peaks arising from the Pb-localised (53 cm^{-1}) and B-cation-localised (255 cm^{-1}) modes are strongly enhanced upon cooling, which points to an enlarged number of off-centred Pb and B-site cations associated with the PNR.

Figure 3.10 shows the temperature evolution of the depolarisation η of the Raman spectra for PSN, PSN-Ba, and PSN-Bi. The latter compound shows a strong increase of the depolarisation below 250 K, whereas PSN-Ba shows a linear, almost temperature-independent $\eta(T)$. For PSN, a slight increase of $\eta(T)$ occurs below 300 K.

Figure 3.11 shows the $\omega(T)$ dependence of the Raman scattering near 53 cm^{-1} PSN, PSN-Ba, and PSN-Bi. All three compounds exhibit similar behaviour at high temperatures: the allowed Z(XY)$\overline{\text{Z}}$ peak shows a weak, linear softening, whereas the anomalous Z(XX)$\overline{\text{Z}}$ peak develops a significantly stronger softening below ∼750 K, corresponding to T_{d}. For

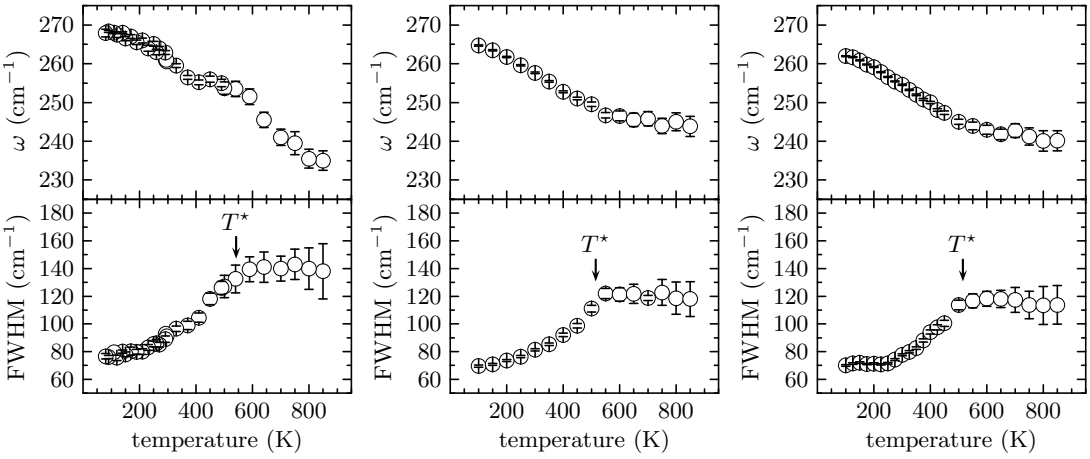

(a) PSN. **(b)** PSN-Ba. **(c)** PSN-Bi.

Figure 3.12: Temperature dependence of the wave number ω and the FWHM of the Raman scattering near 255 cm^{-1} measured for PSN, PSN-Ba, and PSN-Bi in Z(XX)$\overline{\text{Z}}$ scattering geometry.

PSN, the anomalous peak stops softening near 500 K and the $\omega(T)$ dependence develops a plateau-like shape in the range 500–300 K. No such plateau is observed for PST-Ba, whereas PSN-Bi shows a more narrow plateau than PSN. At low temperatures, the allowed and anomalous signal show different $\omega(T)$ dependencies for PSN and PST-Ba, whereas for PSN-Bi, they become the same.

Figure 3.12 shows the $\omega(T)$ and FWHM(T) dependencies of the anomalous Raman peak near 255 cm^{-1}, which is related to B-cation off-centre shifts, for PSN, PSN-Ba, and PSN-Bi. A common feature of all compounds is the drop of the FWHM near 550 K. For PSN-Ba the FWHM decreases steadily to the lowest temperature measured, whereas for PSN-Bi it becomes almost constant below 250 K. At low temperatures $\omega(T)$ continues to increase without reaching saturation.

To follow structural changes in the average structure, high-resolution powder XRD was applied. Although single-crystal XRD with synchrotron radiation revealed additional Bragg reflections for PSN and PSN-Bi (Fig. 3.8a), no line splitting was observed in the powder XRD patterns of all the three compounds because of the intrinsic limitation of the method. Hence, the temperature dependence of the pseudo-cubic unit cell a (see Fig. 3.13) was considered. As can be seen in Fig. 3.13, a slight change in the linear trend of $a(T)$ in the vicinity of T_d is also observed for PSN, PSN-Ba, and PSN-Bi. Apparent nonlinearity of $a(T)$ occurs below $T^\star$, similarly to PST and PST-Ba (see Fig. 3.6). The pseudo-cubic unit cell parameter of PSN shows a maximum near $T_\text{a} = 400$ K, close to the phase transition

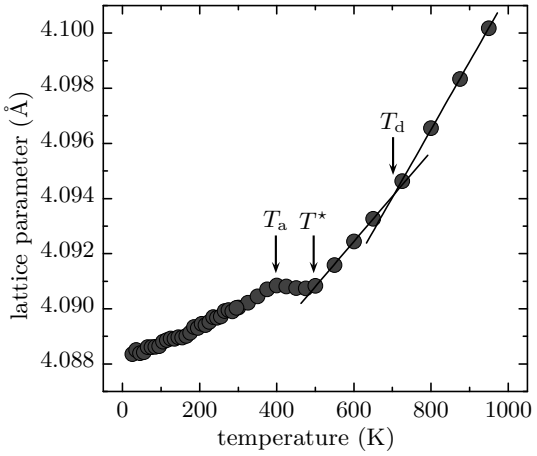

(a) PSN.

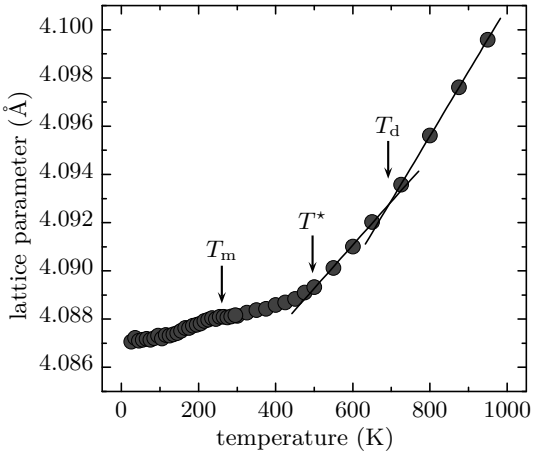

(b) PSN-Ba.

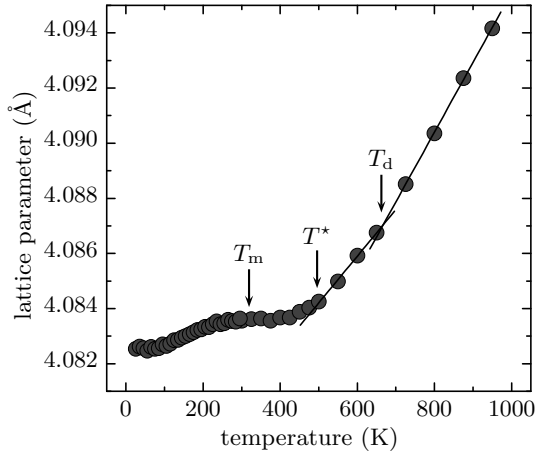

(c) PSN-Bi.

Figure 3.13: Temperature evolution of the lattice parameters for PSN (a), PSN-Ba (b), and PSN-Bi (c). The lines represent linear fits in the ranges $T^\star < T < T_d$ and $T_d < T < T_{max}$. T_a in (a) indicates the maximum of the pseudo-cubic unit-cell parameter of PSN, which coincides with the cubic-to-rhombohedral phase transition reported by Perrin et al. (2000).

reported by Perrin et al. (2000). A maximum of $a(T)$ below $T^\star$ is observed also for the doped samples and it coincides well with T_m.

Figure 3.14 shows the reciprocal lattice section $(hk0)$ and $(hk1)$ for PSN-La reconstructed from synchrotron data at 300 K and 150 K. At room temperature, PSN-La exhibits diffuse scattering streaks in the $(hk0)$ layer along the $\langle 110 \rangle$ directions. These streaks are clearly enhance upon cooling to 150 K, thus no ferroelectric LRO is developed at low temperatures. The $(hk1)$ layer shows reflections with hkl, all odd, which are sharper than the ones observed for PSN (see Fig. 3.7a). As an estimate, a box profile of the 531 reflection, where the x-axis represents the horizontal distance through the selection and the y-axis the vertically averaged pixel intensity, was fitted with an pseudo-Voigt profile for PSN and PSN-La. The fits yield a FWHM in pixels of 48.9 for PSN and 34.3 for PSN-La. This is

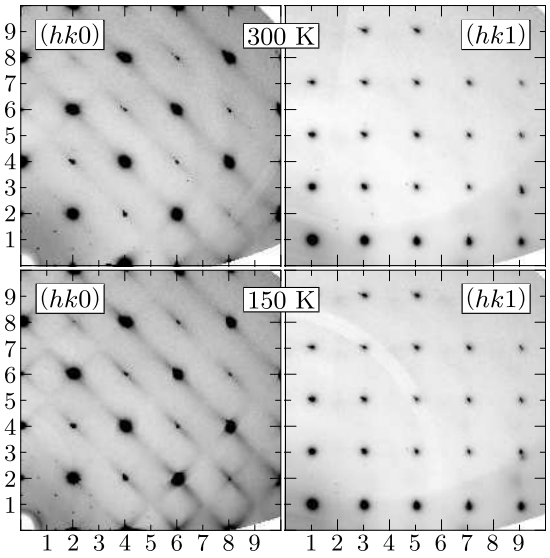

Figure 3.14: The $(hk0)$ and $(hk1)$ layers of the reciprocal space at 300 K and 150 K, reconstructed from synchrotron data for PSN-La. The Miller indices are given in a cubic double-perovskite $Fm\bar{3}m$ unit cell.

consistent with the fact that these reflections of PSN-La originate from anti-phase tilted BO_6 octahedra rather than from chemical B-site ordered domains.

3.3 High-pressure diffraction analysis

3.3.1 Lead scandium tantalate, pure and Ba-doped

At room pressure and temperature PST and PST-Ba exhibit a pseudo-cubic structure consisting of a paraelectric perovskite-type matrix in which PNR are dispersed, thus both the compounds show strong diffuse scattering streaks along the $\langle 110 \rangle^*$ direction (see Fig. 3.1). The average structure exhibits $Fm\bar{3}m$ symmetry. In this symmetry, Bragg reflections indexed with hkl all even (eee-reflections) arise from the primitive-cubic perovskite-type structure, whereas Bragg reflections with hkl all odd (ooo-reflections) arise solely from B-site 1:1 chemically ordered regions and reflect the average chemical B-site cation order within the sample. Both compounds have a low degree of B-site order, whereas PST-Ba has larger B-site ordered domains (33 nm) compared to PST (6 nm, see Tab. 3.1). Structure refinements in $Fm\bar{3}m$ to low-pressure synchrotron single-crystal XRD data also reveal a smaller B-site cation order parameter for PST ($Q_{od} = |\mathrm{SOF(Ta)} - \mathrm{SOF(Sc)}|/[\mathrm{SOF(Ta)} + \mathrm{SOF(Sc)}] = 0.08(2)$ at 0.5 GPa) than for PST-Ba ($Q_{od} = 0.23(2)$ at ambient pressure Marinova et al. (2006)).

In-house single-crystal XRD measurements showed that at ambient and low pressures the diffraction maxima with hkl all even (indexed in $Fm\bar{3}m$) are sharp and the measured unit-cell parameters are cubic (Mihailova et al., 2008a). At pressures above 1.9 GPa the diffraction maxima show broadening (see reflection 022 as representative example in Fig. 3.15d), which was completely reversible on pressure release. The broadening cannot represent a decrease in domain/crystallite size because the corresponding reflections arise from the average cubic structure alone. At the same pressure the evolution of the unit-cell volume V of the material shows a distinct change (Fig. 3.15a). This change in elasticity is clearer when the data are transformed to an f-F plot (Fig. 3.15b, see Sec. 2.1.4 for details). The low-pressure data indicate that the bulk modulus K_T of the material decreases with increasing pressure. At $P > 2$ GPa the slope of the f-F plot is positive, and a direct fit of the P-V data indicates that $dK_T/dP = 13 \pm 4$. There is no detectable discontinuity in the unit-cell volume (Fig. 3.15a), but there is in the bulk modulus (Fig. 3.15c). These observations are all characteristic of a thermodynamically second-order structural phase transition involving elastic softening in both phases as they approach the phase transition (Carpenter and Salje, 1998).

The pressure evolution of the normalised unit-cell volume of PST-Ba shows no exceptional behaviour in the pressure range of the measurements (see Fig. 3.16a). All experimental

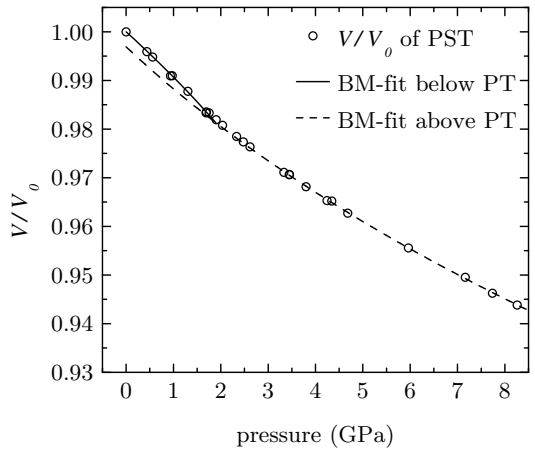

(a) Pressure dependence of the normalised unit-cell volume.

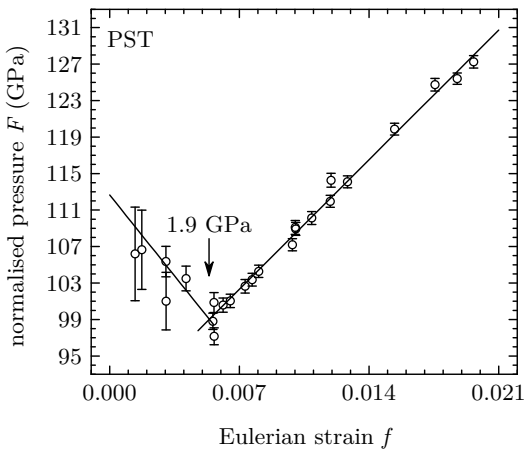

(b) Eulerian strain against normalised pressure.

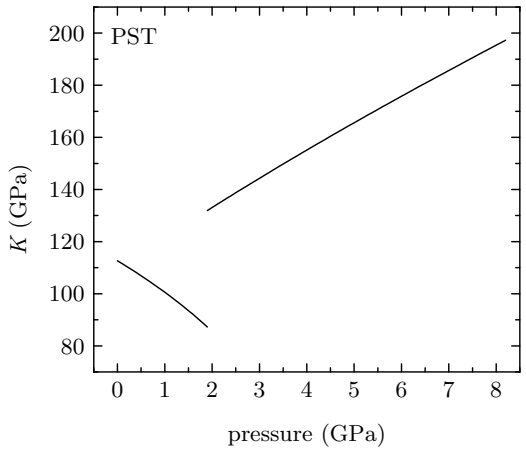

(c) Pressure dependence of the bulk modulus obtained from fitted EoS.

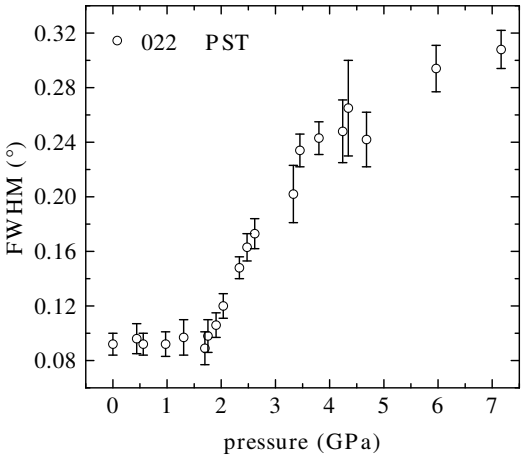

(d) Pressure dependence of the FWHM of the 022 reflection.

Figure 3.15: Volume compressibility of PST obtained by XRD measurements (Mihailova et al., 2008a).

points between ambient pressure and 10 GPa could be fit with a third-order BM-EoS (see Sec. 2.1.4 for details) leading to the following values of the initial unit-cell volume, the bulk modulus and its first derivative over pressure, respectively: $V_0 = 544.52 \pm 0.09$ Å^3, $K_0 = 110.2 \pm 1.9$ GPa, and $K_0' = 9.9 \pm 0.6$. The f-F diagram (Fig. 3.16b) indicates however that the compression behaviour of the average unit cell does not follow an ordinary EoS. In PST the existence of a second-order phase transition corresponds to a minimum of $F(f)$, with negative and positive values of dF/df below and above the critical pressure, respectively (see Fig. 3.15b). The f-F plot of PST-Ba and pure PST are compared in Fig. 3.16d. As can be seen, a negative slope below 2.0 GPa and a positive slope above 3.9

GPa are also observed for PST-Ba. However, contrary to PST, the minimum of $F(f)$ for PST-Ba is not well defined and has a plateau-like shape between 2 and 3.9 GPa. The use of two different sets of EoS parameters to fit the unit-cell volume data of PST below and above the critical pressure $P_c = 1.9$ GPa allowed the discontinuity in the bulk modulus at P_c to be determined (see Fig. 3.15c). Likewise, the low-pressure bulk modulus of PST-Ba was calculated by fitting only the experimental points corresponding to the negative slope of the f-F plot, i.e. below 2.0 GPa, while the high-pressure bulk modulus was obtained from the experimental points corresponding to the positive $F(f)$ slope, i.e. above 3.9 GPa (see Fig. 3.16c). The results show that the first derivative of the low-pressure bulk modulus dK/dP is negative, which reveals structure softening, whereas the structure stiffens above 3.9 GPa with $dK/dP > 4$. In the pressure range of the plateau-like minimum between 2 and 4 GPa $dK/dP = 4$, which is consistent with a second-order truncation of the BM-EoS. Thus, the $F(f)$ diagram and the bulk modulus changes in PST-Ba reveal a broad, diffuse phase transition over a pressure range of 2–4 GPa, without exhibiting a distinctive critical pressure point. Therefore, the incorporation of Ba into PST smears out the pressure-induced phase transition.

Figure 3.17 shows the pressure evolution of the diffuse scattering around the representative reflections $0\bar{6}0$ and $\bar{4}60$ for PST and PST-Ba. For PST the diffuse scattering is very strong at 0.5 GPa, but is significantly suppressed when approaching the phase transition at $P_c = 1.9$ GPa. At $P > P_c$ the streaks still persist in weakened form, suggesting that correlated atomic displacements remain in the sample at least up to 2.8 GPa. Similar to pure PST, pressure suppresses the diffuse scattering in PST-Ba (Fig. 3.17b). It is already strongly suppressed at 2.7 GPa, which is in the plateau-like minimum of $F(f)$ shown in Fig. 3.16b, confirming that transformation processes occur above 2 GPa, as deduced from the EoS.

Structural refinements and symmetry analyses based only on XRD data are restricted by the weak scattering of the oxygen atoms compared to the cations, and very significant absorption and extinction issues. Therefore, in order to completely determine the high-pressure structural state of Pb-based relaxors, high-pressure neutron powder diffraction was applied to PST and PST-Ba. Figure 3.18a shows sections of the powder patterns for both the compounds at low and high pressure. The diffuse scattering around eee-reflections is not observable in the neutron powder diffraction patterns at any pressure. The ooo-reflections can not be observed up to 1.09(2) GPa for PST and up to 3.52(3) GPa for PST-Ba. The absence of the ooo-reflections can be attributed to the low degree of B-site cation order and

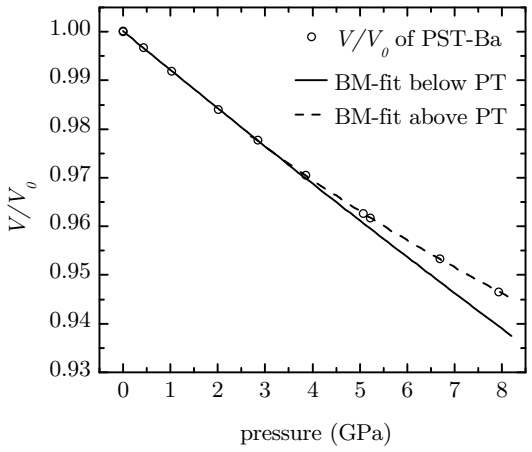

(a) Pressure dependence of the normalised unit-cell volume.

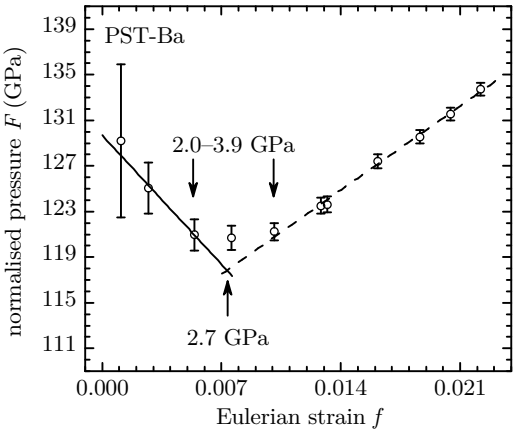

(b) Eulerian strain against normalised pressure.

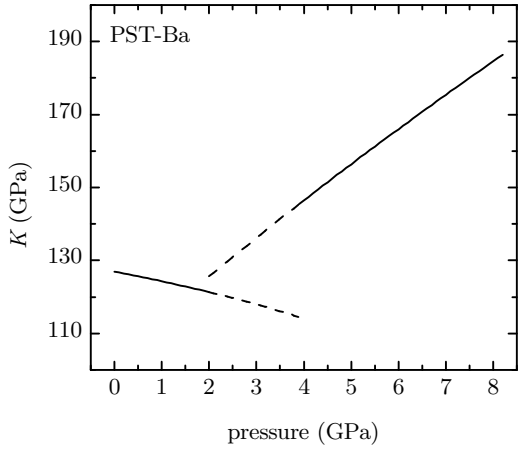

(c) Pressure dependence of the bulk modulus obtained from fitted EoS.

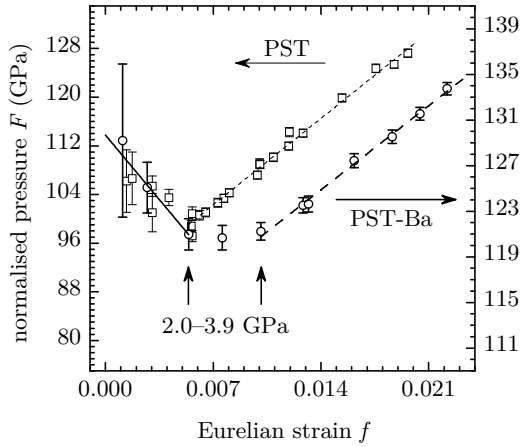

(d) Eulerian strain against normalised pressure in comparison with pure PST.

Figure 3.16: Volume compressibility of PST-Ba obtained by XRD measurements.

the considerably lower scattering contrast of Sc and Ta for neutrons compared to X-rays. It is therefore not possible to determine the state of B-site cation order from the neutron powder data, and consequently the state of chemical cation order on the B-sites does not affect the refined values of the model parameters in the $Fm\bar{3}m$ structure. The oxygen atom position is also fixed at 00¼ by the absence of ooo-reflection intensity. Rietveld refinements to low-pressure neutron diffraction datasets reveal that the oxygen atom displays significant anisotropy in the ADP. At ambient pressure, U_{11} and U_{33} are equal to 0.033(1) Å^2 and 0.013(1) Å^2 for PST and to 0.0242(8) Å^2 and 0.010(1) Å^2 for PST-Ba. For both compounds $U_{11} = U_{22} \sim 2.5U_{33}$. This may be indicative of static and/or dynamic local octahedral tilting within the structure, similar to that observed close to tilt transitions in other

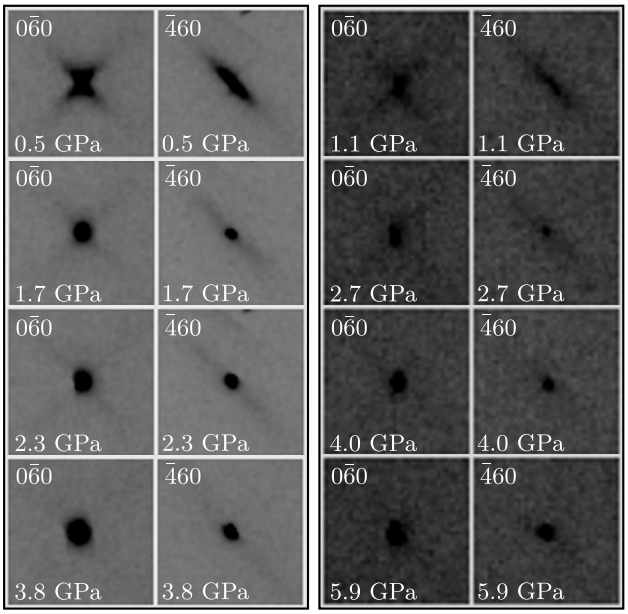

(a) PST. **(b)** PST-Ba.

Figure 3.17: Pressure evolution of the diffuse scattering for PST (a) and PST-Ba (b) at the reflections 0$\bar{6}$0 and $\bar{4}$60. The elastic phase transition occurs near 1.9 GPa for PST and between 2–4 GPa for PST-Ba.

perovskites (Goodwin et al., 2007). It is worth noting that the structure refinement to the 0.5 GPa synchrotron XRD data of PST in $Fm\bar{3}m$ also yields the same pattern of anisotropy in the oxygen ADP. This anisotropy slightly increases with pressure when approaching the high-pressure regime in which the structure is better refined in non-cubic setting. For both PST and PST-Ba, the isotropic ADP of the B-site cation obtained by the refinement to the ambient-pressure neutron powder diffraction patterns is 0.007(1) $\mathring{A}^2$, remaining constant within the uncertainties at all pressures, while that of the Pb atom on the A-site is 0.049(1) $\mathring{A}^2$, decreasing with pressure. The relatively large isotropic ADP of Pb indicates incoherent static and/or dynamic off-centre Pb displacements with a mean value slightly greater than 0.2 Å, which is consistent with the Pb off-centred shifts in lead-based relaxors estimated by other methods (Peng and Bursill, 1993; Zhou et al., 2004). Free refinements of a split position for the Pb site in the manner of Gvasaliya et al. (2006) resulted in the Pb refining to the special position at ¼¼¼ within the uncertainties. The refined unit-cell parameters are given in Appx. C (see Tab. C.2 and C.3 for PST and PST-Ba, respectively). The structural parameters obtained from the refinements are given in Tab. C.4.

At pressures above 1.51(2) GPa the neutron powder diffraction patterns exhibit ooo-reflections that are as sharp as the main eee-reflections (Fig. 3.18a). They significantly increase in intensity with increasing pressure (see Fig. 3.18b). In general, three possible structural features can contribute to the intensity of these pressure-induced ooo-reflections: chemical 1:1 B-site cation ordering, ordering of Pb and/or B-cation off-centred displacements

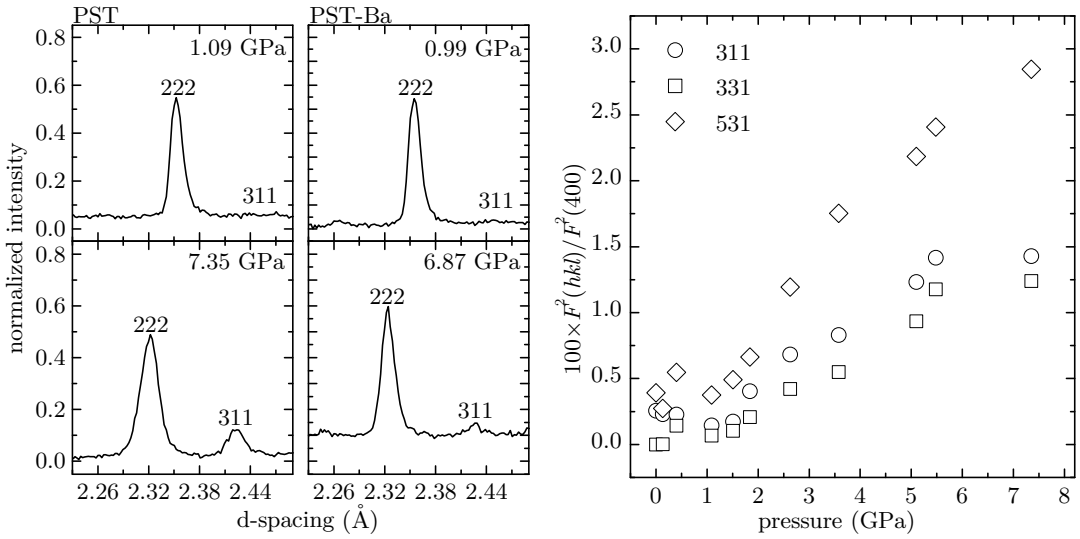

(a) Sections of the patterns at low and high pressures for PST and PST-Ba. Indices are given in $Fm\bar{3}m$.

(b) Pressure dependence of the normalised squared structure factor F^2_{hkl}/F^2_{400} for the superlattice reflections 311, 331, and 531 (indexed as $Fm\bar{3}m$) of PST obtained by LeBail fits.

Figure 3.18: Pressure dependence of superlattice reflections from neutron powder diffraction data of PST and PST-Ba.

in a pattern that maintains an F lattice, and octahedral tilting. As shown in Sec. 3.3.1, the only contribution at low pressures to the intensities of the ooo-reflections is from the B-site ordering. Given that the experiments are performed at room temperature, it is very unlikely that any changes in the B-site cation distribution could occur upon pressurisation and, hence, the pressure-enhancement of ooo-reflections cannot result from an increase in the degree of chemical B-cation order. The isotropy and the very small values of the ADP of B-cations for all pressure points studied indicate that within the sensitivity of diffraction B-cations are not off-centred and, therefore, ordering of off-centre displacements of B-cations is implausible. This is also supported by Raman scattering data, showing that pressure suppresses the local off-centring of B-cations detectable by this spectroscopic technique Mihailova et al. (2008a); Welsch et al. (2009a).

Figure 3.19 shows the $hk\bar{1}$ reciprocal space layer section of an {110}-cut PST crystal at 4.2 GPa. With the exception of the 111 reflection that consists only of the weak and broad contribution from the B-site cation ordering, the intensities of the ooo-reflections have significantly increased with pressure. Similarly, the systematic absence of reflections of type hhh, $h = 2n + 1$ is observed in disordered PSN (see Fig. 3.28). This clearly indicates that the structural distortion developing at higher pressures exhibits a strong pseudo-glide

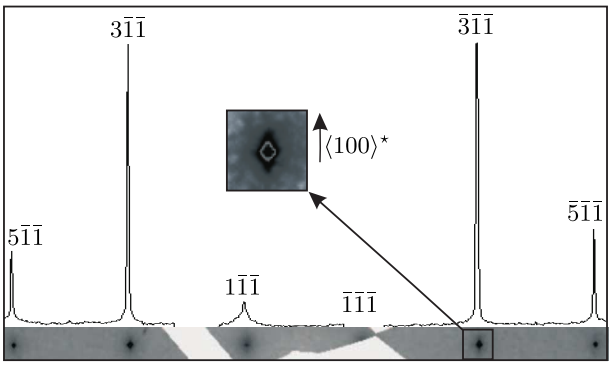

Figure 3.19: Section of the $hk\bar{1}$ reciprocal space layer at 4.2 GPa of a {110}-cut single crystal of PST with a line profile along $h\bar{1}\bar{1}$. The visible $1\bar{1}\bar{1}$ reflection arises from chemical ordered domains only, therefore it appears broad and with weak intensity. The other reflections exhibit strong and sharp components arising from octahedral tilting on top of the broad reflections arising from the B-site ordered domains.

symmetry along the cubic $\langle 111\rangle$ directions which is only broken by the weak reflections arising from B-site cation ordering. The existence of a glide pseudo-symmetry as revealed by the synchrotron XRD measurement on the {110}-cut PST sample (see Fig. 3.19) is also consistent with ordering of off-centred displacements of Pb atoms. However, such LRO shifts of Pb atoms can only contribute to reflections with $l = 2n$, indexed in $Fm\bar{3}m$ and cannot be responsible for the increasing intensity of the $l = 2n + 1$ reflections in the high-pressure phase. Therefore, pressure-induced LRO of tilted BO_6 octahedra is the only possible explanation for the increase in the intensities of ooo-reflections, so in the following, the possible tilt configurations in a perovskite-type structure built up of rigid octahedra are analysed in detail. It should be noted that the diffuse scattering streaks along the $\langle 100\rangle^\star$ directions in the $hk1$ layer indicate that the octahedral tilting pattern is not completely homogeneous across the entire single crystal sample.

Neither the neutron diffraction patterns, nor long exposure single-crystal synchrotron XRD patterns show evidence of any other additional diffraction maxima at high pressures. This means that only static distortions associated with phonon condensation at the R-point of the Brillouin zone of the average $Pm\bar{3}m$ structure are involved in the high-pressure phase (Howard and Stokes, 2005). This mode corresponds to anti-phase tilts of the octahedra about one or more of the unit-cell axes of the cubic structure. There are thus six possible symmetrically-distinct octahedral tilt systems for the high-pressure phase, of which the three with highest symmetry are $a^-a^-a^-$, $a^0b^-b^-$, and $a^0a^0c^-$ in Glazer notation (Glazer, 1972, see also Fig. 1.4a). The remaining three, $a^-b^-c^-$, $a^-b^-b^-$, and $a^0b^-c^-$, are subgroups of these (Howard and Stokes, 2005). Only the three highest-symmetry tilt systems will be considered in the following as the resolution of the neutron powder diffraction data does not allow to reliably refine the more complex lower-symmetry structures that correspond to B-site chemically disordered systems. In a perovskite with completely disordered cations on the B sites the corresponding space group symmetries are $R\bar{3}c$

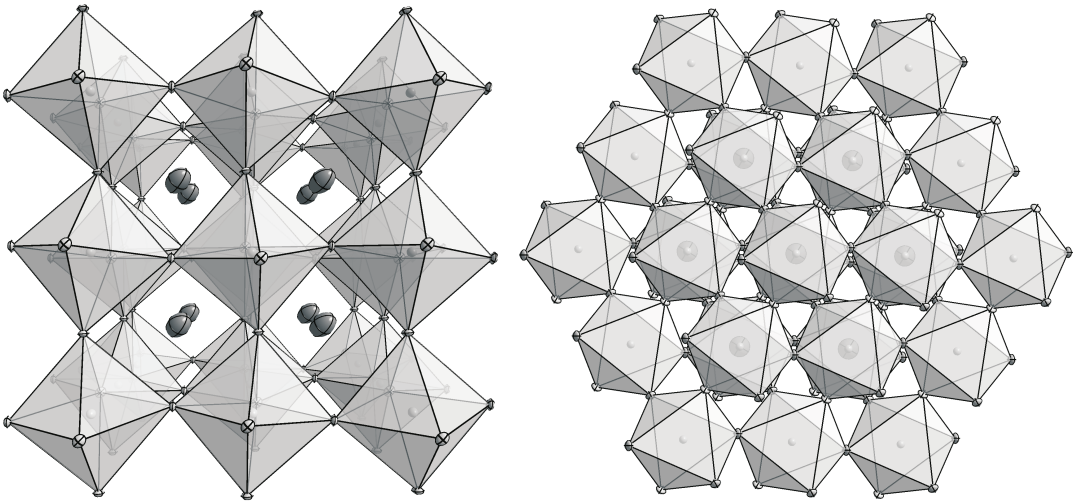

(a) Perspective view along the pseudo-cubic ⟨100⟩ direction.

(b) Plane view along the pseudo-cubic ⟨111⟩ direction.

Figure 3.20: The time and space averaged high-pressure structure of PST at 7.35 GPa in $R\bar{3}c$. The bright ellipsoids denote oxygen atoms with anisotropic atomic displacement parameters and forming octahedra around the B-cations with an $a^-a^-a^-$ tilt pattern. The dark ellipsoids represent Pb cations, having anisotropic atomic displacements enhanced along the pseudo-cubic ⟨111⟩ direction.

($a^-a^-a^-$), $Imma$ ($a^0b^-b^-$), and $I4/mcm$ ($a^0a^0c^-$). The same configurations of tilts can develop from the prototype structure of a chemically B-site ordered system with $Fm\bar{3}m$ symmetry, and the corresponding space groups for the three highest-symmetry tilts are $R\bar{3}$ ($a^-a^-a^-$), C2/m ($a^0b^-b^-$), and I4/m ($a^0a^0c^-$) (Howard et al., 2003, see also Fig. 1.4b). Thus, anti-phase octahedral tilting can be developed throughout the sample bulk, regardless of the intrinsic chemical inhomogeneity of (Pb,A″)(B′,B″)O_3 relaxors.

Rhombohedral systems:

Due to the c-glide pseudo-symmetry of the structural distortion at high pressures and the weak contribution of the B-site cation ordering to the intensities of the ooo-reflections in neutron powder diffraction, initial refinements were performed with a B-site disordered model in space group $R\bar{3}c$. Rietveld refinements to the data were completed with isotropic ADP for the B site, as anisotropic refinement resulted in isotropic values, and anisotropic ADP for the Pb and O sites. The refined high-pressure structure of PST exhibits strong octahedral tilting and significantly anisotropic displacements of the Pb cations (see Fig. 3.20).

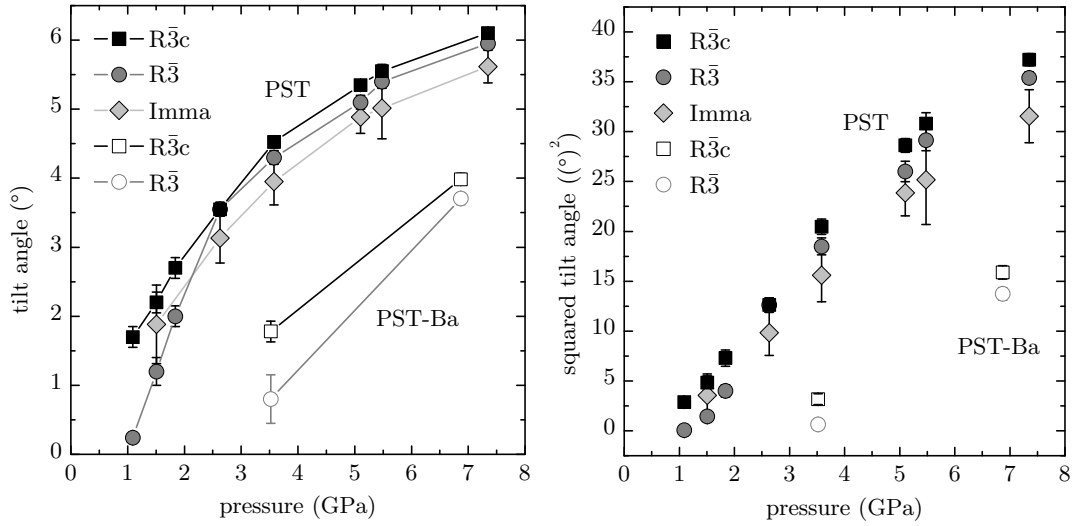

(a) $\omega(P)$. **(b)** $\omega^2(P)$.

Figure 3.21: Pressure dependence of the tilt angle ω and ω^2 for PST and PST-Ba.

The α-angle of the pseudo-cubic unit cell measures the symmetry-breaking strain from the cubic phase. However, due to the limited resolution of the diffractometer, the measured neutron powder patterns cannot resolve the small distortion from cubic existing above 1.9 GPa, resulting in a correlation of the lattice parameters of the high pressure phase with the peak width parameters. Thus, the pseudo-cubic α-angle is not a reliable estimate of the distortion of the structure from cubic symmetry. Therefore, the octahedral tilt angle $\omega(P)$ determined from the structure refinements was used as a more reliable measure for the distortion, as it is derived mainly from the intensities of the ooo-reflections. In rhombohedral perovskites with space group $R\bar{3}c$, the octahedron is constrained by symmetry to rotate around the 3-fold axis. Thus the tilt angle is equal to $(180 - \sphericalangle(\text{B-O-B}))/2$ and would be the primary order parameter for a pure tilt transition. The square of the tilt angle shows approximately a linear variation with pressure (Fig. 3.21b), similar to $LaAlO_3$ and $PrAlO_3$ $R\bar{3}c$ perovskites at high pressures (Zhao et al., 2004, 2009), corresponding to second-order behaviour in terms of Landau theory.

An extrapolation to zero of the squared tilt angles measured at high pressures suggests that tilting may already occur at 1.1 GPa (see Fig. 3.21b), i.e. below the critical pressure of 1.9 GPa determined from the static elastic softening in single-crystal XRD measurements. This is supported by the result that refinements show a significantly non-zero tilt angle at 1.5 and 1.1 GPa, even though there is no significant intensity detected at the ooo peak positions. It therefore appears that, on increasing pressure, the structure may first develop

a rhombohedral pattern of tilts within a unit cell that maintains a global cubic metric and then subsequently undergo a macroscopic transition to a phase with a distorted (non-cubic) unit cell.

In order to determine whether the results of the refinement in $R\bar{3}c$ symmetry, and in particular the magnitudes of the octahedral tilts, are being biased by the setting of $Q_{od} = 0$ (complete B-site disorder), refinements were performed in $R\bar{3}$ symmetry, which allows B-site ordering as well as other rotations and distortions of the octahedron due to the general position of the oxygen (Megaw and Darlington, 1975). In this space group the B and Pb cations can also be displaced along the 3-fold axis. However, general fits were unstable which is consistent with the symmetry restriction of the distortion having a *c*-glide, as explained above. Therefore the refinements were constrained to match the symmetry $R\bar{3}c$ except for the B-site cation ordering. A free refinement of Q_{od} results in $Q_{od} = 0$, corresponding to the $R\bar{3}c$ model. Thus, for the purpose of testing, Q_{od} was fixed to 0.5, which means site occupancies of 0.25/0.75 for the B cations, thus greatly over-estimating the known contribution of B-site order to the intensities of the ooo-reflections. However, the comparison of the refinements in $R\bar{3}c$ and constrained $R\bar{3}$ at high pressures (Tab. C.4) shows that the refined $\omega^2(P)$ is not dependent upon the value chosen for Q_{od} (Fig. 3.21b). Close to the transition however, the tilt angle is smaller for the refinement with $Q_{od} = 0.5$, as expected. Note that for most datasets, the $R\bar{3}c$ refinement with $Q_{od} = 0$ produces a slightly better statistical fit to the data. The ADP for the atoms in the $R\bar{3}c$ and the $R\bar{3}$ ($Q_{od} = 0.5$) refinements are very similar. There is no significant change in the isotropic ADP of the B cation in either refinement with pressure. The range of values is 0.005 to 0.007 Å^2, corresponding to mean displacements of 0.08 Å.

The evolution of the equivalent isotropic equivalent ADP for the Pb atom at higher pressures is entirely continuous with the values refined for the isotropic ADP in the cubic phase at lower pressures (Fig. 3.22a). Both refinements in $R\bar{3}c$ and $R\bar{3}$ show the Pb atom to be isotropic at 1.09(2) GPa with a mean displacement of 0.2 Å. At 1.5 GPa the ADP of the Pb atom becomes significantly anisotropic, with $U_{33} > U_{11}$ (Fig. 3.22a), corresponding to larger displacements along the cubic ⟨111⟩ direction. The value of 0.06 Å^2 for U_{33} corresponds to mean displacements of 0.24 Å. With increasing pressure both the displacements and the anisotropy decreases. If the trends were extrapolated to higher pressures, the ADP of Pb would become isotropic again around 10–12 GPa, with $U_{\text{iso}} \sim 0.015$ Å^2, and a mean displacement of 0.12 Å. The Pb cations are at the special positions $00z$ and $00z{+}½$, lying on the *c*-glide plane in the rhombohedral space groups.

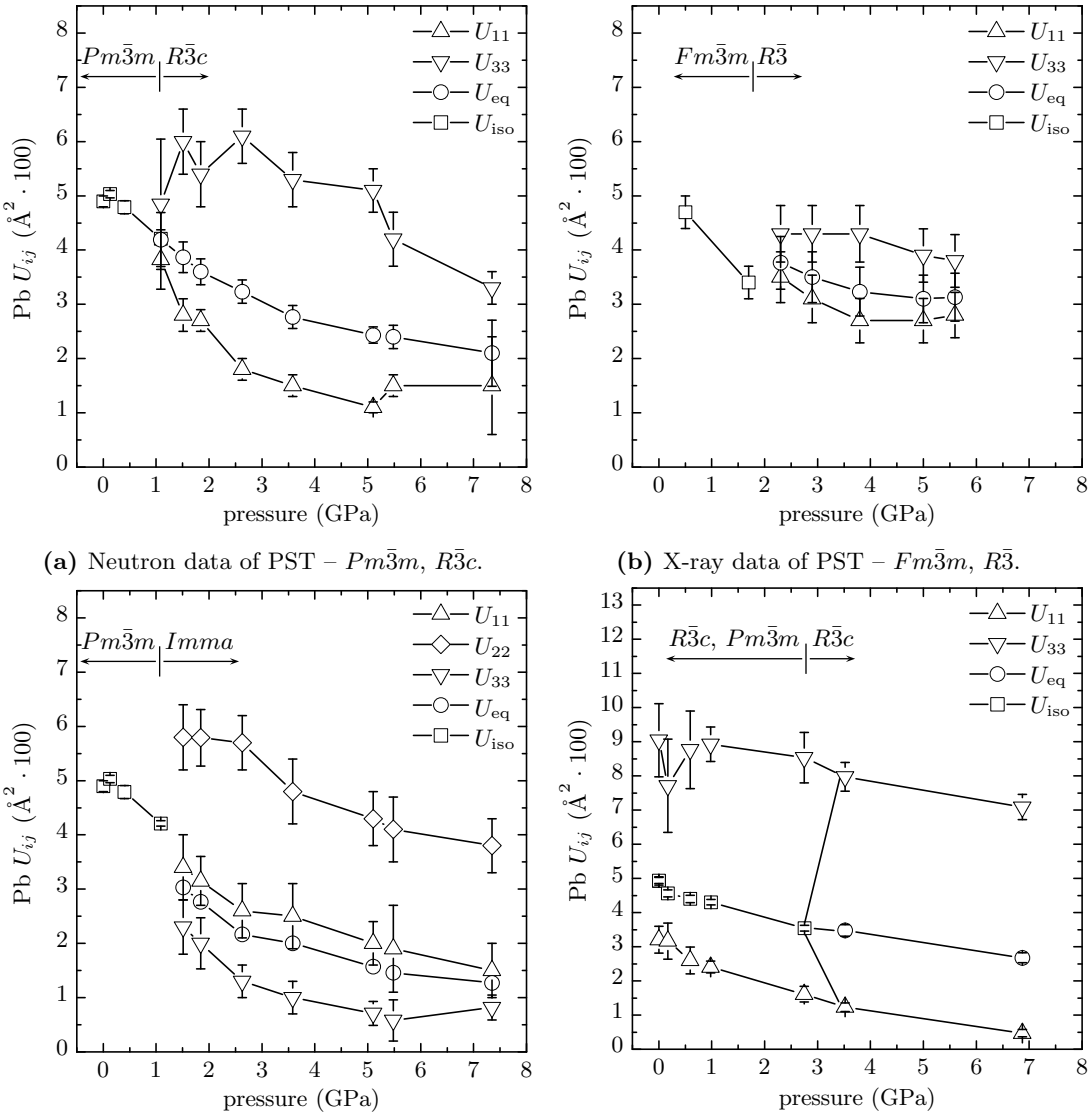

(a) Neutron data of PST – $Pm\bar{3}m$, $R\bar{3}c$.

(b) X-ray data of PST – $Fm\bar{3}m$, $R\bar{3}$.

(c) Neutron data of PST – $Pm\bar{3}m$, $Imma$.

(d) Neutron data of PST-Ba – $Pm\bar{3}m$, $R\bar{3}c$.

Figure 3.22: Pressure dependence of the isotropic and anisotropic Pb ADP of PST and PST-Ba.

Therefore, as mentioned above, Pb shifts can only contribute to reflections with $l = 2n$, indexed in $Fm\bar{3}m$, which become $l = 2n$ reflections in $R\bar{3}c$, and cannot be responsible for the increasing intensity of the $l = 2n + 1$ reflections in the high-pressure phase. It should be emphasised that the Pb position always refined to 00¼, indicating that there are, on average, no off-centre displacements of the Pb atoms with respect to their position in the prototype cubic structure. Thus, there is no evidence for LRO of Pb off-centre displacements and the refined anisotropy must therefore be attributed to Pb displacements along the cubic ⟨111⟩ direction that are, at most, ordered on a local length scale.

Refinements of the high-pressure structure to the single crystal XRD data are complicated by the twinning that must be present within the single-crystal sample as a result of the phase transition to rhombohedral symmetry. The refinements of the structure were therefore performed with a structure model in a unit cell with a cubic metric, an F-lattice, an inversion centre at the origin, and a single 3-fold axis parallel to [111]. The twinning was then modelled as a four-component twin generated by a four-fold rotation around [001], corresponding to the symmetry lost on transformation from cubic to rhombohedral symmetry. Due to a combination of the relatively weak scattering from the oxygen atoms and the twinning, it is not possible to refine the oxygen positional parameter. Thus, it was fixed to a value interpolated from the refinements to neutron powder diffraction data. The occupancies of the B sites were fixed to the values determined at 0.5 GPa, corresponding to $Q_{od} = 0.08$. The Pb atom was fixed at ¼¼¼. Together, these restraints correspond to $R\bar{3}c$ symmetry, apart from the chemical B-site cation ordering. The resulting refinements show that the anisotropy of Pb has the same sense as for the refinements to the neutron data, but the degree of anisotropy is smaller, and the overall decrease in U_{ij} with pressure is not as great (Fig. 3.22b). The 1.7 GPa X-ray dataset does not indicate anisotropic ADP for Pb, whereas the neutron powder dataset at 1.5 GPa does, which may be the reason for the small jump from the U_{iso} in space group $Fm\bar{3}m$ to the U_{eq} in space group $R\bar{3}$. These differences may be in part due to using an empirical extinction model in SHELX for the X-ray refinements.

Tetragonal and orthorhombic systems:

The symmetry of the structural distortion, restricted to having a glide symmetry along $\langle 111 \rangle$ cubic, is not limited to the rhombohedral space group $R\bar{3}c$. The tilt systems $a^0a^0b^-$ ($I4/mcm$) and $a^-b^-b^-$ ($Imma$) are also allowed by the appearance of the additional ooo-reflections without violating the glide symmetry.

Refinements in $I4/mcm$ ($a^0a^0c^-$) with complete B-site disorder consistently give significantly worse fits to the neutron powder diffraction data than the corresponding refinement in $R\bar{3}c$ ($a^-a^-a^-$). Thus $I4/mcm$ can be excluded as a possible space group candidate. This is presumably because $I4/mcm$ has tilts only about one of the $\langle 001 \rangle$ axes of the cubic aristotype, whereas $R\bar{3}c$ has the octahedra tilted about [111] of the cubic structure, which is equivalent to equal tilts about the three cubic axes [100], [010] and [001]. However, space group $Imma$ allows equal tilts about two of these three cubic axes, corresponding to rotation around [110] cubic, with the tilt system $a^0b^-b^-$ in a unit cell of $\sqrt{2}a$ by $2a$ by $\sqrt{2}a$

(for $a \sim 4$ Å). Refinements in $Imma$ ($a^0b^-b^-$) have a quality of fit indistinguishable from that of the $R\bar{3}c$ model, although they require considerable damping to keep them stable. The O site is split to O_1 at 0¼z, $z \sim 0.25$, and O_2 at x00, $x \sim$ ¼ (Woodward, 1997). The ADP of the oxygen atoms in $Imma$ are unusually large, but the positional parameters provide trends in the two $Imma$ tilt angles that parallel those for the rhombohedral refinements, with the average tilt following the R$\bar{3}c$ values closely (Fig. 3.21a). The tilt angles are also clearly non-zero below 1.51(2) GPa. Thus, the space group $Imma$ cannot be excluded as a possible model for the high-pressure phase of PST.

The B-cation site is constrained to lie on an inversion centre in $Imma$, but the Pb site becomes a special position at 0¼z, with $z \sim 0.75$, which allows the Pb atoms to be displaced in an anti-ferroic pattern parallel to [001] of the orthorhombic unit cell, corresponding to ⟨110⟩ of the cubic unit cell. However, as already shown, there is no requirement for the Pb to be shifted, thus the Pb position always refines back to $z =$ ¾ in both isotropic and anisotropic refinements. In contrast to $R\bar{3}c$, the Pb has $U_{22} \sim 2.5U_{11} \sim 4U_{33}$ (Fig. 3.22c), which suggests large displacements along the ⟨110⟩ cubic directions. Nonetheless, they show the same general behaviour as those obtained from the $R\bar{3}c$ and constrained $R\bar{3}$ refinements (Fig. 3.22a).

However, there are a few features that suggest that the $Imma$ model is a worse representation of the structure than $R\bar{3}c$. As mentioned above, the refinements in $Imma$ require considerable damping to keep them stable and the additional parameters do not improve the reduced χ^2 values compared to the refinements in $R\bar{3}c$. In addition, there is a discontinuity from the U_{iso} refined in $Pm\bar{3}m$ to the U_{eq} of $Imma$, (see 3.22c). Finally, the phase transition from $Pm\bar{3}m$ to $Imma$ (or for B-site ordered structures $Fm\bar{3}m$ to C2/m) is required to be of first order by Landau theory (Howard et al., 2003; Howard and Stokes, 2005), whereas the evolution of both the structure and the unit-cell parameters indicate that the observed phase transition near 1.9 GPa is second-order in character.

PST-Ba:

Following the results for PST, refinements were based upon a $R\bar{3}c$ model. Again, a $R\bar{3}$ model constrained to $R\bar{3}c$ was used to determine the influence of chemical B-site cation ordering, giving the same results as for the $R\bar{3}c$ model within the uncertainties. Only the octahedral tilt angle $\omega(P)$ has slightly smaller values as expected. The extrapolation of the squared tilt angle data suggests the appearance of LRO of tilts near 3 GPa (see Fig 3.21b). Figure 3.22d shows the refined Pb ADP. The U_{iso} decreases with increasing pressure as

in PST, however, in contrast to PST, the anisotropy is larger in the high-pressure phase. This can be the result of two features: the B-site ordered regions are larger in PST-Ba, allowing the Pb to shift more along the cubic ⟨111⟩ direction, corresponding to the U_{33} ADP; and the incorporation of Ba^{2+} having an isotropic electron shell destroys the coupling of the stereochemically active Pb^{2+} cations along the cubic ⟨110⟩ direction (see Sec. 3.2.1, which reduces the corresponding $U_{11} = U_{22}$ ADP. This is supported by the result that a rhombohedral refinement below 3.53(3) GPa does not lead to isotropic Pb ADP but rather shows the persistence of the anisotropy down to ambient pressure (Fig. 3.22d).

For completeness, refinements of the PST-Ba data were also performed with $I4/mcm$ and $Imma$ models. The $I4/mcm$ model gave significantly worse fits to the data as it did for pure PST. The $Imma$ model resulted in negative U_{22} ADP for the oxygen atoms, thus giving another strong indication that the rhombohedral symmetry is the most plausible for the high-pressure phase of Pb-based perovskite-type relaxors.

Finally, it should be noted that both ooo and eee peaks in the neutron powder diffraction datasets from both PST and PST-Ba display broadening at the highest pressures, above 5 GPa for PST, and at 6.9 GPa for PST-Ba. The Rietveld refinements show that this increase in width occurs for both the Gaussian and Lorentzian components of the pseudo-Voigt functions used to model the peak shapes. For PST at 7.35(4) GPa, both refined width parameters are approximately twice the values of the instrumental resolution, whereas for PST-Ba at 6.87(4) GPa, they increased about one-third. The uniformity of broadening of all peaks, and the fact that it is the same whatever symmetry chosen for the structure model, suggest that it is not due to a further symmetry reduction. Exploration of various refinement models for the broadening indicate that it arises from isotropic strain.

3.3.2 Lead scandium niobate, pure, Ba-, and Bi-doped

The pressure-induced evolution of the pseudo-cubic unit-cell volume of PSN, PSN-Ba, and PSN-Bi determined from in-house XRD experiments is shown in Figs. 3.23, 3.24, and 3.25, respectively. All the three compounds exhibit a change in the compressibility and consequently in the bulk modulus. Within the experimental accuracy of $\pm 10^{-4}$ Å^3, no detectable discontinuity in the unit-cell volume is observed, which indicates that the pressure-induced phase transition is effectively thermodynamically second-order. The EoS parameters fitted to the experimental points below P_c are $V_0 = 546.78 \pm 0.13$ Å^3, $K_0 = 103\pm$ GPa, $K_0' = 2.8 \pm 1.1$ for PSN, $V_0 = 546.42 \pm 0.14$ Å^3, $K_0 = 105 \pm 3$ GPa,

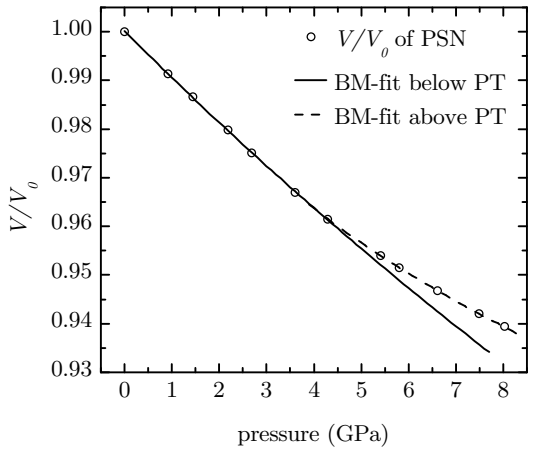

(a) Pressure dependence of the normalised unit-cell volume.

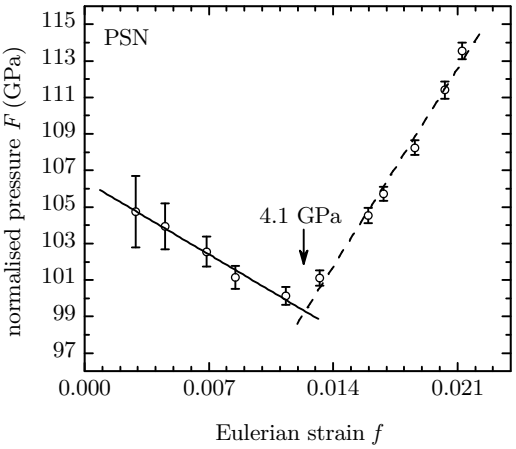

(b) Eulerian strain against normalised pressure.

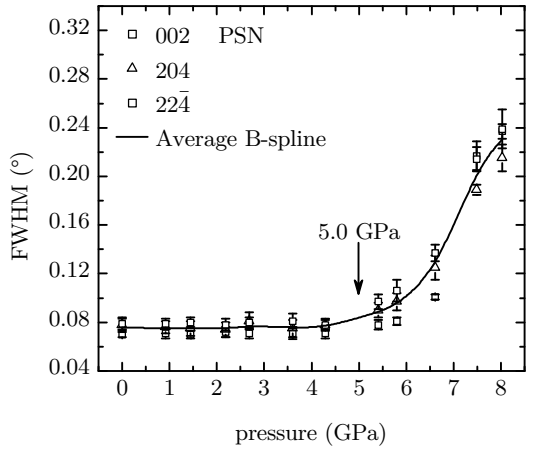

(c) Pressure dependence of the FWHM of representative reflections.

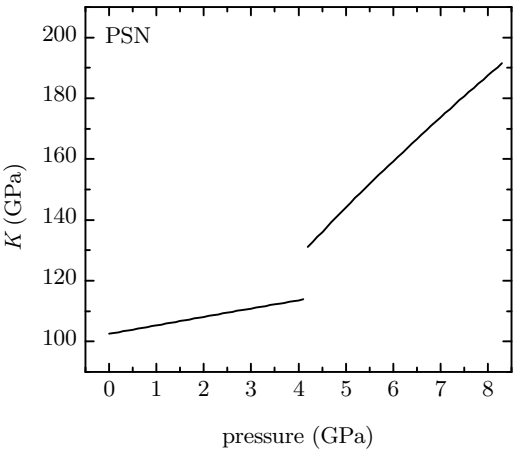

(d) Pressure dependence of the bulk modulus obtained from fitted EoS.

Figure 3.23: Volume compressibility of PSN obtained by XRD measurements.

$K_0' = 3.5 \pm 1.6$ for PSN-Ba, and $V_0 = 544.57 \pm 0.08$ Å^3), $K_0 = 105 \pm 2$ GPa, $K_0' = -0.2 \pm 1.4$ for PSN-Bi.

The critical pressures and the character of the phase transitions are better revealed by the f-F-plots (see Sec. 2.1.4 for details). The f-F plots of all three compounds clearly show elastic softening of both, the low- and the high-pressure phase, as they approach the phase transition pressure. For pure PSN the critical pressure is near 4.1 GPa, whereas the Bi-doped compound undergoes a phase transition at slightly lower pressure near 3.4 GPa. In the case of Ba-doped PSN, the elastic softening is less pronounced, especially for the low-pressure phase. The $F(f)$ minimum appears to be smeared out over a pressure range 3.5–4.3 GPa, rather than being sharp and well-defined at a certain pressure point

as it is the case for pure and Bi-doped PSN. The same behaviour has been observed for PST-Ba (see Sec. 3.3.1, which shows an even broader plateau-like minimum of $F(f)$ due to the higher Ba content. Thus the specific shape of the $F(f)$ dependence indicates a diffuse pressure-induced phase transition, which is related to the Ba-induced disturbance of coherent off-centred Pb^{2+} cations. This is also evident in the negligibly small change in the bulk modulus of PSN-Ba near the phase transition (Fig. 3.24d). In contrast to Ba^{2+}, the incorporation of Bi^{3+} does not smear out the phase transition. The pressure-induced phase transition in PSN-Bi is even more pronounced than that in pure PSN, both with respect to the slope of $K(P)$ below P_c as well as the difference between the low- and high-pressure value of K at the transition point $\Delta K(P_c)$. Considering the structural complexity of relaxors at ambient conditions, namely PNR inside a paraelectric matrix, one can assume that the high-pressure structure comprises ferroic nanodomains distributed within a non-ferroic matrix. Hence, the values of $\Delta K(P_c)$ and dK/dP suggest that the fraction of spatial regions undergoing a phase transition is largest for PSN-Bi, smaller for PSN, and smallest for PSN-Ba.

At pressures above the phase transition the diffraction peaks with hkl all even, indexed as $Fm\bar{3}m$, broaden (see Figs. 3.23c, 3.24c, and 3.25c). This broadening corresponds to diffraction peak splitting caused by symmetry lowering (Mihailova et al., 2008a, see also Sec. 3.3.1), which cannot be experimentally resolved due to the rather small symmetry-breaking strains. For PST the broadening is detectable immediately above the critical pressure (Mihailova et al., 2008a), whereas in the case of pure and doped PSN the broadening appears at a pressure higher than the transition pressure. This is most probably due to the smaller fraction of ferroic domains which have therefore less impact on the pseudo-cubic diffraction peaks. The characteristic pressure at which the FWHM start increasing can be roughly estimated to 5.0, 6.0 and 4.5 GPa for PSN, PSN-Ba and PSN-Bi, respectively. Therefore, the fraction of pressure-induced ferroic domains is largest in PSN-Bi and smallest in PSN-Ba.

Figure 3.26 shows reciprocal space layers reconstructed from the raw diffraction images of PSN, PSN-Ba, and PSN-Bi at three representative pressure values. The (hkl)-layers, with $l = 2n$ show the pressure evolution of the X-ray diffuse scattering originating from the PNR (see Sec. 1.3.4 for details). For all Pb-based perovskite-type relaxors studied up to now the diffuse X-ray scattering is along the $\langle 110 \rangle^\star$ directions of the reciprocal space and is strongly suppressed at HP (see Sec. 1.3.5 for details). As can be seen in Fig. 3.26, this is also typical of PSN, PSN-Ba, and PSN-Bi. The weakening of the X-ray diffuse

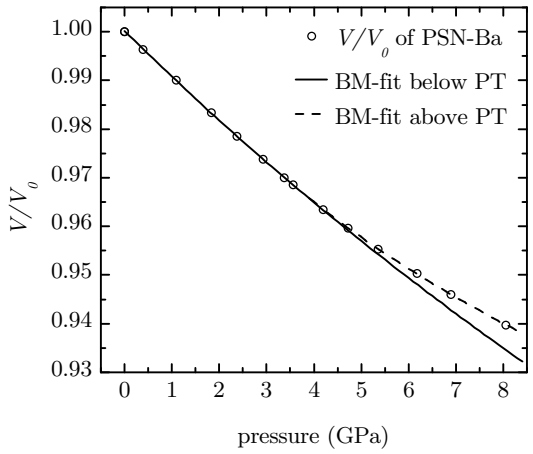

(a) Pressure dependence of the normalised unit-cell volume.

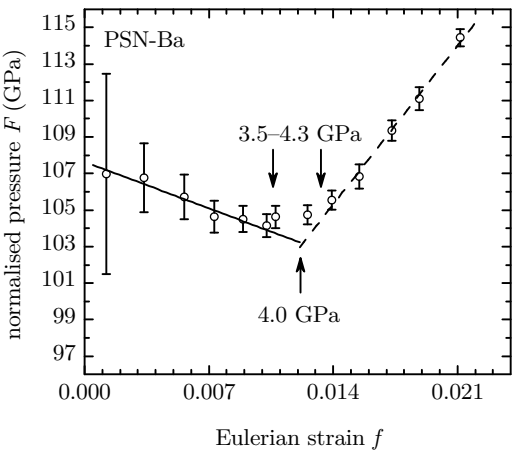

(b) Eulerian strain against normalised pressure.

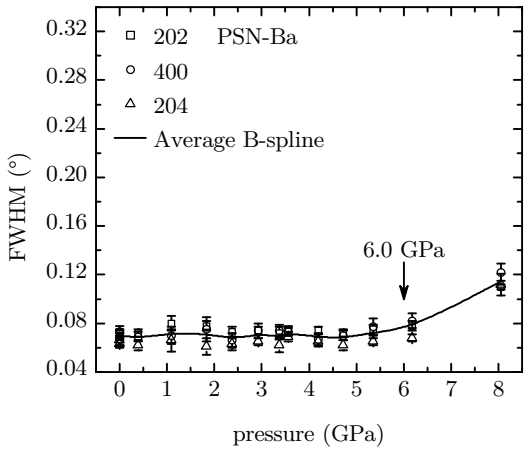

(c) Pressure dependence of the FWHM of representative reflections.

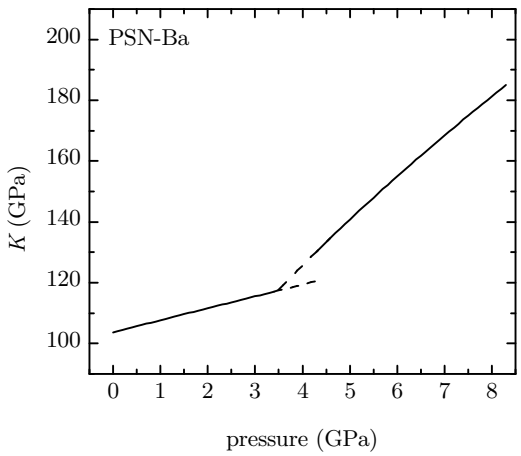

(d) Pressure dependence of the bulk modulus obtained from fitted EoS.

Figure 3.24: Volume compressibility of PSN-Ba obtained by XRD measurements.

scattering at high pressure indicates that the PNR comprising off-centred Pb and B-cation displacements present at ambient pressure (Pasciak et al., 2007; Welberry and Goossens, 2008) are altered by pressure. In general, the process of transformation could occur by the development of LRO of cation displacements and/or the suppression of the magnitudes of the displacements. Raman scattering data on all the three compounds clearly show that pressure leads to a decrease in the off-centred displacements of the B-cations (Maier et al., 2009). The structural refinements to synchrotron XRD and neutron diffraction data on pure and Ba-doped PST (see Sec. 3.3.1) indicate that the magnitude of Pb off-centred displacements is also reduced with increasing pressure. Therefore, the suppression of both B-cation and Pb off-centred displacements should be reflected in the intensity of the diffuse

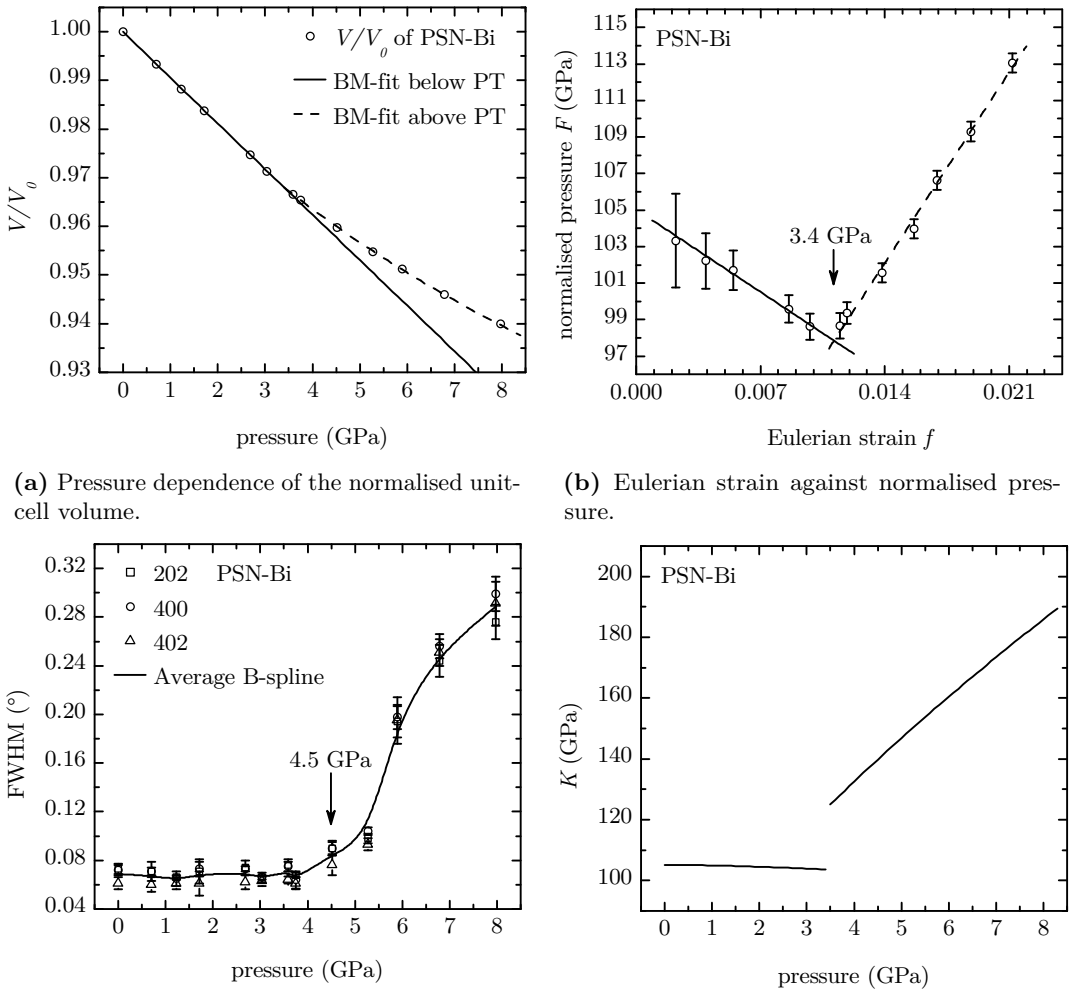

(a) Pressure dependence of the normalised unit-cell volume.

(b) Eulerian strain against normalised pressure.

(c) Pressure dependence of the FWHM of representative reflections.

(d) Pressure dependence of the bulk modulus obtained from fitted EoS.

Figure 3.25: Volume compressibility of PSN-Bi obtained by XRD measurements.

scattering. For all three compounds the X-ray diffuse scattering significantly decreases in intensity above the corresponding critical pressure, indicating that its reduction is also related to the development of the pressure-induced ordering processes, i.e. the development of anti-phase tilt pattern (see Sec. 3.3.1).

For all three compounds pressure-induced diffraction peaks in the ($hk1$) layers are observed above P_c and their intensity increases with pressure. At ambient pressure the presence of Bragg reflections with hkl, all odd, is indicative of chemical 1:1 B-site LRO. For all three compounds studied no odd-odd-odd diffraction peaks are observed in the DAC at low pressures. However, B-site ordering was detected for PSN in air but not in PSN-Ba and PSN-Bi (see Sec. 3.2.2 for details). The absence of the weak odd-odd-odd reflections

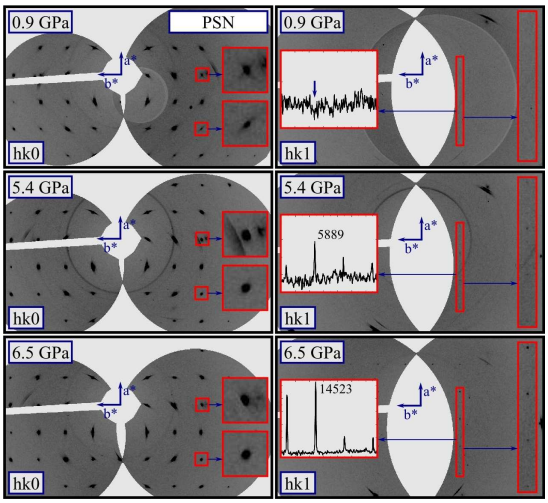

(a) PSN.

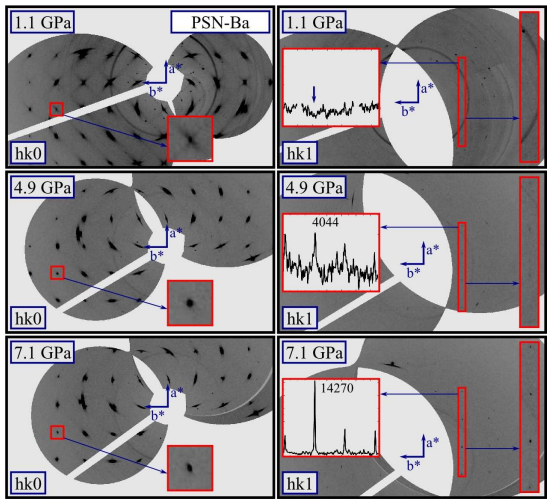

(b) PSN-Ba.

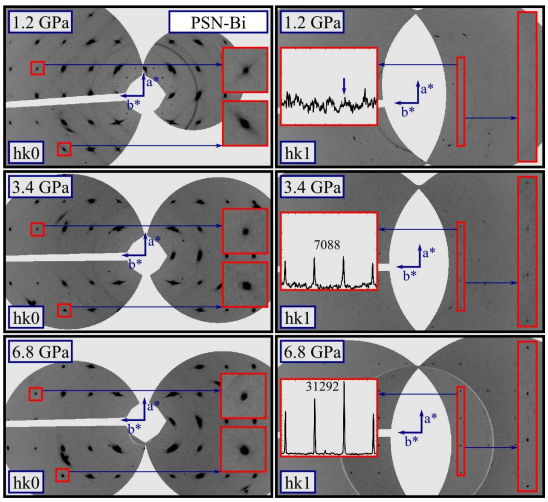

(c) PSN-Bi.

Figure 3.26: Reciprocal space layers of PSN (a), PSN-Ba (b), and PSN-Bi (c) at three representative pressures. The line profiles are along $[h\bar{3}1]$. The superlattice reflections appear first for PSN-Bi and are already pronounced near the critical pressure $P_c = 3.4$ GPa, as strong as the reflections observed for PSN and PSN-Ba at ∼1 GPa above P_c.

for PSN measured in the DAC is due to attenuation of the beam by the diamond anvils and is indicative of a very low degree of B-site order in PSN, comparable with that in Ba- and Bi-doped PSN. To verify the abundance and the size of B-site ordered regions, TEM experiments were performed (see Fig. 3.27). The SAED patterns of all three compounds reveal a low degree of chemical B-site order even on a local scale. Pure PSN sporadically exhibits odd-odd-odd reflections with extremely weak intensities, which confirms that B-site ordered regions are not a characteristic feature of this single-crystal sample. The odd-odd-odd Bragg reflections are better resolved in the SAED pattern of PSN-Bi and are strongest for PSN-Ba. Figure 3.27 also depicts the HRTEM image of PSN-Ba; the HRTEM images of PSN and PSN-Bi single crystals resemble that of PSN-Ba. A clear

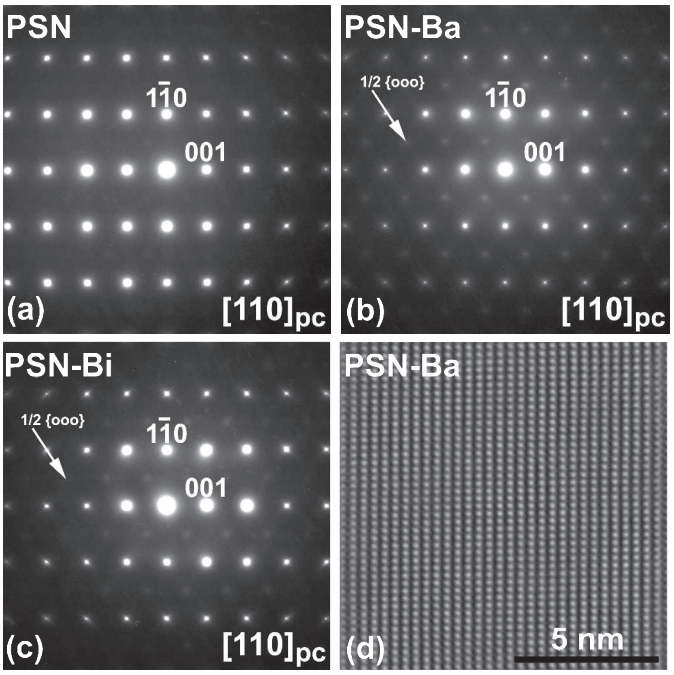

Figure 3.27: TEM images along the primitive cubic [110] direction.
(a) SAED pattern of PSN, showing extremely weak 1/2{ooo} superlattice reflections.
(b) SAED of PSN-Ba; 1/2{ooo} superstructure reflections are visible, marked with an arrow.
(c) SAED of PSN-Bi, also showing more intense 1/2{ooo} superlattice reflections as compared to PSN.
(d) HRTEM image of PSN-Ba; an inverse Fourier-transformed of the HRTEM image is overlayed with 50 percent opacity on the original HRTEM image.

indication for local ordering could not be verified by HRTEM analysis, but the absence of abundant large-size B-site ordered regions is apparent for all the three compounds.

Synchrotron XRD experiments performed on a {110}-cut single crystal of PSN clearly shows the absence of (hhh), $h = n$, reflections (see Fig. 3.28), whereas other odd-odd-odd Bragg reflections are observed. This systematic absence strongly indicates that the ferroic distortion results in a glide-plane pseudosymmetry of the average structure as in the case of PST (see Sec. 3.3.1).

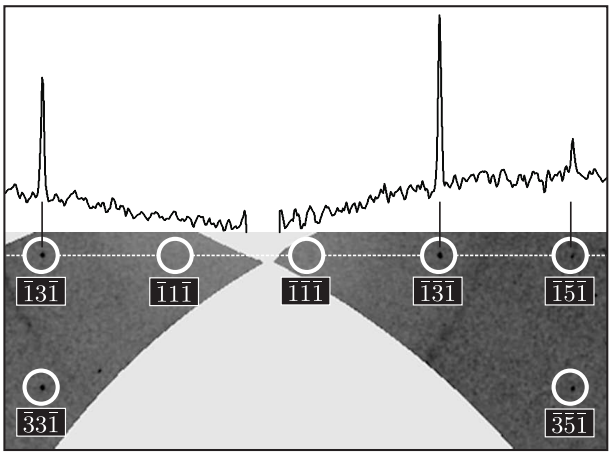

Figure 3.28: Section of the $hk\bar{1}$ reciprocal space layer at 5.4 GPa of a {110}-cut single crystal of PSN with a line profile along $\bar{1}k\bar{1}$. Reflections of type hhh with $h = n$ are not resolved due to the glide-plane extinction.

4 Discussion

4.1 Temperature-induced structural transformations

4.1.1 Lead scandium tantalate, pure and Ba-doped

The results of the comparative study on PST and PST-Ba are presented in Sec. 3.2.1 and elucidate the structural transformations occurring upon cooling, specifically at $T^\star$, a characteristic temperature for relaxors first proposed by Toulouse et al. (2005). In addition, the structural impact of Ba-doping is revealed which leads to the suppression of ferroelectric LRO at low temperatures, and hence, to the canonical relaxor state.

The existence of uncorrelated off-centred cation displacements above T_d is clearly revealed by the presence of the anomalous Raman signal near 53 and 240 cm^{-1}. At T_d = 700 K, the instantaneous Pb and B-cation displacements couple and form small-sized spatial regions comprising off-centred BO_6 octahedra and thus initial small PNR. The slope of the wave number and intensity increases of the B-localised mode near 240 cm^{-1} at T_d reveal the gradual increase in the off-centring of the BO_6 octahedra and the number of such octahedra, i.e. due to nucleation and further growth of the PNR. Due to the limited amount of points in the high-temperature powder XRD data, an impact of the coupling process on the average structure could not be revealed, however, a change in slope of $a(T)$ was observed for PSN and its doped variants (see Sec. 3.2.2)

For PST the system reaches saturation near 450 K. First, no further change in wave number of the B-localised mode is observed, which means no further increase in the B-cation off-centred shifts. Second, there is no further change in intensity, which means no further formation of off-centred BO_6 octahedra, within the sensitivity of Raman spectroscopy. On the other hand, the huge decrease in FWHM between 450 K and T_m indicates strong correlation processes between already formed small polar clusters comprising off-centred B cations. Thus, the strong drop of FWHM of the anomalous Raman scattering near 240 cm^{-1} defines best the temperature $T^\star$ (see Sec. 1.3.2, at which coupling of initial small PNR and their aggregation into larger PNR takes place, i.e. initial freezing of polar

nanoregions as proposed by Toulouse et al. (2005). The deviation of the pseudo-cubic lattice parameter near $T^\star$ indicates a change in the thermal-expansion properties, which is most probably related to the occurrence of local elastic fields at the interface between the PNR and the cubic matrix.

Thus, the temperature range between T_d and $T^\star$ can be considered as the range of intra-cluster structural phenomena, while the range between $T^\star$ and T_m as the range of inter-cluster structural phenomena. Hence, the development of the relaxor ferroelectric state is a two-step process. First, a coupling between off-centre shifts of adjacent atoms takes place, forming incipient polar spatial regions embedded in a paraelectric matrix. Second, a coupling between off-centre shifts of atoms from adjacent polar spatial regions occurs, extending and joining those regions at the expense of the paraelectric substance between them. In addition, just below $T^\star = 450$ K, the wave number of the anomalous Pb-localised mode near 53 cm^{-1} (Fig. 3.3a) becomes a constant down to approximately $T_\mathrm{m} = 280$ K. The intensity and the FWHM of this peak (not shown) are also almost constant within the range $T^\star$ to T_m. This indicates structural saturation in the system of off-centred Pb atoms and implies that massive coupling of the off-centred Pb atoms takes place within near the same temperature range as that of the coupling between off-centred BO_6 octahedra from different polar regions. Therefore, for PST, strong inter-cluster interactions occur between $T^\star$ and T_m, thus leading to a formation of ferroelectric LRO at low temperatures.

For PST-Ba, the temperature $T^\star = 490$ K is again well defined as the point where the FWHM of the B-localised mode strongly decreases and $a(T)$ deviates from a linear temperature dependence. This underlines the fact that $T^\star$ is a fundamental characteristic point of relaxors that exhibit a normal ferroelectric state and of those remaining in a nonergodic state. Below $T^\star$, the square wave number is almost constant, which suggests saturation of local structural deformations, i.e. the maximum of BO_6 off-centring is reached for the majority of the distorted species. However, the prominent increase in intensity at $T < T^\star$ reveals that the inter-cluster coupling processes are accompanied by further occurrence of polar species comprising off-centred B-site cations. This observation is consistent with the canonical relaxor behaviour of PST-Ba, which shows frequency dispersion of the dielectric permittivity at low temperature (Marinova et al., 2006). As expected, $I(T)$ becomes almost constant below T_m, which points to no or negligible further nucleation of polar clusters containing off-centre shifts of B-site cations. The coupling processes in the Pb system are smooth and not as well pronounced as in the case of PST.

The square wave number of the anomalous Pb-localised mode near 53 cm^{-1} shows a broad minimum centred near 350 K, which is well below $T^\star$, i.e. well below the temperature of massive coupling of off-centred B-site cations. Hence, due to the partial substitution of Ba for Pb, weaker inter-cluster interactions occur for PST-Ba between $T^\star$ and T_m, which are not strong enough to induce a formation of ferroelectric LRO domains. This is underlined by the observed intensity changes in the ($hk0$) layer which are most probably due to Ba-induced changes in the medium-range ordering of the Pb system.

Temperature lowering cannot induce hopping of atoms from one B site to another and, therefore, a change in the chemical order cannot be expected on cooling. Thus, the weakening of the reflections in the ($hk1$) layer upon cooling is probably due to the loss of periodicity in the B-cation system that results from a massive formation of very small-sized spatial regions comprising B-cation off-centre shifts, i.e. PNR, hence, the B-site cations contribute more to the diffuse scattering streaks than to the Bragg reflections arising from chemical ordering.

Two modes are involved in inter-cluster coupling processes, 135 cm^{-1} and 300-350 cm^{-1}. The former mode consists of vibrations of all types of atoms (oxygen and A- and B-site cations), and it is reasonable to expect that this mode is involved in inter-cluster interactions. The more interesting fact is that the Pb-O stretching mode is also responsible for cluster coupling. This explains the observed correlation between the intensity ratio ρ (Eq. B.1) and the development of ferroelectric domains as discussed in Appx. B. Furthermore, this emphasises the fact that the incipient ferroic Pb-O species existing above T_d govern the coupling between spatial polar regions comprising off-centred B-site cations and, thus, direct the formation of the ferroelectric state. Due to the dilution of the Pb system with Ba, the coherent length of distorted Pb-O species is shorter than that of PST, as revealed by the decrease in the intensity ratio ρ (Eq. B.1) of the Raman scattering at 300 and 355 cm^{-1}. Consequently, PST-Ba exhibits no development of ferroelectric LRO, as shown by the preserved polarisation of the Raman spectra (Marinova et al., 2006, see Appx. B for details), the frequency dispersion of the dielectric permittivity (Marinova et al., 2006), and the absence of additional Bragg reflections (see Fig. 3.1b) at low temperatures. Therefore, the high temperature Raman data presented in this work show that the incipient ferroic Pb-O species exist even at temperatures above T_d and are an inherent structural feature related to the chemical composition.

An interesting point is that in perovskite-type structures, Ba^{2+} and Pb^{2+} cations have the same valence, i.e. no local electrical fields due to charge imbalance are induced upon

Ba doping of PST. Therefore, the suppression of ferroelectric LRO and the enhancement of nonergodic relaxor state is related to the occurrence of local structural distortions and consequent local elastic strains resulting from the difference in the ionic radii of Ba^{2+} and Pb^{2+}. The fact that the size of chemically B-site ordered domains is larger for PST-Ba as compared to PST also highlights the primary importance of local elastic strains for the formation of relaxor ferroelectric state in perovskite-type materials.

4.1.2 Lead scandium niobate, pure, Ba-, Bi-, and La-doped

The results of the comparative study on PSN, PSN-Ba, and PSN-Bi presented in Sec. 3.2.2 underline the structural processes occurring near the for relaxors characteristic temperatures as shown for PST and PST-Ba (see Sec. 4.1.1). They also highlight the fundamental importance of A-site cations with LPE in governing the formation of regions with coherent ferroic atomic shifts in perovskite-type relaxors.

All the three compounds show a deviation of the anomalous Pb-localised scattering from the linear temperature dependence of the allowed peak, similarly to PST and PST-Ba (see Sec. 4.1.1), revealing Burns temperature. Thus, this is a general feature of Pb-based perovskite-type relaxors. In addition, T_d can also be detected by a change in slope of the linear $a(T)$ dependence at high temperatures as in the case of other Pb-based relaxors (Bonneau et al., 1991; Dkhil et al., 2009). Also common to PST and PST-Ba, $T^\star$ is revealed as the temperature at which the FWHM of the B-localised mode decreases, which indicates a massive coupling of off-centred B-cations from the existing PNR to form larger PNR. Again, the average structure is affected by the created strains as revealed by the deviation from linearity of $a(T)$. Thus, this underlines the nature of $T^\star$ being a characteristic temperature for lead-based perovskite-type relaxors (Dkhil et al., 2009). However, the values of T_d and $T^\star$ determined from the temperature evolution of the Raman spectra are approximately 50 K larger than those determined from the $a(T)$ dependence, because Raman scattering can detect structural transformations on their earlier stage of development.

The comparative study of PST and PST-Ba (see Sec. 4.1.1) has shown that the development of ferroelectric LRO of Pb-based perovskite-type relaxors at low temperatures is favoured by a strong coherence of the distorted Pb-O system, existing at high temperature. The substitution of Ba for Pb substantially enhances the relaxor behaviour and it has much stronger impact on the structure than the charge imbalance associated with compositional B-site disorder. As stated in Sec. 4.1.1, barium has the same valence as Pb occupying

the A-site in the perovskite structure, which means that Ba doping does not introduce additional local electric fields in the structure. However, incorporation of Ba^{2+} leads to strong local elastic fields due to the larger ionic radius as compared to that of Pb^{2+} as well as due to the fact that Ba^{2+} does not form LPE, contrarily to Pb^{2+} (Cohen, 1992; Chen et al., 1996). To further clarify the primary role of local elastic fields vs. local electric fields in Pb-based perovskite-type relaxors, it is necessary to analyse the effect of an A-site dopant having a different valence state but a similar outermost electron shell as Pb^{2+}. Bismuth is the appropriate model dopant, because it is three-valent, i.e. its incorporation in the structure would result in charge imbalance, and it shows a strong affinity to form stereochemically active lone pairs, i.e. Bi^{3+}-doping would barely disturb the system of existing LPE. Besides, the ionic radius of Bi^{3+} is smaller than that of Pb^{2+} and, hence, the local elastic stress in the vicinity of doped Bi^{3+} cations would be much smaller than that induced by Ba^{2+}.

A striking result is that on cooling strong depolarisation of the Raman spectra is observed for PSN-Bi, but not for PSN. This depolarisation is due to the occurrence of ferroelectric domains (see Appx. B for details), as it can be seen in the case of PST which undergoes a phase transition to a normal ferroelectric state near T_C and exhibits abundance of PNR just above T_C, as indicated by the strong X-ray diffuse scattering (see Fig. 3.1a). The Raman scattering of PST remains well polarised above T_C, whereas a strong, abrupt increase in the cross-polarised Raman intensity near 820 cm^{-1}, accompanied by equalisation of the overall Raman scattering in $Z(XX)\overline{Z}$ and $Z(XY)\overline{Z}$ geometries, occur below T_C Mihailova et al. (2007c). This clearly demonstrates that a jump of cross-polarised intensity near 820 cm^{-1} indicates establishment of crystalline ferroelectric domains. As can be seen in Fig. 3.10, such spectral changes are observed for PSN-Bi. Therefore, the substantial depolarisation of the Raman scattering of PSN-Bi below 200 K reveals abundance of crystalline ferroelectric domains in the structure.

Stoichiometric PSN shows a slight increase in the Raman scattering depolarisation below 300 K (see Fig. 3.10), which is consistent with the occurrence of rhombohedral domains detected by synchrotron XRD diffraction at low temperature. However, the overall weak depolarisation of PSN indicates that paraelectric regions prevail over ferroelectric LRO domains even at $T = 100$ K, which is well below T_m. This is underlined by the fact that the $\omega(T)$ dependencies of the allowed and anomalous Pb-localised peak are different at low temperatures and that the lattice parameter remains pseudo-cubic at low temperatures.

The maximum of $a(T)$ near T_a is therefore related to a metastability of the system during the cubic-to-rhombohedral phase transition occurring in some spatial regions.

Thus, the comparison between the temperature evolution of the spectral depolarisation of PSN and PSN-Bi reveals that the substitution of Bi^{3+} for Pb^{2+} even favours the formation of regions with coherent ferroic atomic shifts. This highlights the dominant role of the system of LPE over the A-site charge imbalance to govern the structural transformations in perovskite-type ferroelectrics.

Due to the different nature of interaction processes between the probe radiation and the solid-state sample, XRD and Raman scattering have different length scales of sensitivity. XRD is essentially an interference process of elastically scattered probe radiation and requires a periodic atomic array sized more than 10 unit cells (usually more than 100 Å) to generate Bragg reflections. Raman scattering is based on the change in energy of the probe radiation and for non-metal materials only a few unit cells (usually ∼30-40 Å) are necessary to give rise to crystal normal phonon modes. Consequently, Raman spectroscopy can detect crystalline regions of a size insufficient to generate Bragg reflections in the diffraction pattern. Hence, a considerable part of ferroelectric domains which give rise to the depolarisation of the Raman scattering may contribute to the observed X-ray diffuse scattering. Indeed, a coexistence of diffuse scattering streaks and a weak Bragg reflections at its crossing is observed (see Fig. 3.8a). In this regard, PSN-Bi develops a medium-range ferroelectric ordering, which stands between the PNR in canonical relaxors and ferroelectric LRO domains in normal ferroelectrics. The resemblance of $\omega(T)$ for the $Z(XX)\overline{Z}$ and $Z(XY)\overline{Z}$ peaks of the Pb-localised mode below 200 K indicates the predominance of ferroelectric LRO state. Therefore, the substitution of Bi^{3+} for Pb^{2+} modifies the coupling processes in the system of off-centred Pb atoms: the size of ferroelectric domains at low temperature is reduced, but the fraction of ferroelectric over paraelectric spatial regions is substantially enlarged. Thus, the effect of the associated charge imbalance is dominated by the much stronger influence of the system of LPE, which results in a ferroelectric LRO state clearly resolved by polarised Raman spectroscopy and on the limit of the sensitivity of single-crystal XRD.

The depolarisation of Raman scattering for PSN-Ba is very low and almost temperature independent, as it is expected to be for a canonical relaxor structure consisting of PNR distributed in a paraelectric matrix, as in the case of PST-Ba. In addition, no plateau in the ω(T)-dependence of the anomalous Raman scattering originating from the Pb-localised mode is observed and no ferroelectric LRO is detected at low temperature. This clearly

evidences that coherent Pb off-centred shifts, i.e. aligned LPE govern the development of PNR into ferroelectric domains whereas local elastic fields associated with substitutional disorder in the A-site hinder the occurrence of ferroelectric LRO.

The importance of the A-site LPE system is again underlined by the fact that PSN-La does not develop ferroelectric LRO at low temperatures. La^{3+} introduces an A-site charge imbalance as Bi^{3+}. However, La^{3+} has no affinity to form LPE, thus the host system of LPE associated with A-site cations is strongly disturbed. As a consequence, no ferroelectric LRO can be formed at low temperatures.

4.2 Structural phase transitions under high pressure

4.2.1 Lead scandium tantalate (PST), pure and Ba-doped

The structural state of the high-pressure phase of Pb-based perovskite-type structures is still unknown (see Sec. 1.3.5 for details). In order to reveal the high-pressure structural state, a combined neutron powder diffraction and single-crystal XRD study on PST and PST-Ba is presented in Sec. 3.3.1. PST is a very suitable model compound to study pressure-induced structural changes in this class of materials because at ambient conditions PST is in the ergodic relaxor state, close to T_m, and exhibits an abundance of PNR (see Sec. 3.2.1). In addition, the stoichiometry of this compound allows for the existence of spatial regions with a chemical 1:1 B-site LRO embedded in a chemically disordered matrix. The in-house single-crystal XRD measurements reveal a continuous phase transition near 1.9 GPa for PST (Mihailova et al., 2008a), involving elastic softening of both phases as revealed by the $K_T(P)$ dependence. The diffuse scattering is strongly suppressed by pressure increase when the transition pressure is approached.

The neutron powder and synchrotron single-crystal XRD data show that the transition is associated with a structural evolution that results in a continuous and significant increase in the intensities of ooo-reflections, with the exception of the 111 reflection (as indexed in space group $Fm\bar{3}m$). The constancy of the 111 reflection is critical; it shows that the structural distortion arising from the phase transition must have a glide pseudo-symmetry along the $\langle 111 \rangle$ cubic directions and, because the Pb atoms occupy special positions, it means that they cannot contribute to the intensities of the ooo-reflections. Since the degree of B-site cation ordering is unlikely to change with pressure at room temperature, these arguments are alone sufficient to demonstrate that the structural evolution of PST above the phase transition must involve octahedral tilting.

No other classes of reflections appear in either the X-ray or neutron diffraction patterns, which unambiguously identifies the octahedral tilting pattern as being anti-phase in character. Refinements to the neutron powder diffraction data in the three possible space groups with highest symmetry, namely $R\bar{3}c$ ($a^-a^-a^-$), $I4/mcm$ ($a^0a^0c^-$), and $Imma$ ($a^0b^-b^-$), corresponding to complete B-site disorder, all confirm that octahedral tilting explains the evolution of the diffraction patterns. It is found that $R\bar{3}c$ and $Imma$ provide significantly better fits to the data than $I4/mcm$, strongly suggesting that the tilt system involves simultaneous anti-phase tilts around all three pseudo-cubic axes. Refinements in $R\bar{3}$ of a model with an unrealistically large degree of B-site cation order also shows the development of octahedral tilting.

In discussing the refined structures it is crucial to bear in mind that they constitute some form of time and space average over a complex local nanoscale structure that, at least at ambient conditions, is comprised of dynamic polar nanoregions overlain upon spatial regions exhibiting either chemical B-site cation order or disorder. The average structure that is obtained from refinement to Bragg diffraction intensities therefore depends not only on the types of local domains present in the sample, but also on their sizes, relative orientations and characteristic atomic displacements. Thus, the refined structure represents the LRO present in the sample, but the LRO parameter determined in this way will almost always be much smaller than the short-range order present on the local scale of a few unit cells.

In the case of PST, from ambient pressure to ∼1.1 GPa, the Pb atoms are locally displaced but are not ordered on the diffraction length scale. If octahedral tilts are present, then they are only coherent over a short length scale, and the metric of the structure remains cubic. The isotropic atomic displacement parameter of Pb initially decreases with increasing pressure, as would be expected. However, at 1.5 GPa the displacement ellipsoids become significantly anisotropic, elongated along the cubic ⟨111⟩ directions. Structural refinements revealed no evidence for coherent static displacements of Pb atoms, which indicates that they can only be locally ordered. Although the presence of glide symmetry in the global structure requires anti-ferroic Pb displacements, locally they could be ferroically ordered. The development of the Pb displacement anisotropy is associated with the development of anti-phase tilting of the BO_6 octahedra, but within a unit-cell metric that initially remains cubic. The octahedral tilting develops continuously with increasing pressure, leading to an average symmetry decrease from cubic to rhombohedral. The weak diffuse scattering streaks along $\langle 100 \rangle^\star$ associated with the ooo peaks indicate that

the tilting is not completely homogeneous across the entire single crystal, and that there are faults or domain walls parallel to {100} cubic. Whether the streaks are solely the result of the development of rhombohedral domains all of which have the same degree of tilt but of different orientations, or also arises from domains with different degrees of octahedral tilts, cannot be determined from the available data. The broadening of the reflections at higher pressures can be attributed to the development of coherency strains which become larger as the rhombohedral distortion from cubic increases; that is the regions close to the domain walls will be strained to coherently match the neighbouring domains, while the interiors of the domains will relax and exhibit the full rhombohedral distortion.

The heavily Ba-doped compound shows the same development of structural distortion, but shifted to higher pressures. This can be understood as the result of two effects. The substitution of the larger Ba cation for Pb introduces elastic fields that expand the structure and thus delay the development of octahedral tilting. Further, the Ba dilutes the Pb, thus reducing the coherency in the PbO system (Welsch et al., 2009a) and the cooperative development of local displacements of the Pb atoms. Together, the results on pure PST and PST-Ba therefore suggest that the transition to the high-pressure phase is initially a cooperative phenomenon involving both the development of short-range ordering of Pb displacements along ⟨111⟩ cubic and octahedral tilting. Higher pressures drive further octahedral tilting (as the mechanism to reduce the volume, (Angel et al., 2005)) and this consequently reduces the A-site cavity volume and hence the overall magnitude of Pb displacements. Based on the high-pressure data published on PMN (Chaabane et al., 2003; Rotaru et al., 2008), PZN (Janolin et al., 2006), PMT (Gvasaliya et al., 2006), and PSN (see Sec. 4.2.2) it can be concluded that the same pattern of long-range-ordered anti-phase octahedral tilts and short-range ordered Pb-displacements also develops in these compounds at high pressures, and is therefore a common feature of the high-pressure phases of lead-based perovskite-type relaxor ferroelectrics.

4.2.2 Lead scandium niobate (PSN), pure, Ba-, and Bi-doped

The relaxor ferroelectric PSN shows a pressure-induced phase transition near 4.1 GPa, involving elastic softening of both phases. A moderate level of A-site doping with Ba ($x = 0.07$) and Bi ($x = 0.02$) slightly decreases the critical pressure. However, the change in the critical pressure does not correlate with the degree of doping, revealing the complex effect of the two dopants on the atomic arrangements in Pb-based perovskite type relaxors, due to the difference between the electronic structures of Ba and Bi. The

replacement of Pb^{2+} in the A-sites by isovalent cations (Ba^{2+}) having a larger ionic radius and no stereochemically active LPE smears the pressure-induced phase transition due to the introduction of local elastic fields in the structure. By contrast, the replacement of Pb^{2+} in the A-sites by aliovalent cations (Bi^{3+}) having nearly the same ionic radius and active LPE enlarges the fraction of spatial regions with a pressure-induced ferroic distortion, resulting in a more pronounced phase transition of the average structure. The much stronger diffraction intensities of the additional odd-odd-odd peaks for PSN-Bi, as compared to pure and Ba-doped PSN, unambiguously reveal that the incorporation of 3-valent cations with LPE into the host system of two-valent cations with LPE enhances the distortion to lower symmetry. The distinctive effect of the two types of A-site dopants on the structural changes under pressure is totally consistent with the corresponding effect on the temperature-driven structural transformations in Pb-based relaxors (see Sec. 4.1.2). Thus, the local electric fields associated with Bi^{3+} incorporated on the A-site induces additional nucleation of non-cubic structural species which enhances the overall ferroic ordering on temperature decrease as well as on pressure increase.

The narrow FWHM of Bragg reflections with hkl, all odd, observed at $P > P_c$ points to long correlation lengths of coherently scattering domains. As the chemical order cannot change with pressure, the additional odd-odd-odd Bragg reflections must originate from the pressure-induced structural transformations. As in the case of PST, three distinct processes can contribute to these diffraction peaks: anti-phase octahedral tilting, an anti-parallel ordering of off-centred Pb cations, and a decrease of uncoupled polar B-cation displacements as revealed by Raman spectroscopy (Maier et al., 2009), which would facilitate the observation of spatial regions with chemical B-site ordering. Calculations show that the suppression of incoherent off-centre displacements of B-site cations cannot give rise to the observed XRD intensity. Besides, the TEM data clearly show the absence of abundant regions with B-site LRO, which may give rise to the observed sharp diffraction peaks. Thus the pressure induced diffraction peaks can result from either ferroic order of Pb displacements and/or development of coherent tilting of the BO_6 octahedral system. However, the systematic absence of hhh, $h = n$, reflections strongly indicates that the ferroic distortion results in a glide-plane pseudosymmetry of the average structure. Thus, anti-parallel ordered Pb displacements cannot contribute to the hkl, all odd, reflections. Therefore, the appearance of those reflections is due to pressure-induced anti-phase octahedral tilting as in the case for PST and PST-Ba. Hence, anti-phase octahedral tilting is a characteristic feature of the high-pressure phase of Pb-based perovskite-type relaxors.

5 Conclusion

The isovalent substitution of Ba^{2+} for Pb^{2+} in lead-based perovskite-type relaxor ferroelectrics with a partial degree of chemical B-site order suppresses the ferroelectric LRO at low temperatures, regardless of the degree of chemical B-site order. The effect of Ba^{2+} is twofold. On one hand, the larger ionic radius in comparison to Pb^{2+} introduces local elastic fields, i.e. local strain, reducing the coherency in the distorted PbO system. On the other hand, Ba^{2+} does not form LPE, thus it disturbs the system of LPE associated with A-site-positioned Pb^{2+} which is vital for the formation of ferroelectric LRO. Therefore, the local electric fields associated with the chemical disorder of the heterovalent B-site are of minor importance for the suppression of ferroelectric LRO below T_{m} as compared to local elastic fields associated with substitutional A-site doping. The importance of an undisturbed orientational order of LPE is underlined by the effect of A-site doping with Bi^{3+} which also forms LPE. Despite the additional charge imbalance created by A-site positioned Bi^{3+}, the fraction of domains with ferroelectric LRO is even enhanced as compared to the pure compound. Thus, the disturbance of the coherent LPE system associated with A-site cations is vital for the suppression of ferroelectric LRO below T_{m}.

Regardless of the type and degree of doping, all studied compounds undergo a pressure-induced phase transition involving elastic softening of both phases. Rietveld refinements to neutron powder diffraction revealed that the high-pressure phase is associated with the development of long-range ordered anti-phase tilting of BO_6 octahedra which continuously evolve with increasing pressure. The refinements show that the $R\bar{3}c$ is the most likely space group. No evidence for long-range coherent static displacements of Pb atoms was found, as revealed by the anisotropic displacement ellipsoids. The presence of glide symmetry in the average structure requires anti-parallel Pb displacements but locally they could be ferroically ordered. A strong suppression of the diffuse scattering in the vicinity of the pressure-induced phase transition is found to be a characteristic feature of all compounds and it indicates the vanishing of PNR at high pressure.

Doping with Ba^{2+} smears out the pressure-induced phase transition over a pressure range and hampers the development of the high-pressure structural state. In contrast, doping

with Bi^{3+} reduces the critical pressure and enhances the structural distortions associated with the high-pressure phase. Therefore, the effect of local elastic fields and disturbance of the LPE system on the pressure-driven phase transition resembles that found for the temperature-driven structural phase transformations: the suppression of ferroic LRO.

A Preparation of high-pressure single-crystal X-ray diffraction experiments

A.1 The Boehler-Almax plate diamond anvil cell

The Boehler-Almax plate DAC (Boehler, 2006) follows the principle of two opposing steel plates. However, instead of pressing them together parallel to each other governed by guide pins, pressure is generated by elastic deflection of the plates. This gives higher precision in the alignment of the diamonds at lower cost. Figure A.1 shows the parts of the plate DAC. One diamond anvil is fixed to the top plate whereas the other anvil is fixed on a xy-stage which is put into the bottom plate. This allows for a horizontal adjustment of the diamonds while the vertical adjustment is achieved with the plate alignment screws which also serve the purpose to adjust the initial gap between the two anvils. The gasket is glued on the gasket holder which in turn is put onto the bottom plate, ensuring a unique gasket position. Pressure is applied using gear tool on the fine-threaded pressure screws, which are initially tightened with a torque of 0.4 Nm using a torque wrench. The gear tool allows for

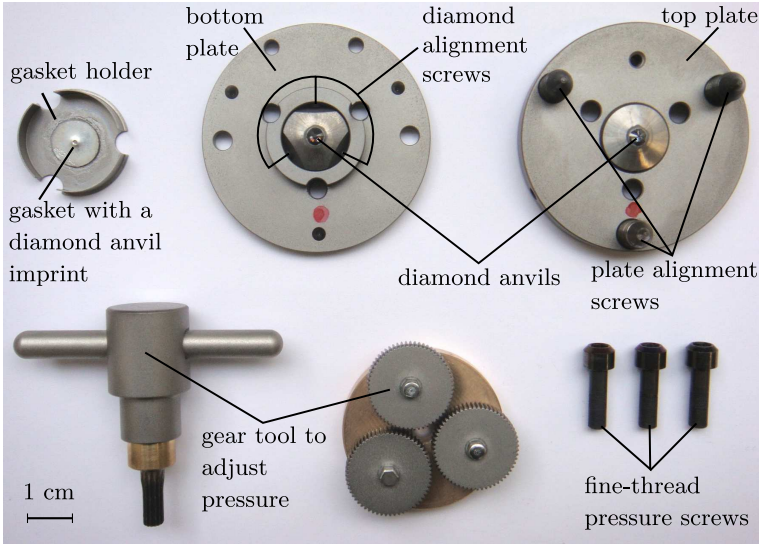

Figure A.1: The Boehler-Almax plate DAC (Boehler, 2006). The gasket holder ensures a unique gasket position. Pressure is adjusted with the fine-thread pressure screws via the gear tool, ensuring equal tightening of the screws which are initially tightened with a torque wrench to 0.4 Nm. During the alignment of the cell, the diamond anvils are horizontally and vertically adjusted via the alignment screws.

equal tightening of the screws, preventing misalignment of the anvils. The gap between the anvils is initially in the order of 100–150 μm and prevents the anvils of clashing together if the gasket fails during the experiment, thus reducing the risk of diamond damage.

The alignment procedure of the plate DAC is as follows. The height of both plates including diamonds is measured using callipers with a precision of ± 0.01 mm. After removing the lower seat, the plates are put together and the total height (bottom plate + top plate + gap) is adjusted with the plate alignment screws within -0.03 to $+0.1$ mm. The two opposing plates have to be parallel with a precision of ± 0.01–0.02 mm. After remounting the lower seat, the cell is closed and the diamonds brought close to touching using the gear tool. The gap can be monitored using a stereo microscope. The anvils can now be aligned horizontally using the diamond alignment screws. After bringing the diamonds into contact, the Newton interference fringes allow for marking the position where the anvils touch first. After opening the cell, the plate distance should be increased slightly at that position using on of the three plate alignment screws (1/10 of a turn is sufficient). This has to be repeated until the amount of fringes is preferably zero.

A.2 The ETH diamond anvil cell

The ETH DAC (Miletich et al., 2000) is a modification with reduced dimensions and weight of the original BGI DAC (Allan et al., 1996), allowing for better use with standard diffractometers. As can be seen in Fig. A.2 the ETH DAC follows the Merrill-Basset design (Merrill and Bassett, 1974) of two opposing steel plates. The top plate is guided onto the bottom plate by the guiding pins. Pressure is applied by four fine-thread pressure screws, the two pairs along the cell diagonal having opposite thread. Small adjustments to the screw pairs with Allan keys allow for controlled pressure change without misalignment of the diamond anvils.

The diamond anvils are mounted on flat backing plates hold in place by leaf springs and are made from X-ray transparent beryllium in order to simplify absorption corrections. However, in the case of synchrotron measurements, beryllium strongly increases the background, thus tungsten carbide backing plates are used alternatively. The bottom backing plate is mounted on an xy-stage, allowing for horizontal adjustment of the two diamond anvils, whereas the top backing plate is mounted on an hemispherical stage for vertical alignment. The metal gasket foil has a unique position ensured by the three asymmetrically placed positioning pins.

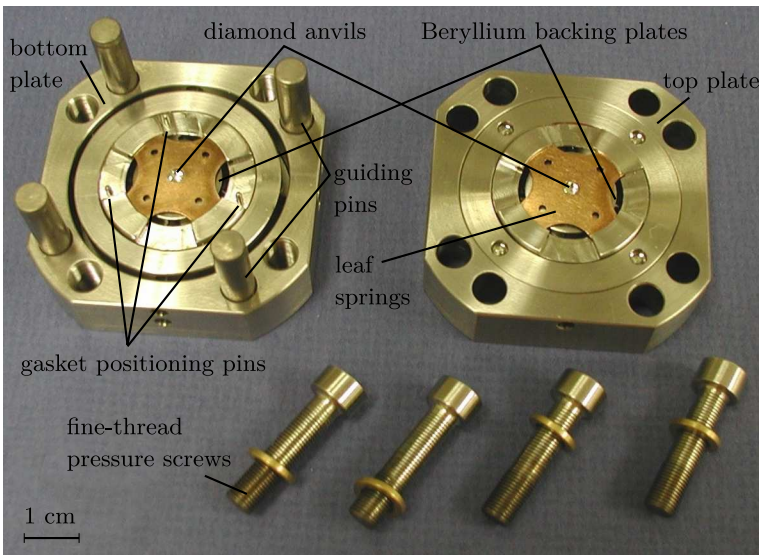

Figure A.2: The ETH DAC (Miletich et al., 2000).

A.3 The Ahsbahs diamond anvil cell

The Ahsbahs DAC (Ahsbahs, 2004) is an improvement of the "quadratic" DAC (Ahsbahs, 1995) which in turn was a modification of the original Merrill-Bassett-type DAC (Merrill and Bassett, 1974). The cell was specifically designed for the 0–10 GPa pressure range, as the limit of 10 GPa is given by liquid pressure transmitting media on the first place (Angel et al., 2007). In order to use the cell with modern area detectors, the beryllium backing plates, which give rise to a strong background, have been replaced by a special steel support schematically shown in Fig. A.3(a). The diamond anvil is pressed into its

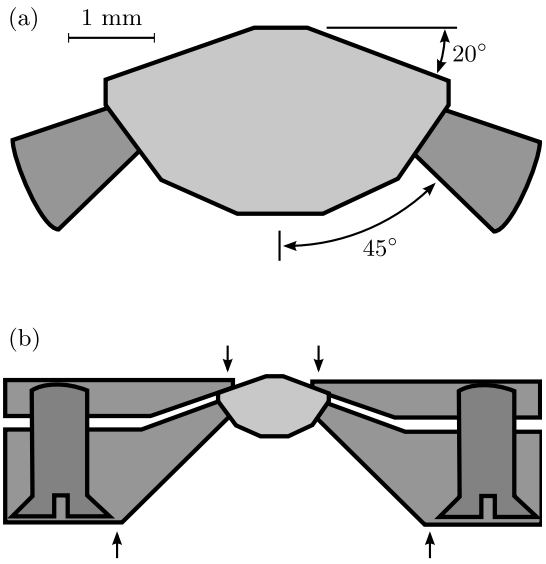

Figure A.3: Schematic view of the steel support holding the diamond anvil in a Ahsbahs-type DAC (Ahsbahs, 2004). The geometry of the diamond is shown in (a) and its mounting into the seat is shown in (b).

seat by a cover plate (Fig. A.3(b)). The setup allows for a wide opening angle of 90° and the almost spherical shape of the diamond eliminates the need of absorption corrections. However, the disadvantage is the flat angle of ∼20° between the culet and the tapering part of the diamond. Thus, the culets of the Ahsbahs DAC used in this work were abrased on the culet edge in order to produce an optimum angle of ∼40°. Nevertheless, thinner tungsten gaskets of approximately 100 μm thickness, preindented to ∼60 μm, are typically used for this cell. Although tungsten gaskets provide the advantage of high absorption of X-rays, thus reducing the background compared to steel gaskets, they behave unstable during pressure increase. Thus, 250 μm thick steel gaskets were used in this work, for which the extruded material was abrased during the indentation process in order to avoid too much pressure on the tapering part of the diamonds.

A.4 Loading the diamond anvil cell with a sample

The loading process consists of a few steps described in detail in the following sections.

A.4.1 Preparation of gaskets

As mentioned in 2.3.1, the gasket plays an important role during a high-pressure experiment conducted in a DAC. It is therefore vital to prepare a suitable gasket for a given experiment. For the diffraction experiments carried out in this work in a pressure range from 0–10 GPa, a stainless steel gasket is the best choice. The gaskets have an initial thickness of 250 μm. For the ETH and Ahsbahs cells, three holes have to be drilled for the guide pins used for a unique gasket position. For the Almax cells, the gasket is simply glued to the gasket holder with rapid glue.

After preindentation, a hole has to be drilled in the centre of the indented area. For this purpose the spark eroder shown in Fig. A.4 was used, capable of drilling holes of any diameter into any metal. The machine utilises an electric discharge in order to melt and evaporate the gasket material near an electrode, usually made of tungsten. The diameter of the hole is mainly influenced by the diameter of the electrode and the applied voltage between the gasket and the electrode. This process itself is complicated and is described by Lorenzana et al. (1994) for a similar device. In the following a practical guide to drill a hole with the spark eroder is given.

The gasket is mounted on the gasket holder which in turn is mounted on the xy-stage (Fig. A.4). The device has a microscope and a drilling mode. One can simply switch

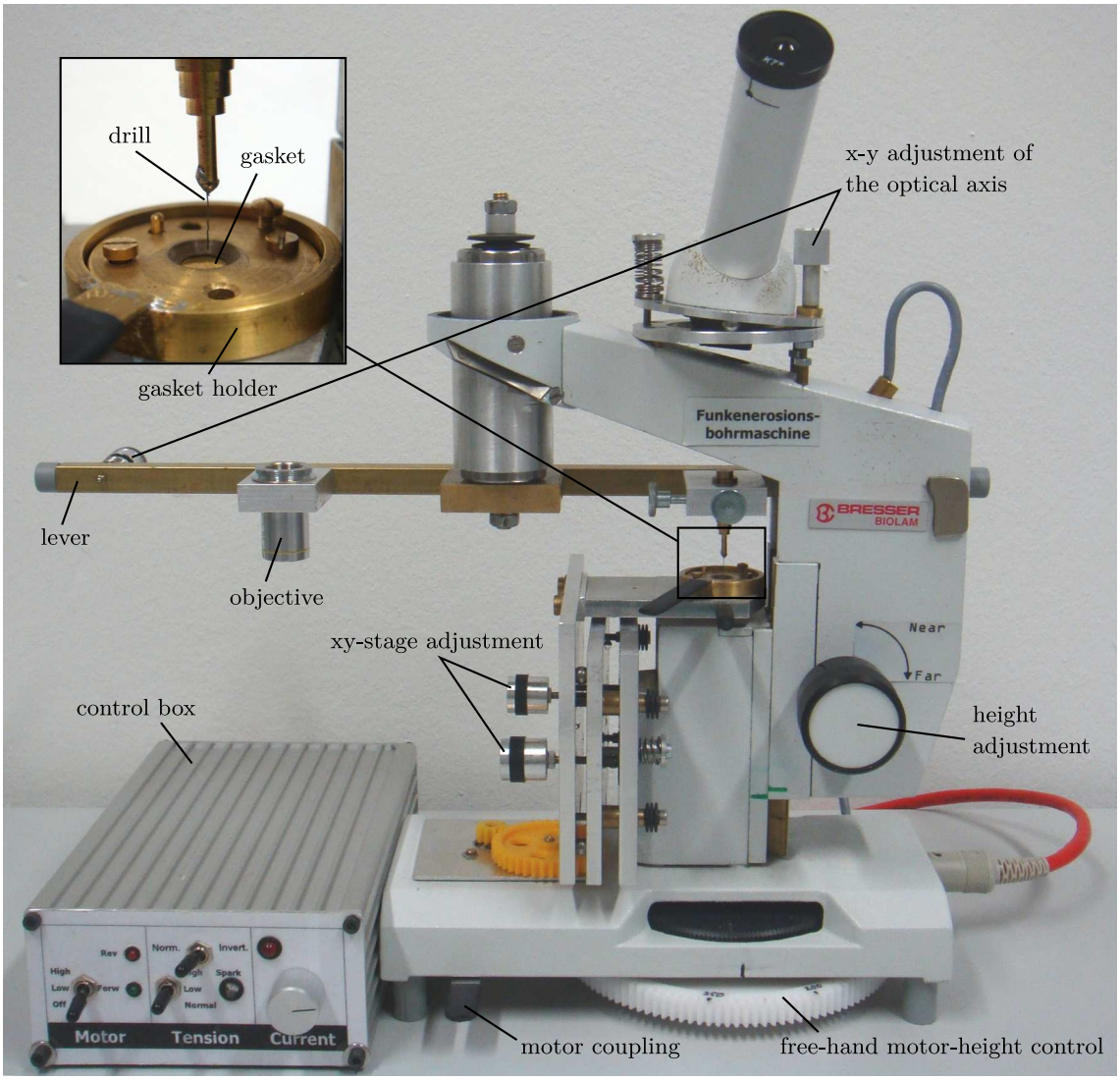

Figure A.4: The spark eroder used for drilling holes into gaskets. See text for a detailed description.

between the two regimes by turning the lever by 180°. Before drilling a hole into the indented area, the optical axis of the microscope has to be aligned with the axis of the electrode. For this purpose, the xy-stage is used in microscope mode to find an area far away from the anvil imprint, where a small hole with about 50 μm depth is drilled (see below for a description of the drilling). When switch back to the microscope mode, the centre of the cross-hair and thus the optical axis can be centred on the drilled hole by using the adjustment wheels marked Fig. A.4. Once the centring is done, the anvil imprint can be brought into the centre of the cross-hair by moving the gasket with the xy-stage. Now, the hole can be drilling by switching back to drilling mode and bringing the electrode close

to the gasket surface with the height adjustment wheel. The gasket has to be immersed in distilled water. A first spark will occur when the electrode is very close to the gasket surface. At this point, the motor can be switch on by using the control box which also allows for regulating the voltage and current. The hole is now drilled automatically. The driven distance of the xy-stage is given on the lower white gear, which can also be used as a free-hand fine height adjustment once the motor is decoupled with the motor coupling switch. Note that the machine will emit a beep in case the electrode in in contact with the gasket. This is automatically corrected during the drilling process. Once the hole is drilled, the gasket has to be thoroughly cleaned, removing all metal dust, especially from the inner rim of the hole.

A.4.2 Picking a suitable sample crystal

As mentioned in 2.3.1, the sample geometry is restricted by the experimental specification, i.e. the highest pressure to be achieved. Thus, the sample crystal has to be cut into proper dimensions from a 50–100 μm thick, polished plate. For this purpose a Olympus SZX16 zoom stereo-microscope with a maximum magnification of 230× was used. A small amount of petroleum jelly can be used to fix the sample on a glass plate. Once an optical homogeneous crystal is selected, it should be measured in air using a single-crystal diffractometer to check for its crystalline quality. This procedure is vital when measuring the sample at a synchrotron facility.

In addition to the sample crystal, a proper pressure marker has to be picked as well. In case of a diffraction standard crystal, the same routine as for the sample crystal is applied. A pressure calibrant based on the fluorescence method should be checked for optical signal and line shape.

A.4.3 Loading and closing the cell

Since the gasket hole should be drilled exactly in the centre of the indented area, the sample crystal and the pressure calibrant are placed in the culet centre. Usually, the sample is put on the diamond of the bottom plate. If the crystal orientation of the sample is known, it can be oriented according to the rotation axis of the cell. Once the sample is in place, the gasket is put on top of the bottom diamond. Note, that all the three DAC types used in this work ensure a unique gasket position, thus there is no risk of losing the sample. After the gasket is in place, a droplet of the pressure medium is put on the imprinted area of the gasket. As the pressure medium is usually a mixture of alcohols, the cell must be closed

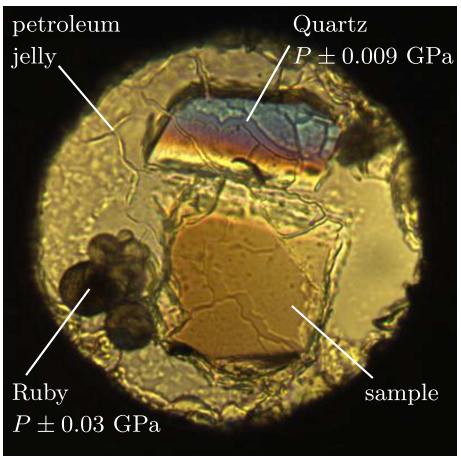

Figure A.5: Microscope image of a loaded DAC sample chamber (Angel, 2008). The sample is hold in place with petroleum jelly. In addition, there ruby and quartz placed next to the sample as pressure calibrants.

quickly and some initial pressure applied in order to prevent the pressure-transmitting medium from evaporating. Figure A.5 shows a microscopic image of the sample chamber of a loaded and closed DAC after (Angel, 2008).

B Group-theoretical analysis and peak assignment of Raman spectra

According to group theory, the Γ-point optical phonon modes of single-perovskite $Pm\bar{3}m$ cubic structure are $3F_{1u}$ (infrared active) + F_{2u} (inactive), none of them is Raman active. These phonon modes transform into $3A_1$ (Raman and infrared active) + A_2 (inactive) + $4E$ (Raman and infrared active) when the system undergoes a paraelectric-to-ferroelectric $Pm\bar{3}m$-to-$R3m$ phase transition. The Γ-point optical phonon modes of the double-perovskite $Fm\bar{3}m$ cubic structure are A_{1g} (Raman active) + E_g (Raman active) + $4F_{1u}$ (infrared active) + F_{1g} (inactive) + F_{2u} (inactive) + $2F_{2g}$ (Raman active). The A_{1g} and E_g modes give rise to two peaks in the Z(XX)$\overline{\text{Z}}$ polarised Raman spectrum, while the F_{2g} modes gives rise to two peaks in the Z(XY)$\overline{\text{Z}}$ polarised Raman spectrum. Under the paraelectric-to-ferroelectric phase transition, the cubic $Fm\bar{3}m$ modes transform into nine nondegenerate A modes and nine doubly degenerate E modes, which are all Raman active in the $R3$ structure. A more detailed site-symmetry analysis of phonon modes is given by Mihailova et al. (2002).

So far, the Raman peaks observed at $T > T_{\text{m}}$ have been controversially ascribed to different cubic modes (Siny et al., 2000; Jiang et al., 2001; Kreisel et al., 2002; Hehlen et al., 2007). However, it is a common opinion that the Raman spectra of Pb-based relaxors are best interpreted in terms of the double-perovskite prototype cubic structure, regardless of the degree of compositional B-site order determined by diffraction methods. The strong peak near 830 cm^{-1} originates from the A_{1g} mode related to the symmetrical stretching of BO_6 octahedra and the Raman scattering near 53 cm^{-1} results from the Pb-localised F_{2g} mode. The term *mode localisation* refers to the type of atoms which participate most to the corresponding phonon mode, i.e. the vibrational energy is localised in this type of atoms. For the F_{2g}, the amplitude of Pb atom displacements is considerable, while the vibration amplitude of the other types of atoms building the primitive unit cell (B-site cations and oxygen atoms) is negligible (Mihailova et al., 2002).

The origin of the Raman scattering near 240 cm^{-1} has been controversially related to cubic F_{2g}, F_{2u}, and F_{1u} modes. By considering the polarised Raman and synchrotron-based far-infrared ellipsometric spectra of stoichiometric as well as A- and B-site-doped PST and PSN single crystals, Mihailova et al. (2002, 2005, 2007b,c) were able to assign the observed Raman signals for these compounds to definite atomic vibrations. The strong B-cation mass dependence of the Raman peak position observed for PST and PSN single crystals (Mihailova et al., 2002) as well as for PST-PSN ceramics (Correa et al., 2007) clearly shows that the peak near 240 cm^{-1} arises from a B-cation localised mode. The site-symmetry group analysis predicts a B-localised F_{1u} mode, which is infrared active, and the corresponding infrared peaks were indeed recorded for PST and PSN (Mihailova et al., 2005). The occurrence of deviations of B-site cations from their positions in the ideal perovskite structure would lead to Raman activity related to the B-localised F_{1u} mode of the cubic phase. Therefore, the Raman scattering near 240 cm^{-1} observed for Pb-based perovskite-type relaxors is due to cation off-centre shifts in polar nanoregions. This assignment is in accordance with ab-initio calculations on $PbMg_{1/3}Nb_{2/3}O_3$, which reveal the existence of a polar mode near 255 cm^{-1} involving Nb vibrations (Choudhury et al., 2005).

The anomalous Raman scattering near 300-350 cm^{-1} is related to the silent F_{2u} mode and involves Pb-O bond stretching vibrations within the Pb-O sheets parallel to {111}. The intensity ratio

$$\rho = \frac{I(355)}{I(300)} \tag{B.1}$$

is indicative for the correlation length of coherent structural distortions in the Pb-O system (Mihailova et al., 2005). Besides, the intensity ratio ρ measured at temperatures higher than T_m correlates with the depolarisation of the Raman scattering observed at temperatures below T_m (Mihailova et al., 2007b,c).

The three-fold symmetrical axes of rhombohedral domains are oriented along the cubic body diagonals, which incline the cubic ⟨100⟩ crystallographic directions. Therefore, rhombohedral phonon modes contribute to both $Z(XX)\overline{Z}$ and $Z(XY)\overline{Z}$ Raman spectra and abundant establishment of ferroelectric order leads to almost the same spectral profiles measured in parallel and cross polarised scattering geometries, if the incident light polarisation is along the cubic edge. The depolarisation of the spectra due to the development of crystalline ferroelectric domains can be quantified via the intensity of the Raman band near between 750 and 950 cm^{-1} which arises from the cubic A_{1g} and E_g modes Mihailova et al. (2007c) contributing only to the $Z(XX)\overline{Z}$ spectrum. Hence, Raman

scattering between 750 and 950 cm^{-1} in the Z(XY)$\overline{Z}$ spectrum mirrors the existence of ferroelectric LRO domains below T_m and can be quantified via the intensity ratio

$$\eta = \frac{I_{cp}}{I_{pp} + I_{cp}} \tag{B.2}$$

where I_{cp} and I_{pp} denote the integrated intensity of the Raman-scattering band between 750 and 950 cm^{-1} measured in Z(XY)$\overline{Z}$ and Z(XX)$\overline{Z}$ geometries, respectively (Mihailova et al., 2007c). The depolarisation of the spectra η at 4 K versus the ratio ρ measured at 298 K for stoichiometric, Ba-, La-, Nb-, and Sn-doped PST as well as PST with enhanced and suppressed oxygen deficiency (Mihailova et al., 2007b,c, 2008b) shows that larger correlation between distorted Pb-O species leads to development of ferroelectric LRO and vice versa.

The anomalous Raman scattering near 135 cm^{-1} is related to the infrared-active translation mode F_{1u} which involves motions of BO_3 units against Pb atoms (Mihailova et al., 2002).

C Supplementary tables on the neutron powder diffraction data

Table C.1 gives the exposure time for each pressure point measured at a given press load in tonnes of the Paris-Edinburgh cell. As the intensity of the neutron beam varies with the synchrotron beam current, the exposure time is given as the integrated proton beam current delivered to the ISIS target.

Tab. C.2 and C.3 list the lattice parameters obtained from the Rietveld refinements at each pressure point for PST and PST-Ba, respectively. In the high-pressure phase, the unit-cell parameters are given in the hexagonal setting of space group $R\bar{3}c$. In addition, the pseudo-cubic lattice parameters are listed. Note that the cell doubling originates from the anti-phase octahedral tilting.

Table C.4 gives a list of the anisotropic ADP as well as the tilt parameters determined for PST and PST-Ba for the high-pressure phase refined in $R\bar{3}c$. Note that the results of

Table C.1: Load, pressure and integrated proton current (IPC) at the ISIS target for the neutron powder diffraction patterns obtained for PST and PST-Ba.

PST			PST-Ba		
Load (tns)	P (GPa)	IPC (μAh)	Load (tns)	P (GPa)	IPC (μAh)
0	0.00(0)	175	0	0.00(0)	95
6	0.13(3)	443	6	0.00(3)	170
9	0.40(4)	110	10	0.17(3)	112
13	1.09(2)	1046	14	0.59(4)	103
17	1.51(2)	1046	17.5	0.98(2)	904
20	1.84(3)	986	30	2.54(4)	170
25	2.63(3)	1046	35	3.52(3)	691
34	3.58(3)	1046	65	6.87(4)	871
54	5.10(4)	1155			
64	5.48(5)	345			
75	7.35(4)	2214			

Table C.2: Unit cell parameters of PST in hexagonal and pseudo-cubic settings obtained from refinements to neutron powder diffraction data. For all pressures a model with disordered B-site cation sites was refined. The doubling of the pseudo-cubic unit cell at pressures above 1.09 GPa results from the occurrence of anti-phase octahedral tilts.

P (GPa)	space group	a (Å)	c (Å)	a_{cub}	α_{cub} (°)	χ^2_w
0.00(0)	$Pm\bar{3}m$	–	–	4.0826(3)	90.00(0)	1.298
0.13(3)	$Pm\bar{3}m$	–	–	4.0811(2)	90.00(0)	1.597
0.40(4)	$Pm\bar{3}m$	–	–	4.0773(3)	90.00(0)	1.216
1.09(2)	$R\bar{3}c$	5.7541(8)	14.091(4)	8.1368(16)	90.01(2)	1.982
1.51(2)	$R\bar{3}c$	5.7444(9)	14.078(4)	8.1251(17)	89.98(2)	2.114
1.84(3)	$R\bar{3}c$	5.7373(9)	14.056(4)	8.1143(17)	89.99(2)	1.998
2.63(3)	$R\bar{3}c$	5.7264(8)	14.029(3)	8.0988(11)	90.00(2)	2.002
3.58(3)	$R\bar{3}c$	5.7147(5)	13.996(3)	8.0814(11)	90.01(2)	2.135
5.10(4)	$R\bar{3}c$	5.7002(5)	13.935(2)	8.0560(9)	90.08(2)	2.041
5.48(5)	$R\bar{3}c$	5.7001(6)	13.901(2)	8.0493(10)	90.17(2)	1.325
7.35(4)	$R\bar{3}c$	5.6828(4)	13.844(2)	8.0221(6)	90.21(2)	2.585

refinements in $R\bar{3}$ for each parameter are given in square brackets, confirming that both the results are the same within the errors.

Table C.3: Unit cell parameters of PST-Ba in hexagonal and pseudo-cubic settings obtained from refinements to neutron powder diffraction data. For all pressures a model with disordered B-site cation sites was refined. The doubling of the pseudo-cubic unit cell at pressures above 3.52 GPa results from the development of anti-phase octahedral tilts.

P (GPa)	space group	a (Å)	c (Å)	a_{cub}	α_{cub} (°)	χ^2_w
0.00(0)	$Pm\bar{3}m$	–	–	4.0837(1)	90.00(0)	1.352
0.17(3)	$Pm\bar{3}m$	–	–	4.0812(1)	90.00(0)	1.218
0.59(4)	$Pm\bar{3}m$	–	–	4.0762(1)	90.00(0)	1.189
0.98(2)	$Pm\bar{3}m$	–	–	4.0717(1)	90.00(0)	2.134
2.75(4)	$Pm\bar{3}m$	–	–	4.0529(1)	90.00(0)	1.281
3.52(3)	$R\bar{3}c$	5.7373(9)	14.056(4)	8.0922(11)	89.99(2)	1.910
6.87(4)	$R\bar{3}c$	5.6796(5)	13.919(3)	8.0356(12)	89.98(2)	1.821

Table C.4: Structural parameters for PST and PST-Ba obtained from refinements to neutron powder diffraction data in $R\bar{3}c$. Parameters in square brackets are for constrained $R\bar{3}$ refinements.

PST							
P (GPa)	U_{11} $(100 \cdot \text{Å}^2)$	U_{33} $(100 \cdot \text{Å}^2)$	U_{eq} $(100 \cdot \text{Å}^2)$	x	∠(B–O–B) (°)	$\omega(p)$ (°)	$\omega^2(p)$ (°)
1.09(2)	3.8(5) [4.0(10)]	4.8(12) [4.6(19)]	4.2(5) [4.2(9)]	0.5104(9) [0.5015(24)]	176.6(3) [179.5(0)]	1.7(2) [0.2(0)]	2.9(5) [0.1(0)]
1.51(2)	2.8(3) [2.6(3)]	6.0(6) [6.4(6)]	3.9(3) [3.9(3)]	0.5137(8) [0.5073(13)]	175.6(3) [177.6(4)]	2.2(2) [1.2(2)]	4.8(7) [1.4(5)]
1.84(3)	2.7(2) [2.4(2)]	5.4(6) [6.0(6)]	3.6(2) [3.6(2)]	0.5167(7) [0.5124(9)]	174.6(3) [176.0(3)]	2.7(2) [2.0(1)]	7.3(8) [4.0(6)]
2.63(3)	1.8(2) [1.8(2)]	6.1(5) [6.1(5)]	3.2(2) [3.2(2)]	0.5205(5) [0.5199(6)]	172.9(2) [172.9(2)]	3.5(1) [3.5(1)]	12.6(7) [12.6(7)]
3.58(3)	1.5(2) [1.5(2)]	5.3(5) [5.4(5)]	2.8(2) [2.8(2)]	0.5280(4) [0.5267(5)]	170.9(2) [171.4(2)]	4.5(1) [4.3(1)]	20.5(8) [18.5(9)]
5.10(4)	1.1(1) [1.0(1)]	5.1(4) [5.3(4)]	2.4(2) [2.4(2)]	0.5331(4) [0.5316(4)]	169.3(1) [169.8(2)]	5.3(1) [5.1(1)]	28.6(7) [26.0(10)]
5.48(5)	1.5(2) [1.4(2)]	4.2(5) [3.8(5)]	2.4(2) [2.2(2)]	0.5342(5) [0.5333(6)]	168.8(2) [169.2(2)]	5.5(1) [5.4(1)]	30.8(11) [29.2(11)]
7.35(4)	1.5(9) [1.5(9)]	3.3(3) [3.1(3)]	2.1(6) [2.1(6)]	0.5377(3) [0.5365(3)]	167.7(1) [168.1(1)]	6.1(1) [6.0(1)]	37.2(6) [35.4(6)]
PST-Ba							
3.52(3)	1.2(1) [1.2(1)]	8.0(4) [8.0(4)]	3.5(2) [2.2(2)]	0.5110(9) [0.5048(22)]	176.4(2) [178.4(3)]	1.8(2) [0.8(4)]	3.2(5) [0.6(5)]
6.87(4)	0.5(1) [0.4(1)]	7.1(4) [7.2(4)]	2.7(2) [2.7(1)]	0.5246(5) [0.5229(5)]	172.0(2) [172.6(2)]	4.0(1) [3.7(1)]	15.9(7) [12.7(6)]

References

Ahart, M., Cohen, R. E., Struzhkin, V., Gregoryanz, E., Rytz, D., Prosandeev, S. A., Mao, H.-K., and J.Hemley, R. (2005). High-pressure Raman scattering and x-ray diffraction of the relaxor ferroelectric $0.96Pb(Zn_{1/3}Nb_{2/3})O_{3-0.04}PbTiO_3$. *Phys. Rev. B*, 71:144102.

Ahsbahs, H. (1995). 20 Jahre Merrill-Bassett-Zelle. Einige Neuheiten. *Z. Kristallogr.*, Suppl.:42.

Ahsbahs, H. (2004). New pressure cell for single-crystal X-ray investigations on diffractometers with area detectors. *Z. Kristallogr.*, 219:305–308.

Allan, D. R., Miletich, R., and Angel, R. J. (1996). A diamond-anvil cell for single-crystal x-ray diffraction studies to pressures in excess of 10 GPa. *Rev. Sci. Instrum.*, 67:840–842.

Anderson, O. L. (1995). *Equations of state of solids for geophysics and ceramic science.* Oxford University Press.

Angel, R. J. (1993). The high-pressure, high-temperature equation of state of calcium fluoride, CaF_2. *J. Phys.: Condens. Matter*, pages L141–L144.

Angel, R. J. (2000). Equations of State. In Hazen, R. M. and Downs, R. T., editors, *High-pressure, high-temperature crystal chemistry*, volume 41 of *Reviews in Mineralogy and Geochemistry*, pages 35–69. Mineralogical Society of America.

Angel, R. J. (2008). School on *High pressure – high temperature mineral physics: implications for geosciences.* Handout Material.

Angel, R. J., Allan, D. R., Miletich, R., and Finger, L. W. (1997). The use of quartz as an internal pressure standard in high-pressure crystallography. *J. Appl. Crystallogr.*, 30:461–466.

Angel, R. J., Bismayer, U., and Marshall, W. G. (2004). Local and long-range order in ferroelastic lead phosphate at high pressure. *Acta Crystallogr.*, B60:1–9.

Angel, R. J., Bujak, M., Zhao, J., Gatta, G. D., and Jacobsen, S. D. (2007). Effective hydrostatic limits of pressure media for high-pressure crystallographic studies. *J. Appl. Crystallogr.*, 40:26–32.

Angel, R. J., Downs, R. T., and Finger, L. W. (2000). High-temperature, high-pressure diffractometry. In Hazen, R. M. and Downs, R. T., editors, *High-pressure, high-temperature crystal chemistry*, volume 41 of *Reviews in Mineralogy and Geochemistry*. Mineralogical Society of America.

Angel, R. J., Ross, N. L., Wood, I. G., and Woods, P. A. (1992). Single-crystal X-ray diffraction at high pressures with diamond-anvil cells. *Phase Trans.*, 39:13–32.

Angel, R. J., Zhao, J., and Ross, N. L. (2005). General rules for predicting phase transitions in perovskites due to octahedral tilting. *Phys. Rev. Lett.*, 95:025503.

Basset, W. A. (2009). Diamond anvil cell, 50th birthday. *High Pressure Res.*, 29:163–186.

Bérar, J.-F. and Baldinozzi, G. (1993). Modeling of line-shape asymmetry in powder diffraction. *J. Appl. Crystallogr.*, 26:128–129.

Besson, J. M., Nelmes, R. J., Hamel, G., Loveday, J. S., Weill, G., and Hull, S. (1992). Neutron powder diffraction above 10 GPa. *Physica B*, 180:907–910.

Bhalla, A. S., Guo, R., and Roy, R. (2000). The perovskite structure - a review of its role in ceramic science and technology. *Mater. Res. Innovations*, 4:3–29.

Birch, F. (1947). Finite elastic strain of cubic crystals. *Phys. Rev.*, 71:809–824.

Bismayer, U., Devarajant, V., and Groves, P. (1989). Hard-mode Raman spectroscopy and structural phase transition in the relaxorferroelectric lead scandium tantalate, $Pb(Sc_{0.5}Ta_{0.5})O_3$. *J. Phys.: Condens. Matter*, l:6977–6986.

Blinc, R., Gregorovič, A., Zalar, B., Pirc, R., Laguta, V. V., and Glinchuk, M. D. (2001). ^{207}Pb NMR study of the relaxor behavior in $PbMg_{1/3}Nb_{2/3}O_3$. *Phys. Rev. B*, 63:024104.

Blinc, R., Gregorovič, A., Zalar, B., Pirc, R., and Lushnikov, S. G. (2000). ^{45}Sc NMR study of the relaxor transition in a lead scandotantalate single crystal. *Phys. Rev. B*, 61(1):253–257.

Boehler, R. (2006). New diamond cell for single-crystal x-ray diffraction. *Rev. Sci. Instrum.*, 77:115103.

Bokov, A. A. (1997). Influence of disorder in crystal structure on ferroelectric phase transitions. *J. Exp. Theor. Phys.*, 84:994–1002.

Bokov, A. A. and Ye, Z.-G. (2006). Recent progress in relaxor ferroelectrics with perovskite structure. *J. Mater. Sci.*, 41:31–52.

Bonneau, P., Garnier, P., Calvarin, G., Husson, E., Gavarri, J. R., Hewat, A. W., and Morell, A. (1991). X-Ray and Neutron Diffraction Studies of the Diffuse Phase Transition in $PbMg_{1/3}Nb_{2/3}0_3$ Ceramics. *J. Solid State Chem.*, 91:350–361.

Burns, G. and Dacol, F. H. (1983). Crystalline ferroelectrics with glassy polarization behavior. *Phys. Rev. B*, 28(5):2527–.

Busing, W. R. and Levy, H. A. (1967). Angle calculations for 3- and 4- circle X-ray and neutron diffractometers. *Acta Crystallogr.*, 22:457–464.

Caglioti, G., Paoletti, A., and Ricci, F. (1958). Choice of Collimator for a Crystal Spectrometer for Neutron Diffraction. *Nucl. Instrum. Methods Phys. Res.*, 3:223–228.

CAMECA website (2009). Synopsis of the CAMECA SX100, `http://www.cameca.com/doc_en_pdf/SX100_synoptic_web.pdf`.

Carpenter, M. A. and Salje, E. K. H. (1998). Elastic anomalies in minerals due to structural phase transitions. *Eur. J. Mineral.*, 10:693–812.

Chaabane, B., Kreisel, J., Bouvier, P., Lucazeau, G., and Dkhil, B. (2004). Effect of high pressure on the $Pb(Mg_{1/3}Nb_{2/3})O_3$-$PbTiO_3$ solid solution:A Raman scattering investigation. *Phys. Rev. B*, 70:134114.

Chaabane, B., Kreisel, J., Dkhil, B., Bouvier, P., and Mezouar, M. (2003). Pressure-induced suppression of the diffuse scattering in the model relaxor ferroelectric PbMg1/3Nb2/3O3. *Phys. Rev. Lett.*, 90(25):257601.

Chen, I.-W., Li, P., and Wang, Y. (1996). Structural origin of relaxor perovskites. *J. Phys. Chem. Solids*, 57(10):1525 – 1536. Proceedings of the 3rd Williamsburg Workshop on Fundamental Experiments on Ferroelectrics.

Choudhury, N., Wu, Z., Walter, E. J., and Cohen, R. E. (2005). Ab initio linear response and frozen phonons for the relaxor $PbMg_{1/3}Nb_{2/3}O_3$. *Phys. Rev. B*, 71:125134.

Cohen, R. E. (1992). Origin of ferroelectricity in perovskite oxides. *Nature*, 358:136–138.

Correa, M., Choudhary, R. N. P., and Katiyar, R. S. (2007). Structural and dielectric properties of Ta-modified $Pb(Sc_{0.5}Nb_{0.5})O_3$ ceramics. *J. Appl. Phys.*, 101:054116.

Cross, L. E. (1987). Relaxor Ferroelectrics. *Ferroelectrics*, 76:241–267.

Cross, L. E. (1990). *Advanced Ceramics III*, chapter Ferroic Materials and Composites: Past, Present, and Future, pages 71–101. Elsevier Applied Science London and New York.

Davies, P. K., Wu, H., Borisevich, A. Y., Molodetsky, I. E., and Farber, L. (2008). Crystal Chemistry of Complex Perovskites: New Cation-Ordered Dielectric Oxides. *Annu. Rev. Mater. Res.*, 38:369–401.

Dkhil, B., Gemeiner, P., Al-Barakaty, A., Bellaiche, L., Dul'kin, E., Mojaev, E., and Roth, M. (2009). Intermediate temperature scale $T^\star$ in lead-based relaxor systems. *Phys. Rev. B*, 80:064103.

Dul'kin, E., Roth, M., Janolin, P.-E., and Dkhil, B. (2006). Acoustic emission study of phase transitions and polar nanoregions in relaxor-based systems: Application to the $PbZn_{1/3}Nb_{2/3}O_3$ family of single crystals. *Phys. Rev. B*, 73(1):012102.

Egami, T. (2002). Atomistic Mechanism of Relaxor Ferroelectricity. *Ferroelectrics*, 267:101–111.

Egami, T. (2007). Local Structure of Ferroelectric Materials. *Annu. Rev. Mater. Res.*, 37:297–315.

Eremets, M. (1996). *High Pressure Experimental Methods*. Oxford University Press.

Fan, H., Zhang, L., and Yao, X. (1998). Relaxation characteristics of strontium barium niobate ferroelectric ceramics. *J. Mater. Sci.*, 33:895–900.

Finger, L. W., Cox, D. E., and Jephcoat, A. P. (1994). A correction for powder diffraction peak asymmetry due to axial divergence. *J. Appl. Crystallogr.*, 27(6):892–900.

Forman, R. A., Piermarini, G. J., Barnett, J. D., and Block, S. (1972). Pressure Measurement Made by the Utilization of Ruby Sharp-Line Luminescence. *Science*, 176:284–285.

Giacovazzo, C., Monaco, H. L., Viterbo, D., Scordari, F., Gilli, G., Zanotti, G., and Catti, M. (1992). *Fundamentals of Crystallography*. Oxford University Press.

Glazer, A. M. (1972). The Classification of Tilted Octahedra in Perovskites. *Acta Crystallogr.*, B28:3384–3392.

Glinchuk, M. D. and Farhi, R. (1996). A random field theory based model for ferroelectric relaxors. *J. Phys.: Condens. Matter*, 8:6985–6996.

Goldschmidt, V. M. (1927). *Geochemische Verteilungsgesetze der Elemente*. Norske Videnskap, Oslo.

Goodwin, A. L., Redfern, S. A. T., Dove, M. T., Keen, D. A., and Tucker, M. G. (2007). Ferroelectric nanoscale domains and the 905 K phase transition in $SrSnO_3$: A neutron total-scattering study. *Phys. Rev. B*, 76:174114.

Gruverman, A. and Kholkin, A. (2006). Nanoscale ferroelectrics: processing, characterization and future trends. *Rep. Prog. Phys.*, 69(8):2443–2474.

Gvasaliya, S. N., Pomjakushin, V., Roessli, B., Strässle, T., S.Klotz, and Lushnikov, S. G. (2006). Anomalous pressure dependence of the atomic displacements in the relaxorferroelectric $PbMg_{1/3}Ta_{2/3}O_3$. *Phys. Rev. B*, 73:212102.

HASYLAB website (2009). Beamline F1, `http://hasylab.desy.de/facilities/doris_iii/beamlines/e6154/index_eng.html`.

Hazen, R. M. and Finger, L. W. (1981). Calcium fluoride as an internal pressure standard in high-pressure crystallography. *J. Appl. Crystallogr.*, 14(4):234–236.

Hehlen, B., Simon, G., and Hlinka, J. (2007). Polar modes in relaxor $PbMg_{1/3}Nb_{2/3}O_3$ by hyper-Raman scattering. *Phys. Rev. B*, 75:052104.

Hikichi, Y., Chen, Z., Newnham, R. E., and Cross, L. E. (1982). Preparation, thermal change and dielectric properties of cubic perovskites $A(B_{1/4}Nb_{3/4})O_3$ (A = Ba or Sr, B = Na or Li). *Mater. Res. Bull.*, 17:1371–1377.

Hirota, K., Wakimoto, S., and Cox, D. E. (2006). Neutron and X-ray Scattering Studies of Relaxors. *J. Phys. Soc. Jpn.*, 75:111006.

Hosono, Y. and Yamashita, Y. (2006). Piezoelectric ceramics and single crystals for ultrasonic medical transducers. *J. Electroceram.*, 17:577–583.

Howard, C. J., Kennedy, B. J., and Woodward, P. M. (2003). Ordered double perovskites – a group-theoretical analysis. *Acta Crystallogr.*, B59:463–471.

Howard, C. J. and Stokes, H. T. (2004). Octahedral tilting in cation-ordered perovskites - a group-theoretical analysis. *Acta Crystallogr.*, 60:674–684.

Howard, C. J. and Stokes, H. T. (2005). Structures and phase transitions in perovskites – a group-theoretical approach. *Acta Crystallogr.*, A61:93–111.

Ihringer, J. (1982). An automated low-temperature guinier X-ray diffractometer and camera. *J. Appl. Crystallogr.*, 15:1–4.

Imry, Y. and Ma, S.-K. (1975). Random-Field Instability of the Ordered State of Continuous Symmetry. *Phys. Rev. Lett.*, 35:1399–1401.

ISIS Annual Report (1996). Dedicated facility for high pressure diffraction. *Rutherford Appleton Laboratory Report*, RAL-TR-96-050:61–62.

ISIS Annual Report (1997). PEARL - Pressure and engineering research line. *Rutherford Appleton Laboratory Report*, RAL-TR-97-050:28–29.

ISIS/RAL website (2009). `http://www.isis.rl.ac.uk/`.

Isupov, V. A. (2003). Ferroelectric and Antiferroelectric Perovskites $PbB'_{0.5}B''_{0.5}O_3$. *Ferroelectrics*, 289(1):131–195.

Jacobson, A. J., Collins, B. M., and Fender, B. E. F. (1974). Powder Neutron-Diffraction Determination of Structure of $Ba_4Sb_3LiO_{12}$ - Preparation And Structure of Perovskite-Related Compounds $Ba_4M_3LiO_{12}$ (M=Sb,Bi) and $Ba_5M_3Li_2O_{15-X}$ (M=Te,U). *Acta Crystallogr.*, B30:1705–1711.

Jacobson, A. J., Collins, B. M., and Fender, B. E. F. (1976). Powder Neutron and X-Ray-Diffraction Determination of Structure of $Ba_3Ta_2ZnO_9$ - Investigation of Perovskite Phases in System Ba-Ta-Zn-O and Preparation Of $Ba_2TaCdO_{5.5}$ and $Ba_2CeInO_{5.5}$. *Acta Crystallogr.*, B32:1083–1087.

Janolin, P. E., Dkhil, B., Bouvier, P., Kreisel, J., and Thomas, P. A. (2006). Pressure instabilities up to 46 GPa in the relaxor ferroelectric $PbZn_{1/3}Nb_{2/3}O_3$. *Phys. Rev. B*, 73:094128.

Jeong, I. K., Darling, T. W., Lee, J. K., Proffen, T., Heffner, R. H., Park, J. S., Hong, K. S., Dmowski, W., and Egami, T. (2005). Direct observation of the formation of polar nanoregions in $Pb(Mg_{1/3}Nb_{2/3})O_3$ using neutron pair distribution function analysis. *Phys. Rev. Lett.*, 94(14):147602.

Jiang, F., Kojima, S., Zhao, C., and Feng, C. (2001). Chemical ordering in lanthanum-doped lead magnesium niobate relaxor ferroelectrics probed by A_{1g} Raman mode. *Appl. Phys. Lett.*, 79:3938–3940.

Kabsch, W. (1988). Evaluation of Single-Crystal X-ray Diffraction Data from a Position-Sensitive Detector. *J. Appl. Crystallogr.*, 21:916–924.

Kabsch, W. (1993). Automatic Processing of Rotation Diffraction Data from Crystals of Initially Unknown Symmetry and Cell Constants. *J. Appl. Crystallogr.*, 26:795–800.

Katrusiak, A. (2008). High-pressure crystallography. *Acta Crystallogr.*, A64:135–148.

Kerfah, A., Taïbi, K., Guehria-Laïdoudi, A., Simon, A., and Ravez, J. (2000). New oxyfluoride lead-free ferroelectric relaxors in the $BaTiO_3$–$BaZrO_3$–$BaLiF_3$ system. *Mat. Lett.*, 42:189–193.

King, H. and Finger, L. W. (1979). Diffracted beam crystal centering and its application to high-pressure crystallography. *J. Appl. Crystallogr.*, 12:374–378.

Kleemann, W. (1993). Random-Field Induced Antiferromagnetic, Ferroelectric And Structural Domain States. *Int. J. Mod. Phys. B*, 7:2469–2507.

Kreisel, J., Bouvier, P., Dkhil, B., Thomas, P. A., Glazer, A. M., Welberry, T. R., Chaabane, B., and Mezouar, M. (2003). High-pressure x-ray scattering of oxides with a nanoscale local structure: Application to Na1/2Bi1/2TiO3. *Phys. Rev. B*, 68(1):014113.

Kreisel, J., Dkhil, B., Bouvier, P., and Kiat, J. M. (2002). Effect of high pressure on relaxor ferroelectrics. *Phys. Rev. B*, 65:172101.

La-Orauttapong, D., Toulouse, J., Robertson, J. L., and Ye, Z. G. (2001). Diffuse neutron scattering study of a disordered complex perovskite Pb(Zn1/3Nb2/3)O-3 crystal. *Phys. Rev. B*, 6421(21):212101.

Laguta, V. V., Glinchuk, M. D., Bykov, I. P., Blinc, R., and Zalar, B. (2004). NMR study of ionic shifts and polar ordering in the relaxor ferroelectric $Pb(Sc_{1/2}Nb_{1/2})O_3$. *Phys. Rev. B*, 69:054103.

Langford, J. I. and Wilson, A. J. C. (1978). Scherrer after sixty years: A survey and some new results in the determination of crystallite size. *J. Appl. Crystallogr.*, 11:102–113.

Larson, A. C. and Von Dreele, R. B. (2004). General Structure Analysis System (GSAS). *Los Alamos National Laboratory Report*, LAUR:86–748.

Lente, M. H., Moreira, E. N., Garcia, D., Eiras, J. A., Neves, P. P., Doriguetto, A. C., Mastelaro, V. R., and Mascarenhas, Y. P. (2006). Induction of relaxor state in ordinary ferroelectrics by isovalent ion substitution: A pretransitional martensitic texture case. *Phys. Rev. B*, 73:054106.

Lines, M. E. and Glass, A. M. (1977). *Principles And Applications of Ferroelectrics and Related Materials*. Clarendon Press, Oxford.

Lorenzana, H. E., Bennahmias, M., Radousky, H., and Kruger, M. B. (1994). Producing diamond anvil cell gaskets for ultrahigh-pressure applications using an inexpensive electric discharge machine. *Rev. Sci. Instrum.*, 65:3540–3543.

Maichle, J., Ihringer, J., and Prandl, W. (1988). Simultaneous structure refinement of neutron, synchrotron and X-ray powder diffraction patterns. *J. Appl. Crystallogr.*, 21:22–27.

Maier, B. J. (2007). Analyse der thermischen Ausdehnung an organischen und anorganischen Materialien zur Bestimmung der Debye-Temperatur. Master's thesis, Universität Tübingen.

Maier, B. J., Mihailova, B., Paulmann, C., Ihringer, J., Gospodinov, M., Stosch, R., Güttler, B., and Bismayer, U. (2009). Effect of local elastic strain on the structure of Pb-based relaxors. A comparative study of pure, Ba- and Bi-doped $PbSc_{0.5}Nb_{0.5}O_3$. *Phys. Rev. B*, 79:224108.

Mao, H. K., Xu, J., and Bell, P. M. (1986). Calibration of the ruby pressure gauge to 800-kbar under quasi-hydrostatic conditions. *J. Geophys. Res.*, 91:4673–4676.

Marinova, V., Mihailova, B., Malcherek, T., Paulmann, C., Kovacs, K. L. L., Veleva, M., Gospodinov, M., Güttler, B., and Bismayer, R. S. U. (2006). Structural, optical and dielectric properties of relaxor-ferroelectric $Pb_{0.78}Ba_{0.22}Sc_{0.5}Ta_{0.5}O_3$. *J. Phys.: Condens. Matter*, 18:L385–L393.

Marshall, W. G. and Francis, D. J. (2002). Attainment of near-hydrostatic compression conditions using the Paris–Edinburgh cell. *J. Appl. Crystallogr.*, 35:122–125.

Megaw, H. D. and Darlington, C. N. W. (1975). Geometrical and Structural Relations in the Rhombohedral Perovskites. *Acta Crystallogr.*, A31:161–173.

Merkel, S. and Yagi, T. (2005). X-ray transparent gasket for diamond anvil cell high pressure experiments. *Rev. Sci. Instrum.*, 76.

Merrill, L. and Bassett, W. A. (1974). Miniature diamond anvil pressure cell for single crystal x-ray diffraction studies. *Rev. Sci. Instrum.*, 45:290–294.

Mihailova, B., Angel, R. J., Welsch, A.-M., Zhao, J., Engel, J., Paulmann, C., Gospodinov, M., Ahsbahs, H., Stosch, R., Güttler, B., and Bismayer, U. (2008a). Pressure-induced phase transition in $PbSc_{0.5}Ta_{0.5}O_3$ as a model Pb-based perovskite relaxor ferroelectric. *Phys. Rev. Lett.*, 101:017602.

Mihailova, B., Bastjan, M., Schulz, B., Rübhausen, M., Gospodinov, M., Stosch, R., Güttler, B., Malcherek, T., and Bismayer, U. (2007a). Resonance Raman scattering of relaxors $PbSc_{0.5}Ta_{0.5}O_3$ and $PbSc_{0.5}Nb_{0.5}O_3$. *Appl. Phys. Lett.*, 90:042907.

Mihailova, B., Bismayer, U., Güttler, B., Boris, M. G. A., Berndhard, C., and Aroyo, M. (2005). Nanoscale phase transformations in relaxor-ferroelectric lead scandium tantalate and lead scandium niobate. *Z. Kristallogr.*, 220:740–747.

Mihailova, B., Bismayer, U., Güttler, B., Gospodinov, M., and Konstantinov, L. (2002). Local structure and dynamics in relaxor-ferroelectric $PbSc_{1/2}Nb_{1/2}O_3$and $PbSc_{1/2}Ta_{1/2}O_3$ single crystals. *J. Phys.: Condens. Matter*, 14:1091–1105.

Mihailova, B., Gospodinov, M., Güttler, B., Petrova, D., Stosch, R., and Bismayer, U. (2007b). Ferroic nanoclusters in relaxors: the effect of oxygen vacancies. *J. Phys.: Condens. Matter*, 19(24):246220.

Mihailova, B., Gospodinov, M., Güttler, B., Stosch, R., and Bismayer, U. (2007c). Ferroic clustering and phonon anomalies in Pb-based perovksite-type relaxors. *J. Phys.: Condens. Matter*, 19:275205.

Mihailova, B., Maier, B., Paulmann, C., Malcherek, T., Ihringer, J., Gospodinov, M., Stosch, R., Güttler, B., and Bismayer, U. (2008b). High-temperature structural transformations in relaxor-ferroelectric $PbSc_{0.5}Ta_{0.5}O_3$ and $Pb_{0.78}Ba_{0.22}Sc_{0.5}Ta_{0.5}O_3$. *Physical Review B*, 77:174106.

Miletich, R., Reifler, H., and Kunz, M. (2000). *High-Pressure and High-Temperature Crystal Chemistry*, chapter High-pressure single-crystal techniques, pages 445–519. The Mineralogical Society of America.

Miyazawa, H., Ishii, F., Ishida, M., Natori, E., Shimoda, T., and Oguchi, T. (2003). Contribution of Pb to Ferroelectricity in Perovskite-type Oxides. *Mat. Res. Soc. Symp. Proc.*, 748:U3.2.1–U3.2.11.

Nelmes, R. J., Loveday, J. S., Wilson, R. M., Besson, J. M., Klotz, S., Hamel, G., and Hull, S. (1994). Structure Studies at High Pressure Using Neutron Powder Diffraction. In *Proceedings of the Symposium on Time-of-Flight Diffraction at Pulsed Neutron Sources*, volume 29, pages 19–27. American Crystallographic Association, Buffalo, New York.

Neurgaonkar, R. R., Hall, W. F., Oliver, J. R., Ho, W. W., and Cory, W. K. (1988). Tungsten bronze $Sr_{1-x}Ba_xNb_2O_6$: A case history of versatility. *Ferroelectrics*, 87:167–179.

Oxford Diffraction (2009). CrysAlisPro – RED, version 171.33.33d. *Oxford Diffraction Ltd, Abingdon, England.*

Pasciak, M., Wolcyrz, M., and Pietraszko, A. (2007). Interpretation of the diffuse scattering in Pb-based relaxor ferroelectrics in terms of three-dimensional nanodomains of the <110>-directed relative interdomain atomic shifts. *Phys. Rev. B*, 76(1):014117.

Paulmann, C. and Malcherek, T. (2006). Software development for studies of disorder-induced diffuse scattering using CCD-detectors. *Hasylab Annual Report*, Part I:1399–1400.

Peng, J. L. and Bursill, L. A. (1993). POLAR AND CHEMICAL DOMAIN STRUCTURES OF LEAD SCANDIUM TANTALATE (PST). *Mod. Phys. Lett B*, 7:609–621.

Perrin, C., Menguy, N., Suard, E., Mueller, C., Caranoni, C., and Stepanov, A. (2000). Neutron diffraction study of the relaxor ferroelectric phase transition in disordered $Pb(Sc_{1/2},Nb_{1/2})O_3$. *J. Phys.: Condens. Matter*, 12:7523–7539.

Piermarini, G. J., Block, S., Barnett, J. D., and Forman, R. A. (1975). Calibration of the pressure dependence of the R_1 ruby fluorescence line to 195 kbar. *J. Appl. Phys.*, 46:2774–2780.

Proffen, T. and Neder, R. B. (1997). DISCUS: a program for diffuse scattering and defect-structure simulation. *J. Appl. Crystallogr.*, 30:171–175.

Ralph, R. L. and Finger, L. W. (1982). A computer program for refinement of crystal orientation matrix and lattice constants from diffractometer data with lattice symmetry constraints. *J. Appl. Crystallogr.*, 15:537–539.

Raman, C. V. and Krishnan, K. S. (1928). A New Type of Secondary Radiation. *Nature*, 121(3048):501.

Rietveld, H. M. (1969). *J. Appl. Crystallogr.*, 2:65–71.

Ritter, H., Ihringer, J., Maichle, J., and Prandl, W. (2003). *SIMREF 2.7 manual*. Universität Tübingen.

Rotaru, G.-M., Gvasaliya, S. N., Pomjakushin, V., Roessli, B., Strässle, T., Lushnikov, S. G., Shaplygina, T., and Günter, P. (2008). Atomic displacements in $PbMg_{1/3}Nb_{2/3}O_3$ under high pressures. *J. Phys.: Condens. Matter*, 20:104235.

Samara, G. A. (2003). The relaxational properties of compositionally disordered ABO_3 perovskites. *J. Phys.: Condens. Matter*, 15(9):R367–R411.

Samara, G. A. and Venturini, E. L. (2006). Ferroelectric/relaxor crossover in compositionally disordered perovskites. *Phase Trans.*, 79:21–40.

Samara, G. A., Venturini, E. L., and Boatner, L. A. (2006). Dielectric properties and phase transitions of $Cd_2Nb_2O_7$: Effects of pressure and temperature. *J. Appl. Phys.*, 100:074112.

Scott, J. F. (2007). Applications of Modern Ferroelectrics. *Science*, 315:954–959.

Shannon, R. D. (1976). Revised effective ionic radii and systematic studies of interatomic distances in halides and chalcogenides. *Acta Cryst.*, A32:751–767.

Sheldrick, G. M. (2008). A short history of *SHELX*. *Acta Crystallogr.*, A64(1):112–122.

Siny, I. G., Katiyar, R. S., and Bhalla, A. S. (2000). *Ferroelectrics*, 2:51.

Stenger, C. G. F. and Burggraaf, A. J. (1980). Order-disorder reactions in the ferroelectric perovskites $Pb(Sc_{1/2}Nb_{1/2})O_3$ and $Pb(Sc_{1/2}Ta_{1/2})O_3$. II. Relation between ordering and properties. *Phys. Stat. Sol.*, 61(2):653–664.

Stokes, H. T., Kisi, E. H., Hatch, D. M., and Howard, C. J. (2002). Group-theoretical analysis of octahedral tilting in ferroelectric perovskites. *Acta Crystallogr.*, B58:934–938.

Svitelskiy, O., Toulouse, J., Yong, G., and Ye, Z. G. (2003). Polarized Raman study of the phonon dynamics in Pb(Mg1/3Nb2/3)O-3 crystal. *Phys. Rev. B*, 68(10):104107.

Toby, B. H. (2001). EXPGUI, a graphical user interface for GSAS. *J. Appl. Crystallogr.*, 34:210–213.

Tolédano, P. and Dmitriev, V. (1996). *Reconstructive Phase Transitions: In Crystals and Quasicrystals*. World Scientific.

Torres-Pardo, A., Jiménez, R., González-Calbet, J. M., and García-González, E. (2009). Induction of Relaxor Behavior in $Na_{1-x}Sr_{x/2}\square_{x/2}NbO_3$ through the Introduction of Cationic Vacancies. *Chem. Mater.*, 21:2193–2200.

Toulouse, J., Jiang, F., Svitelskiy, O., Chen, W., and Ye, Z. G. (2005). Temperature evolution of the relaxor dynamics in $Pb(Zn_{1/3}Nb_{2/3})O_3$: A critical Raman analysis. *Phys. Rev. B*, 72(18):184106.

Uchino, K. (2000). *Ferroelectric Devices*. New York: Decker.

Vijayakumar, M., Hoatson, G. L., and Vold, R. L. (2007). Identification of polar nanoclusters in $PbMg_{1/3}Nb_{2/3}O_3$ from NMR spectra. *Phys. Rev. B*, 75(10):104104.

Welberry, T. R. and Goossens, D. J. (2006). Chemical origin of nanoscale polar domains in $PbZn_{1/3}Nb_{2/3}O_3$. *Phys. Rev. B*, 74:224108.

Welberry, T. R. and Goossens, D. J. (2008). Different models for the polar nanodomain structure of PZN and other relaxor ferroelectrics. *J. Appl. Crystallogr.*, 41:606–614.

Welberry, T. R., Gutmann, M. J., Woo, H., Goossens, D. J., Xu, G., Stock, C., and Ye, Z.-G. (2005). Single-crystal neutron diffuse scattering and Monte Carlo study of the relaxor ferroelectric $PbZn_{1/3}Nb_{2/3}O_3$ (PZN). *J. Appl. Crystallogr.*, 38:639–647.

Welsch, A.-M., Maier, B. J., Engel, J., Mihailova, B., Angel, R. J., Paulmann, C., Gospodinov, M., Friedrich, A., Stosch, R., Güttler, B., and Bismayer, U. (2009a). Effect of Ba on pressure-induced structural changes in the relaxor ferroelectric $PbSc_{0.5}Ta_{0.5}O_3$. *Phys. Rev. B*, 80:104118.

Welsch, A.-M., Mihailova, B., Gospodinov, M., Stosch, R., Güttler, B., and Bismayer, U. (2009b). High pressure Raman spectroscopic study on the relaxor ferroelectric $PbSc_{0.5}Nb_{0.5}O_3$. *J. Phys.: Condens. Matter*, 21:235901.

Westphal, V., Kleemann, W., and Glinchuk, M. D. (1992). Diffuse phase transitions and random-field-induced domain states of the "relaxor" ferroelectric $PbMg_{1/3}Nb_{2/3}O_3$. *Phys. Rev. Lett.*, 68:847–850.

Woodward, P. M. (1997). Octahedral Tilting in Perovskites. I. Geometrical Considerations. *Acta Crystallogr.*, B53:32–43.

Woodward, P. M. and Baba-Kishi, K. Z. (2002). Crystal structures of the relaxor oxide $Pb_2(ScTa)O_6$ in the paraelectric and ferroelectric states. *J. Appl. Crystallogr.*, 35:233–242.

Xu, G., Gehring, P. M., and Shirane, G. (2006a). Coexistence and competition of local- and long-range polar orders in a ferroelectric relaxor. *Phys. Rev. B*, 74:104110.

Xu, G., Zhong, Z., Bing, Y., Ye, Z.-G., and Shirane, G. (2006b). Electric-field-induced redistribution of polar nano-regions in a relaxorferroelectric. *Nature*, 5:134–140.

Xu, G., Zhong, Z., Hiraka, H., and Shirane, G. (2004). Three-dimensional mapping of diffuse scattering in $Pb(Zn_{1/3}Nb_{2/3})O_3$–$xPbTiO_3$. *Phys. Rev. B*, 70:174109.

Zhang, L., Wang, X., Yang, W., Liu, H., and Yao, X. (2008). Structure and relaxor behavior of $BaTiO_3$–$CaTiO_3$–$SrTiO_3$ ternary system ceramics. *J. Appl. Phys.*, 104:014104.

Zhao, J., Ross, N. L., and Angel, R. J. (2004). Polyhedral control of the rhombohedral to cubic phase transition in $LaAlO_3$ perovskite. *J. Phys.: Condens. Matter*, 16:8763–8773.

Zhao, J., Ross, N. L., Angel, R. J., Carpenter, M. A., Howard, C. J., Pawlak, D. A., and Lukasiewicz, T. (2009). High-pressure crystallography of rhombohedral $PrAlO_3$ perovskite. *J. Phys.: Condens. Matter*, 21:235403.

Zhou, D. (2008). Piezoelectric Single Crystals of $Pb(Mg_{1/3}Nb_{2/3})O_3$-$PbTiO_3$ and their Applications in Medical Ultrasonic Transducers. In Chen, J. and Luo, H., editors, *International Conference on BioMedical Engineering and Informatics*, volume 2, pages 662–666.

Zhou, D. H., Hoatson, G. L., Vold, R. L., and Fayon, F. (2004). Local structure in perovskite relaxor ferroelectrics by ^{207}Pb NMR. *Phys. Rev. B*, 69:134104.

Curriculum vitae

Personal

Name	Bernd Jens Maier
Birth	27. November 1980, Böblingen, Germany
Office address	Universität Hamburg Mineralogisch-Petrographisches Institut Grindelallee 48 D-20146 Hamburg Fax: +49 (0)40 42838-2422 Phone: +49 (0)40 42838-2076 e-mail: bernd.maier@mineralogie.uni-hamburg.de

Education

10/2001–03/2007	Studies of Geosciences with focus crystallography at the University of Tübingen, Germany. Diploma thesis: *Analyse der thermischen Ausdehnung an organischen und anorganischen Materialien zur Bestimmung der Debye Temperatur.*
2002–2006	Student assistant for various tasks, e.g. the setup of a X-ray diffractometer.
08–09/2005	Traineeship at HMI Berlin, SFB 2, Abt. Magnetismus with focus on neutron diffraction.
03/2006	Laboratory course on neutron scattering, research centre Jülich, Germany.

04/2007–03/2010 Doctorate studies at the University of Hamburg, Germany. Research on relaxor ferroelectrics using temperature and pressure dependent synchrotron and neutron diffraction.

02/2008 Participance at the school *High pressure – high temperature mineral physics: implications for geosciences*, Italy.

04–06/2008 Ph.D. internship for Prof. Ross Angel, crystallography laboratory, Virginia Tech, USA. Studies on relaxor ferroelectrics using high-pressure single-crystal X-ray diffraction.

09/2008 Participance at the course *Diffuse Scattering and Structure Simulation*, University of Erlangen, Germany.

Teaching activities

2002–2006 Tutor for undergraduates in the subject *Mineralogy*, University of Tübingen.

2008–2010 Assistance to Prof. Mihaylova for the MSc course *Materials Research Methods*, University of Hamburg.

2008–2009 Assistance to Prof. Bismayer for the BSc course *Crystallography*, University of Hamburg.

Service to the Scientific Community

2008 Referee for the Journal of Electroceramics.

List of publications

B. J. Maier, A.-M. Welsch, R. J. Angel, B. Mihailova, J. Zhao, J. M. Engel, L. A. Schmitt, C. Paulmann, M. Gospodinov, A. Friedrich, and U. Bismayer. A-site Doping Induced Renormalization of Structural Transformations in $PbSc_{0.5}Nb_{0.5}O_3$ Relaxor Ferroelectric under High Pressure. *Phys. Rev. B*, 81:174116, 2010.

B. J. Maier, R. J. Angel, W. G. Marshall, B. Mihailova, C. Paulmann, J. M. Engel, M. Gospodinov, A.-M. Welsch, D. Petrova, and U. Bismayer. Octahedral tilting in Pb-based relaxor ferroelectrics at high pressure. *Acta Crystallogr. B*, 66:280–291, 2010.

A.-M. Welsch, **B. J. Maier**, J. Engel, B. Mihailova, R. J. Angel, C. Paulmann, M. Gospodinov, A. Friedrich, R. Stosch, B. Güttler, and U. Bismayer. Effect of Ba on pressure-induced structural changes in the relaxor ferroelectric $PbSc_{0.5}Ta_{0.5}O_3$. *Phys. Rev. B*, 80:104118, 2009.

B. Maier, B. Mihailova, C. Paulmann, J. Ihringer, M. Gospodinov, R. Stosch, B. Güttler, and U. Bismayer. Effect of local elastic strain on the structure of Pb-based relaxors. A comparative study of pure, Ba- and Bi-doped $PbSc_{0.5}Nb_{0.5}O_3$. *Phys. Rev. B*, 79:224108, 2009.

B. Mihailova, **B. Maier**, C. Paulmann, T. Malcherek, J. Ihringer, M. Gospodinov, R. Stosch, B. Güttler, and U. Bismayer. High-temperature structural transformations in relaxor-ferroelectric $PbSc_{0.5}Ta_{0.5}O_3$ and $Pb_{0.78}Ba_{0.22}Sc_{0.5}Ta_{0.5}O_3$. *Phys. Rev. B*, 77: 174106, 2008.

Contribution to conferences:

B. J. Maier, R. J. Angel, W. G. Marshall, B. Mihailova, C. Paulmann, J. M. Engel, M. Gospodinov, A.-M. Welsch, D. Petrova, and U. Bismayer. The high-pressure structure of Pb-based relaxor ferroelectrics. In *Frühjahrstagung der Sektion Kondensierte Materie (SKM) der Deutschen Physikalischen Gesellschaft (DPG)*, Regensburg, Germany, March 2010. Oral presentation.

N. Waeselmann, B. Mihailova, **B. Maier**, M. Gospodinov, and U. Bismayer. The local structure of 0.9PZN-0.1PT at high temperature and pressure. In *Frühjahrstagung der Sektion Kondensierte Materie (SKM) der Deutschen Physikalischen Gesellschaft (DPG)*, Regensburg, Germany, March 2010. Poster presentation.

B. Mihailova, **B. J. Maier**, R. J. Angel, A.-M. Welsch, and U. Bismayer. Structure refinement of the high-pressure phase of Pb-based relaxor ferroelectrics. In *3rd Berichtskolloquium of SPP 1236*, Overursel, Germany, March 2010. Oral presentation.

N. Waeselmann, **B. Maier**, B. Mihailova, M. Gospodinov, and U. Bismayer. In situ high pressure and high temperature Raman spectroscopy of $PZn_{1/3}Nb_{2/3}O_3$-$PTiO_3$ near the morphotropic phase boundary. In *3rd Berichtskolloquium of SPP 1236*, Oberursel, Germany, March 2010. Poster presentation.

N. Waeselmann, B. Mihailova, A.-M. Welsch, **B. J. Maier**, and U. Bismayer. Pb-based relaxor ferroelectrics under high pressure and temperature. In *437. Wilhelm und Else Heraeus Seminar*, Bad Honnef, Germany, December 2009. Poster and short oral presentation.

B. Mihailova, **B. Maier**, A.-M. Welsch, R. J. Angel, M. Gospodinov, and U. Bismayer. Temperature/pressure-driven transformation processes in pure, Ba- and Bi-doped $PbSc_{0.5}Nb_{0.5}O_3$. In *Joint Meeting of 12th International Meeting on Ferroelectricity and 18th IEEE Symposium on Applications of Ferroelectrics (IMF–ISAF)*, Xi'an, China, August 2009. Oral presentation.

A.-M. Welsch, B. Mihailova, **B. Maier**, J. Engel, C. Paulmann, R. J. Angel, J. Zhao, M. Gospodinov, R. Stosch, B. Güttler, and U. Bismayer. Effect of Ba on pressure-induced changes in the relaxor ferroelectric $PbSc_{0.5}Ta_{0.5}O_3$. In *1st Workshop for the Extreme Conditions Beamline at PETRA III*, Hamburg, Germany, May 2009. Poster presentation.

B. Maier, C. Paulmann, R. J. Angel, J. Engel, M. Gospodinov, B. Mihailova, and U. Bismayer. Single-Crystal X-ray Diffraction Study on Lead Scandium Niobate (PSN) and A-site Doped PSN at High Pressures. In *Frühjahrstagung der Sektion Kondensierte Materie (SKM) der Deutschen Physikalischen Gesellschaft (DPG)*, Dresden, Germany, March 2009. Oral presentation.

B. Maier, C. Paulmann, T. Malcherek, J. Ihringer, M. Gospodinov, R. J. Angel, B. Mihailova, and U. Bismayer. Temperature- and Pressure-dependent X-ray Diffraction

on A-site Doped Lead Scandium Niobate. In *86. Jahrestagung der Deutschen Mineralogischen Gesellschaft (DMG)*, Berlin, Germany, September 2008. Oral presentation.

B. Mihailova, R. J. Angel, **B. Maier**, A.-M. Welsch, C. Paulmann, T. Malcherek, M. Gospodinov, B. Güttler, and U. Bismayer. Temperature- and pressure-induced structural changes in the perovskite-type relaxor ferroelectric $PbSc_{0.5}Ta_{0.5}O_3$. In *86. Jahrestagung der Deutschen Mineralogischen Gesellschaft (DMG)*, Berlin, Germany, September 2008. Oral presentation.

B. Mihailova, **B. Maier**, C. Paulmann, T. Malcherek, M. Gospodinov, B. Güttler, and U. Bismayer. High-temperature structural transformations in Pb-based perovskite-type relaxor ferroelectrics. In *22nd General Conference of the Condensed Matter Division (CMD 22) of the European Physical Society (EPS)*, Rome, Italy, August 2008. Oral presentation.

B. Mihailova, **B. Maier**, C. Paulmann, T. Malcherek, J. Ihringer, M. Gospodinov, R. Stosch, B. Güttler, , and U. Bismayer. Temperature Induced Phase Transformations in Relaxor Ferroelectrics Lead Scandium Tantalate and Ba-doped Lead Scandium Tantalate. In *Annual Meeting of the American Crystallographic Association (ACA)*, Knoxville, USA, May 2008. Poster presentation.

B. Mihailova, **B. Maier**, C. Paulmann, T. Malcherek, J. Ihringer, M. Gospodinov, R. Stosch, B. Güttler, and U. Bismayer. Temperaturabängige Phasenübergänge in den Relaxor-Ferroelektrika $PbSc_{0.5}Ta_{0.5}O_3$ und $Pb_{0.78}Ba_{0.22}Sc_{0.5}Ta_{0.5}O_3$. In *16. Jahrestagung der Deutschen Gesellschaft für Kristallographie (DGK)*, Erlangen, Germany, March 2008. Oral presentation.

B. Mihailova, **B. Maier**, C. Paulmann, T. Malcherek, J. Ihringer, M. Gospodinov, R. Stosch, B. Güttler, and U. Bismayer. Temperature-driven structural transformations in relaxor-ferroelectric $PbSc_{0.5}Ta_{0.5}O_3$ and $Pb_{0.78}Ba_{0.22}Sc_{0.5}Ta_{0.5}O_3$. In *72. Jahrestagung der Deutschen Physikalischen Gesellschaft (DPG)*, Berlin, Germany, February 2008. Oral presentation.

B. Maier, B. Mihailova, and U. Bismayer. Crystal Structure Of The Relaxor Ferroelectric Lead Scandium Tantalate Oxide (PST). In *11^{th} European Meeting on Ferroelectricity*, Bled, Slovenia, September 2007. Poster presentation.

B. Maier, B. Mihailova, J. Ihringer, and U. Bismayer. Structure Refinement Of The Relaxor Ferroelectric $PbSc_{0.5}Ta_{0.5}O_3$ (PST). In *Smart Materials and Structures, 2nd International Workshop*, Kiel, Germany, August 2007. Oral presentation.

B. Maier, J. Ihringer, B. Mihailova, and U. Bismayer. Structure of the relaxor ferroelectric $PbSc_{0.5}Ta_{0.5}O_3$ from 300 K to 20 K. In *71. Jahrestagung der Deutschen Physikalischen Gesellschaft (DPG)*, Regensburg, Germany, March 2007. Oral presentation.

B. Maier, J. Ihringer, and F. Schreiber. Structure and unusual thermal behaviour of a prototype organic semiconductor (Diindenoperylene). In *71. Jahrestagung der Deutschen Physikalischen Gesellschaft (DPG)*, Regensburg, Germany, March 2007. Poster presentation.

Annual reports of synchrotron and neutron facilities:

B. J. Maier, R. J. Angel, B. Mihailova, J. M. Engel, A.-M. Welsch, C. Paulmann, M. Gospodinov, and U. Bismayer. High-pressure structural state of La-doped $PbSc_{0.5}Ta_{0.5}O_3$ and $PbSc_{0.5}Nb_{0.5}O_3$ relaxor ferroelectrics. In *Hasylab Annual Reports*, 2009.

B. J. Maier, R. J. Angel, B. Mihailova, J. M. Engel, A.-M. Welsch, C. Paulmann, M. Gospodinov, and U. Bismayer. Pressure-induced X-ray diffraction peaks and diffuse scattering in Pb-based perovskite-type relaxors. In *Hasylab Annual Reports*, 2009.

B. J. Maier, R. J. Angel, B. Mihailova, and W. G. Marshall. Pressure-induced phase transition in $PbSc_{0.5}Ta_{0.5}O_3$ as a model Pb-based perovskite-type relaxor ferroelectric. In *ISIS Experimental Report*, 2009.

B. J. Maier, R. J. Angel, J. Engel, C. Paulmann, B. Mihailova, M. Gospodinov, A. Friedrich, and U. Bismayer. Effect of Ba on the high-pressure structural state of $PbSc_{0.5}Ta_{0.5}O_3$ relaxor ferroelectric. In *Hasylab Annual Reports*, 2008.

B. J. Maier, C. Paulmann, B. Mihailova, M. Gospodinov, and U. Bismayer. Low-temperature state of La-doped $PbSc_{0.5}Ta_{0.5}O_3$ and $PbSc_{0.5}Nb_{0.5}O_3$ relaxor ferroelectrics. In *Hasylab Annual Reports*, 2008.

B. J. Maier, C. Paulmann, B. Mihailova, M. Gospodinov, and U. Bismayer. Renormalization phenomena in Ba and Bi doped $PbSc_{0.5}Nb_{0.5}O_3$ relaxor ferroelectrics. In *Hasylab Annual Reports*, 2008.

R. J. Angel, J. Engel, C. Paulmann, **B. Maier**, H. Ahsbahs, B. Mihailova, M. Gospodinov, and U. Bismayer. Structural transformations in relaxor-ferroelectric $PbSc_{0.5}Ta_{0.5}O_3$ under pressure. In *Hasylab Annual Reports*, 2007.

Acknowledgements

First of all I would like to thank Prof. Ulrich Bismayer and Prof. Boriana Mihailova for supervising and guiding me through the three years of my Ph.D. thesis, during which I could learn a great deal about the work's subject, experimental techniques, and scientific publishing.

This work was achieved with the help of many people who deserve my gratitude. These are in detail Dr. Carsten Paulmann and Dr. Thomas Malcherek for technical assistance and fruitful discussions on single-crystal X-ray diffraction experiments, Peter Stutz for preparing sample cuts, Dipl.-Min. Stefanie Heidrich for measuring the chemical sample composition with the electron microprobe, and Joachim Ludwig for measuring the in-house powder X-ray diffraction patterns. Thanks also to the workshop staff, especially to Ralph Görbing, for the realization of technical parts for experiments, to Prof. Marin Gospodinov for growing and supplying the sample crystals, and to Dr. Alexandra Friedrich helping me with the preparation of diamond anvil cells at the Goethe-Universität Frankfurt. Special thanks to my room-sharing fellow Dr. Anna-Maria Welsch for many fruitful discussions, working on common problems, and a great time in the office.

Special thanks also to Prof. Ross Angel for teaching me high-pressure crystallography in detail during and after my three-month stay in his Crystallography Laboratory at the Virginia Tech University in Blacksburg, USA. He also provided a great deal of assistance during the synchrotron and neutron experiments and helped with the data reduction and analysis. Thanks also to Dr. Jens Engel who introduced me to the technical handling of diamond anvil cells with great patience and provided his time during the synchrotron measurements.

My thanks also to Prof. Jörg Ihringer for enabling me to low-temperature powder data at the Institut für Angewandte Physik, Universität Tübingen and for sharing his crystallographic knowledge for my particular field of study.

Thanks also to the people who had to suffer the proof-reading of this work. I am certain that there is no typing error left.

Most important, however, is the personal support I received from my beloved partner Anne who had to suffer times in which I was quite occupied with this work. She was backing me all the time and gave me reassurance when I needed them most. She also gifted me with the birth of our wonderful son Felix for whose smile I am grateful every day. Thank you!

Last but not least, I like to thank also my parents for personal support and enabling this work in the first place by financial support during my education.

This work was financially supported by the Deutsche Forschungsgemeinschaft via the Interdisciplinary Graduate School 611 *Design and Characterisation of Functional Materials*, which is gratefully acknowledged by the author.